N64-30604

CONTINUOUS MICROWAVE MAGNETIC ACCELERATOR

by

David B. Miller

prepared for

NATIONAL AERONAUTICS AND SPACE ADMINISTRATION

CONTRACT NO. NAS 3-3567

OTS PRICE

XEROX $

MICROFILM $

SPACE SCIENCES LABORATORY

GENERAL ELECTRIC

MISSILE AND SPACE DIVISION

Requests for copies of this report should be referred to

National Aeronautics and Space Administration
Office of Scientific and Technical Information
Attention: AFSS-A
Washington, D.C. 20546

SUMMARY REPORT

CONTINUOUS MICROWAVE MAGNETIC ACCELERATOR

By

David B. Miller

Prepared for

NATIONAL AERONAUTICS AND SPACE ADMINISTRATION

8 August 1963 to 7 August 1964

CONTRACT NAS 3-3567

GENERAL ELECTRIC COMPANY
Space Sciences Laboratory
Missile and Space Division
P. O. Box 8555, Philadelphia 1, Pa.

ABSTRACT

30604

During this one year program, a cyclotron-resonance accelerator (8.35 gc) was tested up to 4150 watts, and was shown under proper conditions to convert over 50% of the incident r-f power into directed motion of the accelerated exhaust stream. Continuous operating times at these several kilowatt power levels were typically one to four minutes.

Total and sampling collectors were used to measure power and ion flux density within the accelerated plasma stream. Calorimetry in the thrustor walls, shielded antenna probes, bare-electrode probes, and a microwave reflectometer yielded addition thrustor characteristics.

Author

Table of Contents

List of Figures

List of Tables

I. INTRODUCTION AND SUMMARY

The magnetic-resonance, or cyclotron-resonance (Cyclops) plasma accelerator is a continuous-wave (c-w), electrodeless system which employs electron cyclotron resonance coupling of power from a microwave electromagnetic field to the plasma electrons. The power is subsequently transferred from the transverse cyclotron motions of the electrons to longitudinal ion motion (thereby generating the $\dot{m}$ v required for thrust) by a magnetic-field gradient/charge-separation-electric-field process.

The magnetic-resonance accelerator is being evaluated under NASA sponsorship as a possible space propulsion engine. Since there are numerous other electric thrustor concepts also being investigated for this same purpose, it is proper to consider what advantages this particular system has which make its study worth continuing. Three basic features can be listed:

A. ELECTRODELESS

Power is coupled to the plasma through an induced electric field. This avoids the erosion problem resulting when large amounts of power must be transferred to a plasma through electrodes.

B. RESONANCE

Because of the resonance coupling of power from the r-f field to the plasma, essentially all of the r-f source power can be transferred by this device into the plasma. This is in contrast to other inductive (electrodeless) accelerators, which typically exhibit very poor coupling between the circuit and the plasma.

C. CONTINUOUS-WAVE

The magnetic-resonance accelerator does not depend on self-fields and therefore does not require the high peak powers of the pulsed accelerators. Thus, problems of high instantaneous voltage and current are avoided.

This report covers the work which has been carried out during the third year of effort on the cyclotron-resonance accelerator. In order to summarize the progress which has been made during this third year, it will be in order first to indicate briefly where the project stood at the beginning of this third year.

At the beginning of this effort, simultaneous experimental and theoretical studies were initiated. The theoretical work resulted primarily in an understanding of the important r-f/plasma coupling processes. The need for a properly-oriented, circularly-polarized wave was recognized, the influence of Doppler broadening on the coupling process was revealed, and the advantage of a broad r-f/plasma boundary, enhanced by high velocity gas injection and by a gradient in the magnetic field, was hypothesized.

After some initial pulsed studies, the experimental effort eventually led to a successful medium power (320 watt), S-band (2450 mc), c-w experiment. While this experiment successfully accelerated plasmas under steady-state, c-w conditions, it also pointed out some problem areas. Foremost of these was the problem of designing a dielectric wall which would allow the r-f power to pass into the plasma but would also sustain the severe plasma

heating. An additional problem was the apparently poor mass utilization of this S-band accelerator.

The desirability of going to higher power and higher frequency was recognized at an early stage in this effort, and as a result, another major achievement of the first two years was to get into operation an X-band (8350 mc) experiment capable of power levels of several kilowatts.

Thus, at the beginning of this third year, some theoretical understanding of the accelerator was in hand, experience had been gained with a c-w accelerator, and apparatus was ready to go on to higher-power, higher-frequency experiments.

The important accomplishment of this third year has been to operate a c-w, X-band, cyclotron-resonance plasma accelerator at high power (up to 4150 watts) and high power efficiency*(up to .53) under steady-state conditions (up to 4 minutes 28 seconds continuous operation). These experiments have also demonstrated that the coupling of power from the r-f wave into the plasma can be very efficient, that is, greater than 95%. These favorable accomplishments were the result of significant improvements in accelerator design. During the course of these studies, improved diagnostics techniques were also developed.

With regard to accelerator design, a basic accelerator (the "longitudinal-interaction" device) was designed at the beginning of the year, but two major changes in this basic design were required to attain the final results. First, the window through which the r-f enters the plasma was changed. In addition,

----

*-Defined as: plasma stream power/ incident r-f power.

after probing the r-f propagation into the plasma and the heat loss from the plasma, it was determined that a much shorter accelerator should yield much higher efficiencies. Accordingly, a short model was built and this verified the hypothesis by operating at better than 50% power conversion efficiency.

As pointed out in the previous paragraph, diagnostics within the accelerator itself led to an improved accelerator design. Additional improvements in diagnostics included a steady-state calorimeter and a sampling probe array. This latter instrument has shown that, while the accelerated plasma stream has a complex cross-sectional profile, it is more confined than would result if ions followed magnetic field lines.

An alternate basic design (the "transverse-interaction" accelerator) was tested, with the indication being that it was not a very efficient system. It had unique features, however, that might make it worthy of further study at a later time.

Because of the attractive operating characteristics achieved during this year, it is felt that development of a cyclotron-resonance thrustor should continue. The following goals, with possible means of attaining them, should be considered.

    1. Better determination of thrustor performance by improvement in diagnostic techniques: A thrust stand should be used with the calorimeter to measure total efficiency. Plasma potential and particle probes should be improved to give independent measurements of

velocity and mass efficiencies.

2. Improvement in engine efficiencies: The effects of variations in gas injection, magnetic field shape, gas species and accelerator geometry should be studied.

3. Increase in operating time: Improved efficiency will automatically lead to less engine heating and therefore less likelihood of failure during long-duration tests. In addition, further improvement in window design and accelerator cooling should be made.

With regard to eventual applications, several other, longer-range goals should be kept in mind. Conversion from coils to permanent magnets should be made as soon as a final accelerator design and field shape have been made. Easily storable propellants (e.g., cesium) should be tried. The development of high-efficiency r-f sources should be encouraged. Finally, missions on which the cyclotron-resonance thrustor can be employed should be identified.

2. EXPERIMENTAL PROGRAM
LONGITUDINAL-INTERACTION ACCELERATOR

2.1 Apparatus

2.1.1 Accelerator Designs

The accelerators used during this program are shown in Figures 1-4. Note that there are two configurations, short and long. The longer, more heavily instrumented, version was the design originally used during this year's studies. Information gained from it pointed the way to the shorter accelerator.

In the accelerators shown in Figures 1-4, the r-f power enters (from the left) as a TE_{11}, circularly-polarized wave. The r-f power passes through the transition piece and ceramic window into the evacuated region. A continuous flow of un-ionized gas is introduced just beyond the window, and a solenoidal, d-c magnetic field, coaxial with the accelerator is generated by the coils. In the region just downstream of the window, the gas is ionized and its electrons are accelerated in cyclotron orbits by the r-f field. These accelerators are termed "longitudinal-interaction" devices because of the fact that the direction of flow of power from the r-f field to the plasma is parallel with the magnetic field.

As the energized plasma flows down the accelerator it passes through a region of expanding magnetic field which converts the electron paths from transverse cyclotron orbits to longitudinal trajectories. Finally, the plasma ions are accelerated longitudinally by the electric field generated
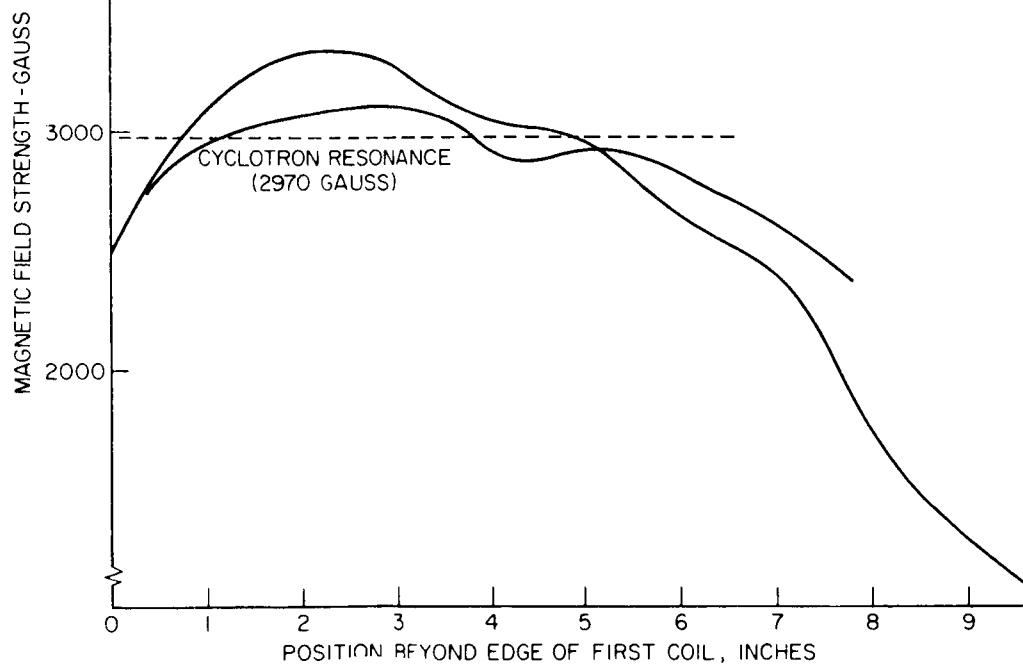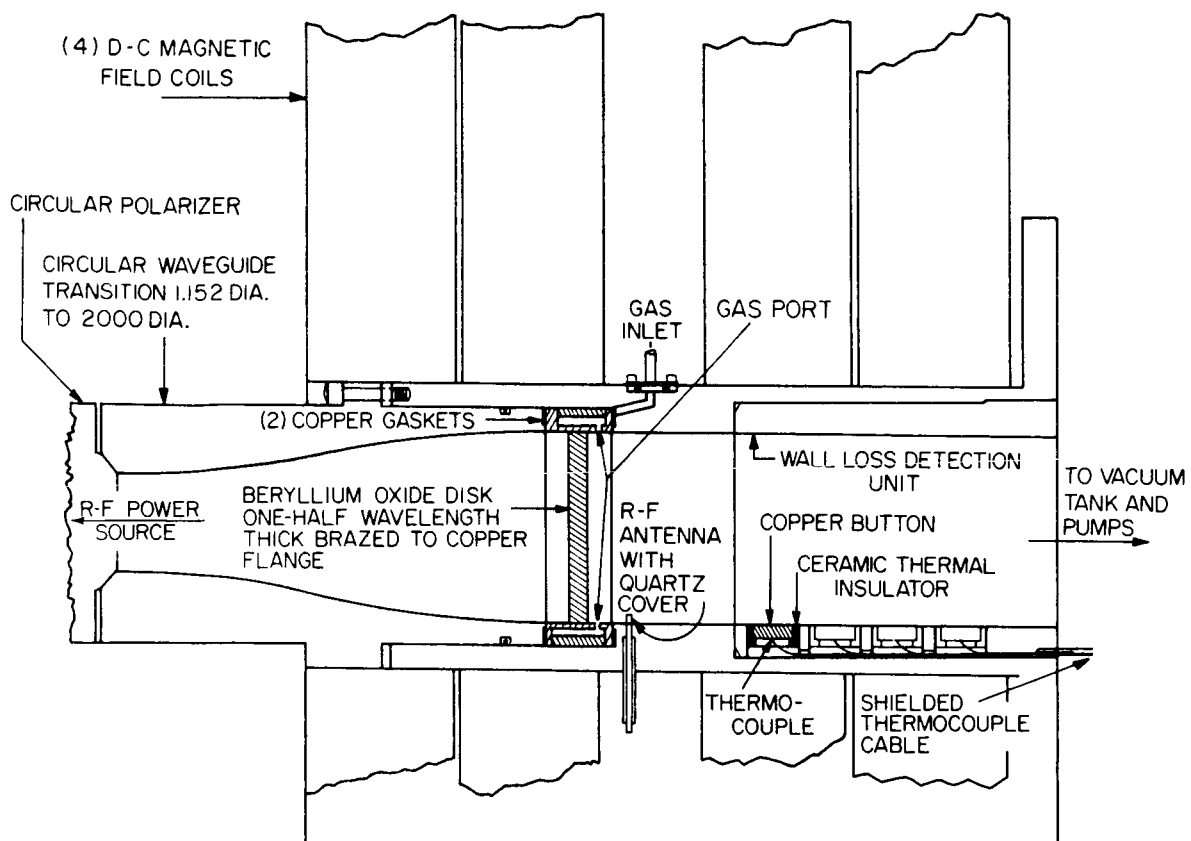
Figure 1. 2" I.D., X-band, Longitudinal - Interaction Accelerator;
Showing Two (of many) Possible Magnetic Field Patterns.
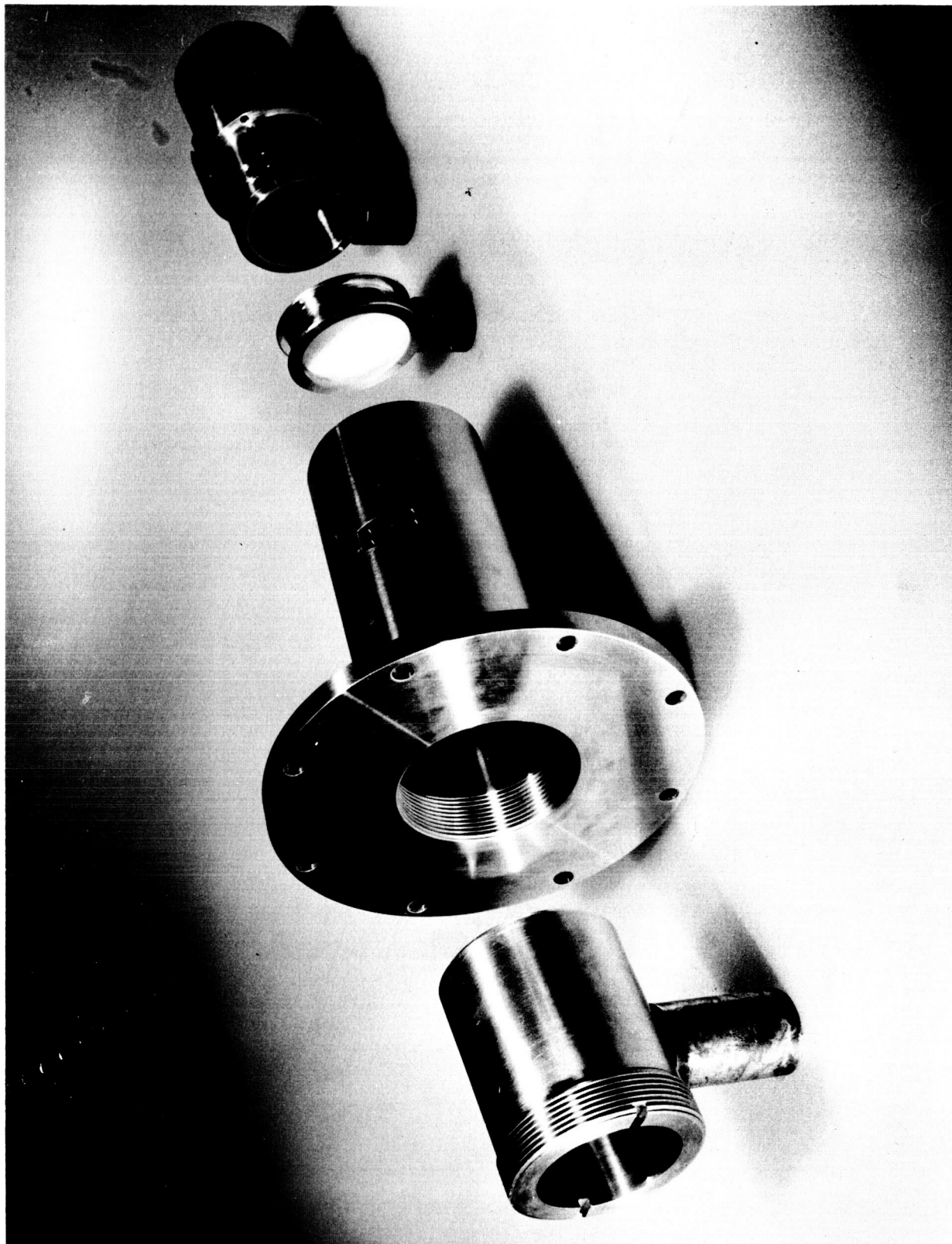
Figure 2. 2" I.D., X-band, Longitudinal - Interaction Accelerator; Photograph of Component Parts Before Assembly.

Figure 3. 2" I.D., X-band Longitudinal - Interaction Accelerator; Engineering Drawings.
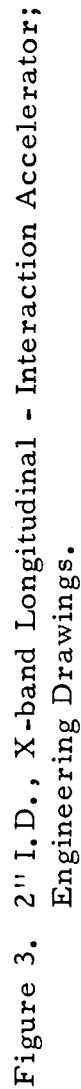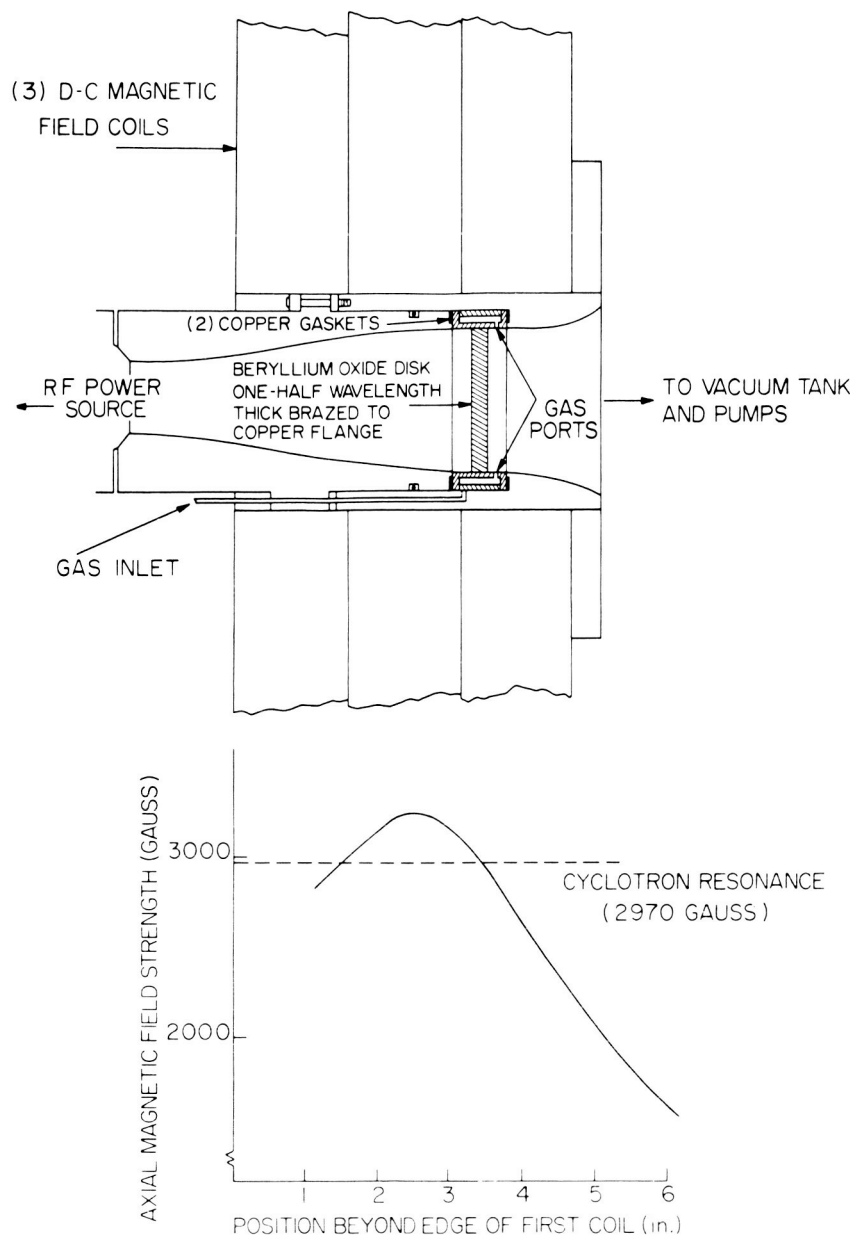
Figure 4a.   Longitudinal - Interaction Accelerator; Short Version
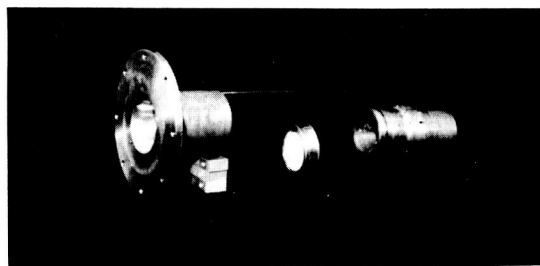
Figure 4b. Longitudinal-Interaction Accelerator (short version), Showing
(from left to right) Plasma Chamber Body with Contoured Exit Orifice, and
Gas Inlet Tube, Beryllium Oxide Window (Peripheral Gas Injection), and r-f
Transition Piece .

as the electrons attempt to separate away from the ions.

Some features of these accelerator designs should be noted. The waveguide dimension was expanded from 1.152 inches to 2.000 inches inside diameter in order to reduce the power density loading on the ceramic window. This creates possible disadvantages which should be explored in future studies: 1). The radial heat flow path length out from the center of the window is increased by increasing the diameter. 2). Increasing the waveguide diameter allows more than just the fundamental TE_{11} mode to propagate. 3). Optical observation of the discharge (see Figure 46) indicates that the majority of the r-f/plasma transfer occurs in a region near each injection port. Thus, as is, the entire cross-sectional area is not utilized, and either the diameter should be decreased, or the number of gas ports should be increased.

A dominating feature of these accelerator designs was to maximize the rate at which heat is carried away from the window. Thus, beryllium oxide windows were used, the copper flanges were made as thick as brazing techniques would allow, and copper gaskets were employed to enhance the heat flow out to the accelerator body. During most of this year's tests with these accelerators, water cooling around the back end of the transition piece was employed. A thermocouple, inserted into a well which extends from the back end of the transition piece up to a point very close to the first copper gasket, is used as an indicator of window temperatures.

The gas flow path is observed from the drawings (Figures 1, 3 and 4) to pass from an annular volume through four radial holes in the window flange. Originally the gas was passed from the annular volume through a radial hole to the center of the ceramic disk and from there out to the evacuated region through a hole along the axis of the ceramic disk. This axial injection along the center of the tube rather than radially at the wall is theoretically preferable and should continue to be considered during future studies. For these 2 inch windows, however, it appears that an intense arc was created within the small radial hole through the ceramic, leading in all cases to destruction of this type of window.

Before the gas reaches the accelerator it passes from a relatively large (1.11×10^4 cm^3) reservoir and through a capillary tube. The flow rate is adjusted by controlling the reservoir gas pressure.

It should be noted that the copper calorimeter buttons, shown in Figure 1, were added after taking the photograph for Figure 2.

Each of the magnetic field coils is driven by its own variable d-c power supply, thereby allowing variations in the shape as well as intensity of the magnetic field. The field strength from a coil arrangement of this sort increases with radial distance away from the coil axis. This results in the desirable feature that the field tends to focus particles away from the walls. Magnetic field strengths are measured by a calibrated flux meter (Sensitive Research Corporation, Multi-Range

Flux Meter, Model FM).

2.1.2   R-f System

The r-f system used to drive this cyclotron-resonance accelerator is shown in Figure 5. The power klystron d-c characteristics are held constant, and frequency and power level are controlled by adjusting the driver klystron parameters. Frequency is measured by the cavity frequency meter in the driver section, while r-f power is determined by the calorimetric power meter, which is matched and coupled to the main waveguide by the tuner and calibrated coupler shown in Figure 5. Reflection coefficient is measured by the pair of thermistor power meters in the calibrated reflectometer setup. In this same reflectometer system, a pair of crystal detectors is included to give signals proportional to incident and reflected power for chart recorder purposes. For each test, then, the following power signals are determined:

1.   Incident r-f power (absolute measurement), by reading calorimetric power meter.

2.   Incident and reflected power (each signal is an absolute measurement, but their relative values are of particular interest), by reading thermistor power meters.

3.   Incident and reflected power (time resolved), permanently chart recorded, to determine time variations in behavior and test durations. A typical chart recording, Figure 6, shows

OSCILLATOR KLYSTRON VA 244E ← FAULT CIRCUIT ← KLYSTRON POWER SUPPLY

↓

ISOLATOR

↓

TERMINATION ← COUPLER 30 DB DBH − 631 → WAVEMETER FXR W410B → CRYSTAL DETECTOR HP − H421A → METER 0 − 50 μa DC

↓

VAR. ATTEN. 0−20 DB FXR W155A

↓

H.V.D.C. SUPPLY & CONTROL

POWER KLYSTRON VA−823J ← FOCUS COIL SUPPLY

↓

FAULT CIRCUIT ← ARC DETECTOR

↓

TO FAULT CIRCUIT

TERMINATION 200 WT. DBH−460 ← COUPLER WAVELINE 569−30 → VAR. ATTEN. 0−20DB HP − H375A → ADAPTER RG51/U → N NARDA 611A → CRYSTAL MA4133 HP 440A

↓

TERMINATION ← CIRCULATOR → TERMINATION

↓

ARC DETECTOR → TO FAULT CIRCUIT

↓

POWER METER HP 430 C

TERMINATION ← COUPLER 30 DB DBH 631 → CRYSTAL DETECTOR NARDA 501R → TUNER FXR N3004 → CALORIMETRIC POWER METER HP 434A

THERMISTOR MOUNT HP 478B

TO VISICORDER

ADAPTER W601 B

VAR. ATTEN 0−20DB FXR W155A ← COUPLER 0−30DB DBH 631 ← TERMINATION — COUPLER WAVELINE 569−40 → COUPLER 30DB DBH631 → VAR. ATTEN 0 − 20DB FXR W155A → THERMISTOR MOUNT HP − H487B

ADAPTER FXR−W601B

TERMINATION

POWER METER HP − 430C

VISICORDER H−1508 ← CRYSTAL DETECTOR NARDA 501R

E−H TUNER FXR−W312B

↓

ADAPTER RG51 RG52

↓

ADAPTER RECT. → CIRC.

↓

POLARIZER DBG − 930 → NOTE: MODIFIED FOR 8.35 KMC/SEC.

↓

PLASMA STREAM INTO VACUUM SYSTEM ← THRUST CHAMBER

Figure 5. R-f System, Microwave Magnetic Accelerator, 8.35 kmc/sec.

time behavior of incident and reflected powers as well as other parameters. The incident r-f power is seen to be steady (neglecting the interfering plasma noise signal), and plasma changes, dependent on other variables such as magnetic field strength, can account for the recorded variations in the antenna probe signal.

A tuner is incorporated in the waveguide circuit to match the plasma load to the waveguide and thereby eliminate reflections. In this way, essentially all of the klystron r-f power may be coupled into the plasma. Between the tuner and the accelerator, the wave is converted to a TE_{11} circular mode and circularly polarized.

2.1.3   Diagnostics Tank

These experiments have been conducted at the GE Plasma Engine Test Facility, sharing this facility with the "Reppac" plasma accelerator program (NAS3-3570) in order to use this facility's high pumping capacity vacuum system and high voltage power supply. In order not to interfere with the "Reppac" studies, however, tests of the cyclotron-resonance accelerator were carried out in a separate tank, attached through a ten inch gate valve to the main chamber. This tank, the accelerator, the d-c coil supplies and some of the microwave and instrumentation components are shown in Figure 7. A drawing of the tank is shown in Figure 8.
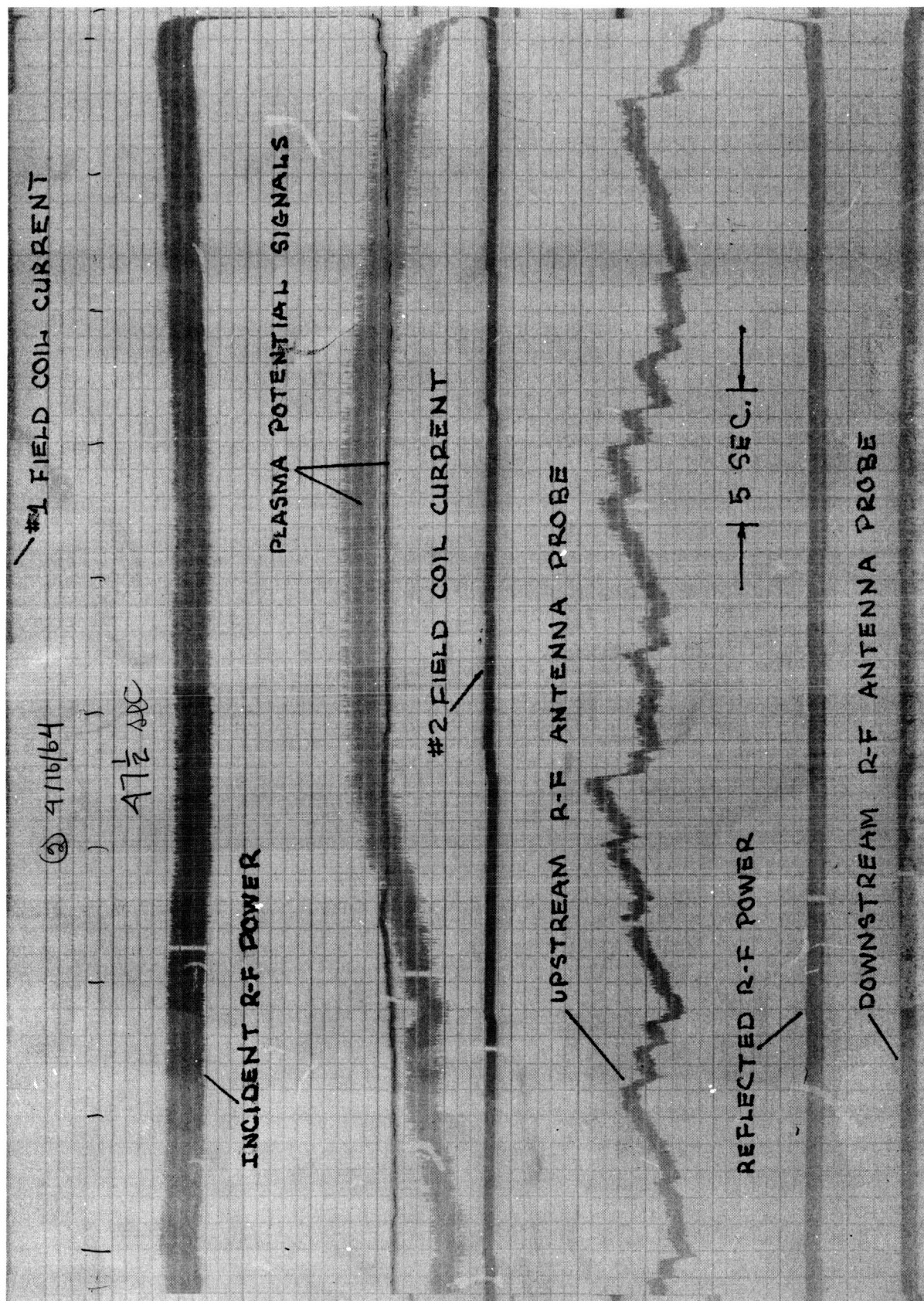
Figure 6. Typical Oscillograph Record.
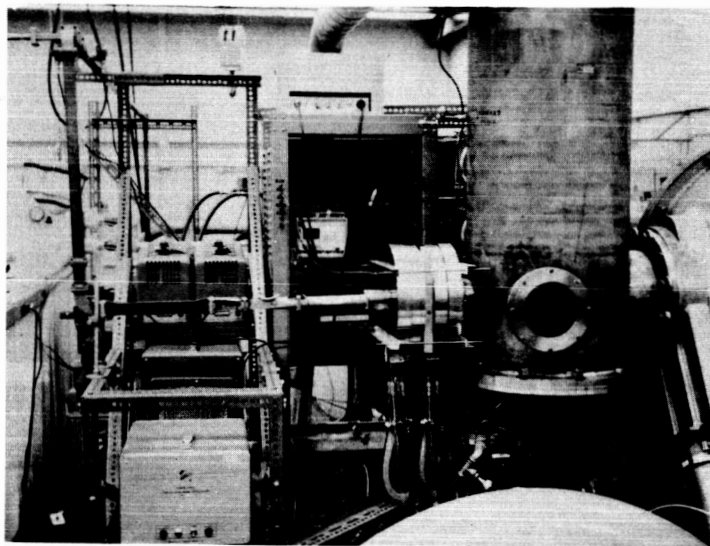
Figure 7a. Microwave Magnetic Accelerator Experimental
Assembly - Accelerator Side
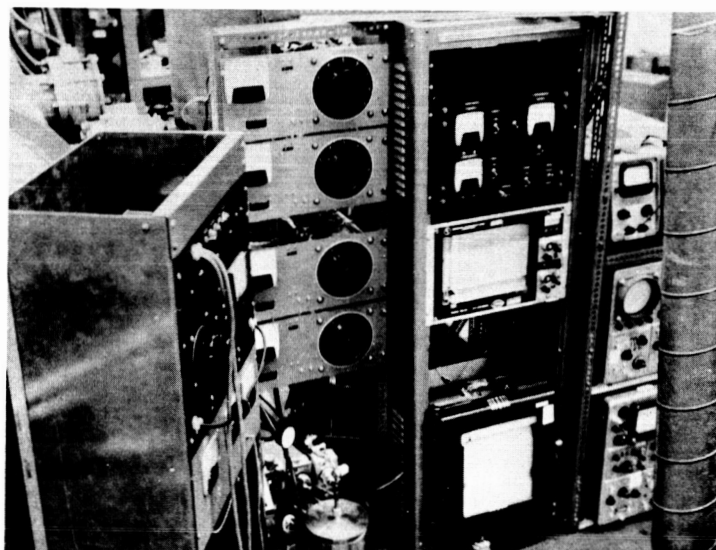
Figure 7b. Microwave Magnetic Accelerator Experimental
Assembly - Instrumentation Side

Figure 8. Diagnostics Tank.

2.2   Diagnostic Techniques

Procedures used for measurement of controllable parameters, namely r-f power, magnetic field strength and gas flow rate, have already been described. Among the dependent (plasma) parameters, determination of r-f reflection coefficient has already been discussed. The following sections cover the various techniques which have been used during this program to measure other important plasma characteristics.

2.2.1   R-f/Plasma Interaction Region

The depth of the boundary region in which the power is transferred from the r-f field to the electrons is important in that it influences the coupling efficiency and it determines the minimum length of the accelerator. Thus, it is important to measure the r-f field strength and its decrease with distance into the plasma.

Antenna probes, extending a short way into the accelerator but shielded from the plasma by quartz covers, are used to measure the strength of the r-f field at two places in the r-f/plasma coundary region. The signals from these probes are detected by crystal diodes and are then displayed on oscilloscopes or oscillographs (e.g., Figure 6). One such probe is shown in Figure 1, located one centimeter beyond the ceramic window. A second probe, identical to the one shown, is positioned two-and-one-half centimeters beyond the window.

2.2.2   Transverse Power Loss

Although a large percentage of the incident r-f power might be coupled to the plasma, large losses of power from the plasma to the

accelerator walls could result in a device with low overall efficiency. Since, as will be shown, overall power efficiency of the Figure 1 accelerator was found to be at most 25%, it became imperative to try and define the losses by making a direct measure of the power going to the walls.

The "wall loss detection unit" shown in Figure 1 was designed for this purpose. In this insert piece are mounted four, thermally insulated, copper buttons whose faces are flush with the accelerator inner wall. The temperature of each is measured by a thermocouple; power is determined from the temperature change of a button during a test of known duration and from the heat capacity of each button.

2.2.3   Sampling Pendulum/Calorimeter

For propulsion purposes it is necessary to determine the power and momentum carried by the accelerated plasma stream. For more complete diagnosis of the plasma engine characteristics, it is additionally desirable to map the power density and thrust density across the stream.

During studies preceding this program (Contract NAS5-1046), a combination pendulum/calorimeter was used for these purposes, and a similar unit, shown in Figures 9-11, was built for these X-band experiments. The pendulum/calorimeter and its support and drive mechanisms are shown, as bench-tested, in Figure 9 and as assembled into the 18" tank, Figure 10. The pendulum/calorimeter itself is a 1-1/2" diameter copper disc, suspended on the end of a counterbalanced glass tube. The temperature of the disc is measured by means of a thermocouple, whose leads are brought out through the pendulum suspension points. An optical technique is employed to determine pendulum deflection. Sensitivities of this unit are as follows:

> pendulum: 93 dynes per centimeter of counterbalance deflection.
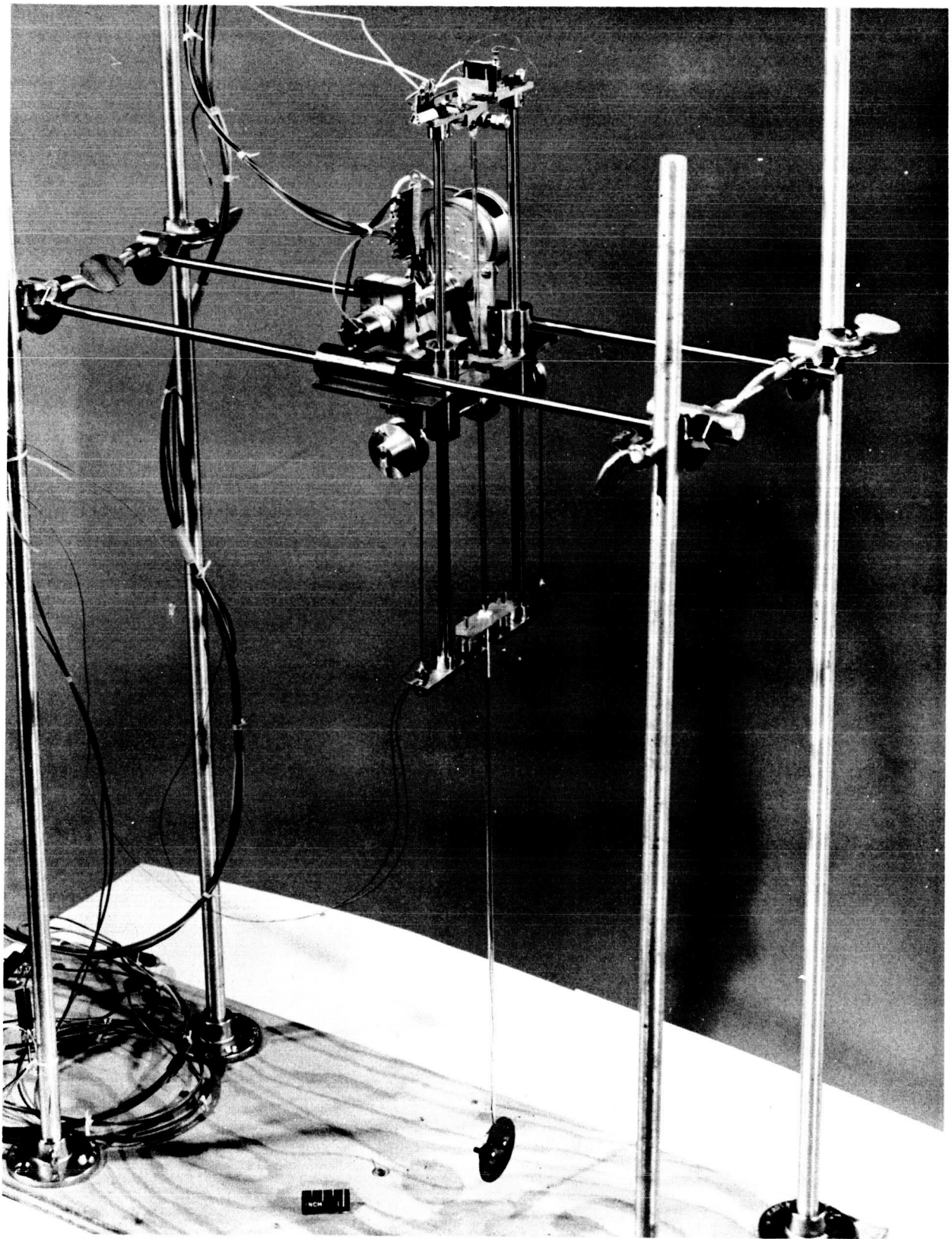
Figure 9. Pendulum/Calorimeter and Carriage System;
Bench-Test Setup.
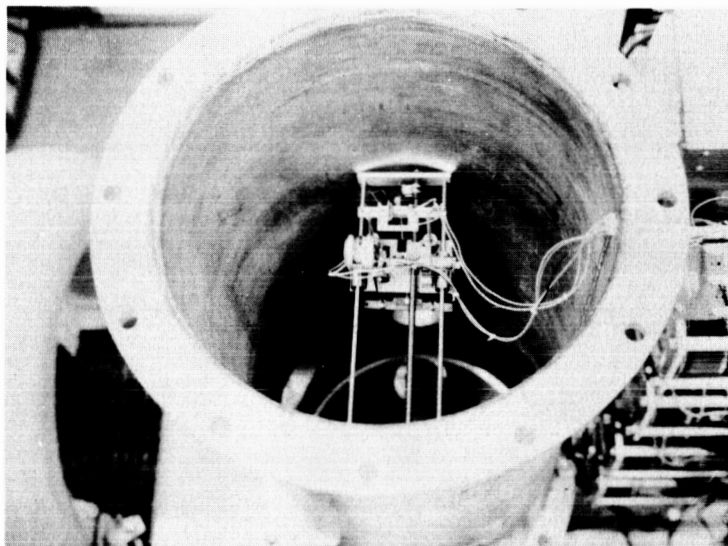
Figure 10. Pendulum/Calorimeter and Carriage System,
Installed in 18" I. D. Diagnostics Tank
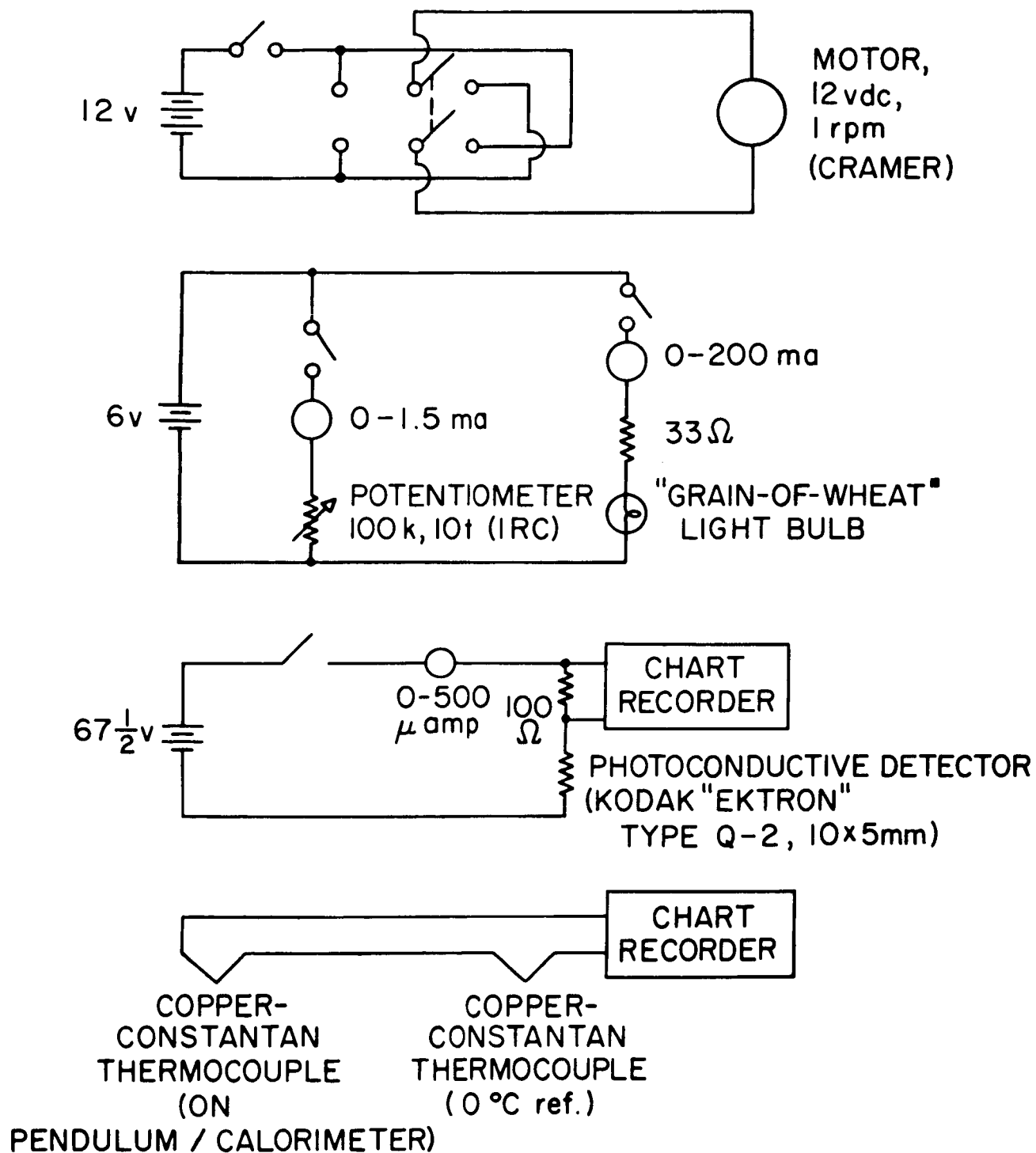
PENDULUM/CALORIMETER INSTRUMENTATION
AND DRIVE CIRCUIT

Figure 11. Pendulum/Calorimeter and Carriage System;
Instrumentation & Drive Curcuit

calorimeter: $12 \pm .8$ joules per $^{\circ}$C.

The horizontal position of the pendulum/calorimeter is varied by a threaded drive which extends through the 18" tank wall and is driven by hand crank which can be seen in Figure 1a. The vertical position is determined by a small d-c gear motor mounted on the carriage unit and is indicated by the setting of a coupled potentiometer, visible in Figure 7. Figure 9 shows details of these instrumentation and drive circuits.

This instrument was, then, designed to be capable of measuring thrust and power densities throughout the entire plasma stream. As will be seen, the calorimetric power measurement was carried out, but the pendulum capability was not employed because of possible electrostatic force interference. The concept of a single sampling probe being moved from point to point was also later discarded in favor of an array of many probes simultaneously operating because of the complex nature of the stream cross sectional profile and also because of the time consuming nature of the single probe technique.

2.2.4 Three-Channel Sampling Probe Array

As a result of the short comings of the pendulum/calorimeter, a new type of probe was developed during this contract's work. This new probe has the capabilities of yielding power density, ion flux density and ion velocity distribution, in other words, more information than could be obtained from the pendulum/calorimeter. Although it was made to be scanned through the plasma stream (using the pendulum/calorimeter carriage), it consists of

-24-

three probes, thereby increasing the speed and thoroughness with which a given plasma stream can be covered. As will be shown, however, the plasma stream from this accelerator is sufficiently random and complex that three simultaneous channels are not enough.

A drawing of this three channel probe is shown in Figure 12, and photographs are shown in Figure 13. This unit is hung vertically down into the plasma stream from a platform which can be moved so that points throughout the entire stream can be probed. Each of the three probes consists of a cylindrical copper housing with end caps. Within each housing, a collector (a copper cylinder with one end closed) is suspended by small-diameter quartz rods. A thermocuple is attached to the back ends of each collector, and these three thermocouples are brought out through the hollow copper support rod and through braided copper shielding to the measurement and recording circuitry outside the vacuum tank.

This probe is mounted in the plasma stream so each collector is "looking" through the 1/2 inch diameter end cap holes at the accelerator. The collectors therefore sample a part of the plasma stream at three different points. This sample of the plasma stream can be studied in two ways by this type of probe. The collector, whose mass is accurately known, acts as a calorimeter whose rate of temperature rise is a function of the power carried by the collected plasma stream. In addition, the collector, through the insulated thermocouple wires, can be negatively biased with respect to the housing so that the flux of ions in the plasma stream can be determined.

TO POSITIONABLE SUPPORT
STRUCTURE & MEASURING
CIRCUITRY

END CAPS(COPPER)

CONNECTING TUBE
(COPPER)

SUPPORT RODS(QUARTZ)

THERMOCOUPLE
(CU-CONST)

0   INCH   1

CYLINDRICAL HOUSING
(COPPER)

CYLINDRICAL COLLECTOR
CUP (COPPER)

GRIDDED ORIFICE
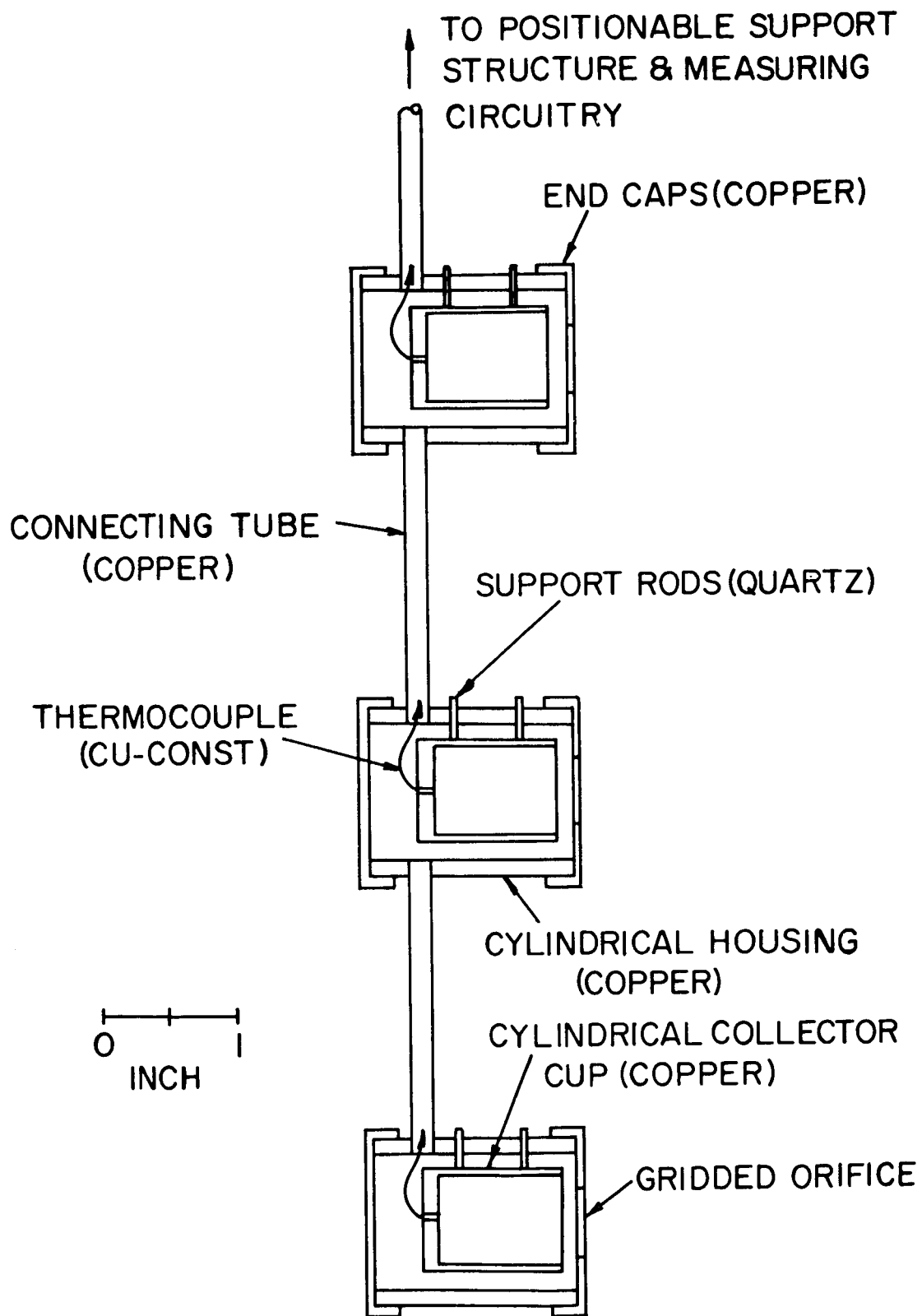
Figure 12.   Three Channel Sampling Probe
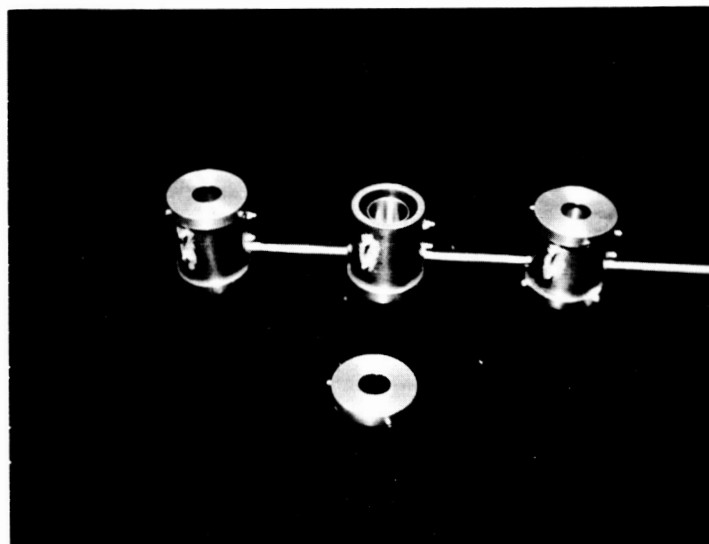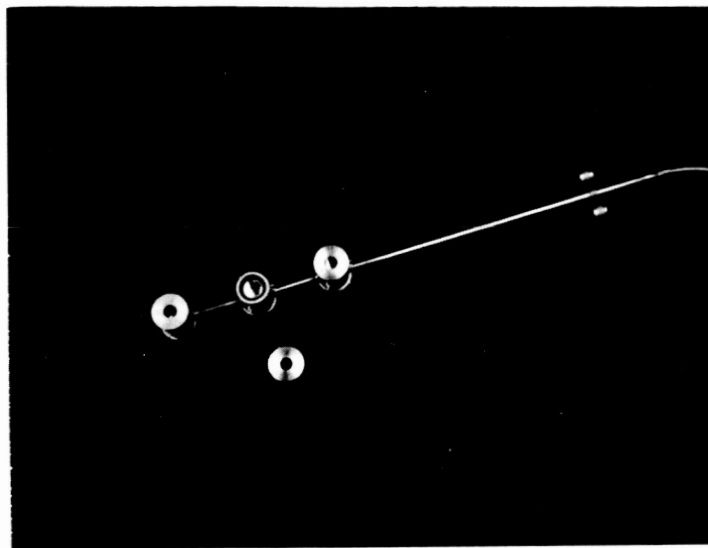
Figure 13. Photographic Views of the Three-Point Plasma
Probe; End Cap Orifice Diameter in one-half inch

Ion velocity distribution may be obtained by noting the change in ion current as the collector is biased at increasing higher _positive_ potentials. So that electron collection by this positively biased collector does not interfere with the ion measurement, the electrons must first be removed from the plasma stream. The three gridded orifice structure shown in Figure 14 was built for this purpose. Unfortunately, confusing results, believed caused by the plasma Debye length being smaller than the grid wire separation, and the press of other more input measurements prevented obtaining more than preliminary information with this instrument.

2.2.5 Sixteen-Channel Sampling-Probe Array

A sixteen-channel sampling-probe array was designed to meet the following requirements:

1) Enough sampling points over a large enough area to yield a valid mapping of a large portion of the plasma stream at one instant.

2) Allow for both calorimetry and ion flux determination.

Drawings of this probe array are shown in Figure 15; see Figure 17 for a photographic view of the assembly and Figure 16 for a view of the total assembled system. Note that, whereas the basic design is the same as the 3-channel sampling probe, the following changes have been made.

1) Each probe has been shortened, and the design allows for easier assembly and repair.

2) Spacing between the collector and the front orifice has been reduced to diminish any space charge limitation effect.

QUARTZ SUPPORT RODS

COLLECTOR CUP (COPPER)

CERAMIC INSULATOR

O_3
O_2
O_1

1/2 INCH DIAMETER
GRIDDED ORIFICES
(TUNGSTEN GRID WIRE)

ALL PARTS COPPER UNLESS
OTHERWISE NOTED

COAX, CABLE (CENTER CONDUCTOR
TO O_2 ELECTRODE)

THERMOCOUPLE
(CU-CONST.)

INCH

0
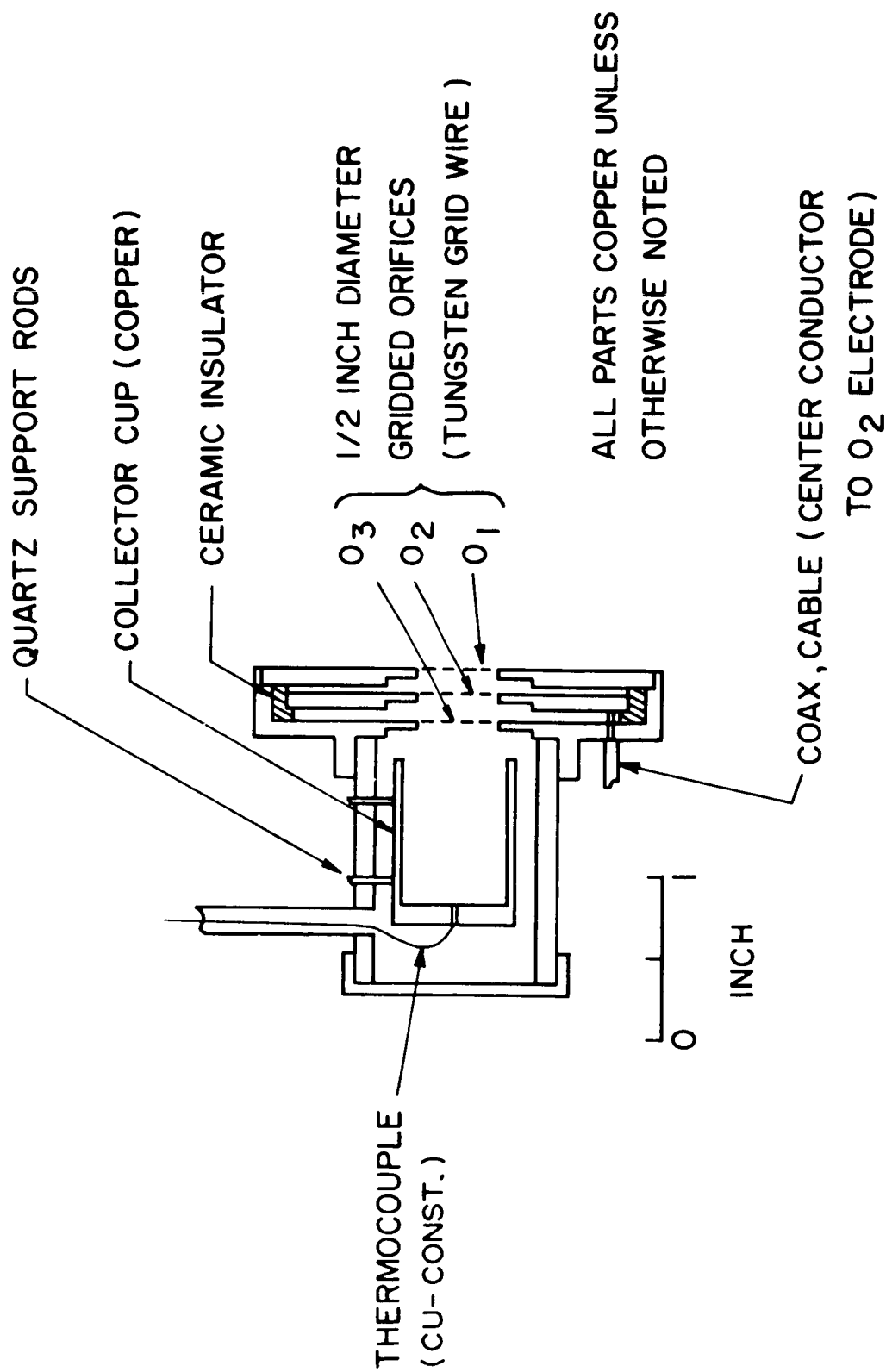
Figure 14.   Retarding-Potential Particle - Analyser Probe

SLIDING VACUUM SEAL

SHAFT (STAINLESS STEEL)

ALUMINUM VACUUM ENCLOSURE
(CYLINDRICAL)

PROBE DETAIL

ALL PARTS OFHC COPPER EXCEPT AS NOTED.

EPOXY CEMENT
QUARTZ TUBE

100 x 100 x .0008
TUNGSTEN MESH

THERMOCOUPLE

(COPPER – CONSTANTAN,
TEFLON & COPPER
BRAID ENCLOSED)

STAKE

PRESS

0   1/4   1/2
INCHES

VALVE

0   2   4
INCHES

"RTV" VACUUM SEAL

THERMOCOUPLE CABLE
(TYPICAL OF 16)

(16) PROBES

VALVE

CYCLOTRON – RESONANCE
ACCELERATOR

36" DIAMETER
VACUUM TANK

PROBE PATTERN

Figure 15.   Arrangement for Operation of Accelerator Directly into 36'' Tank,
Showing the Short Longitudinal – Interaction Accelerator and the
16-Channel Sampling Probe Array in Operating Position.

-30-
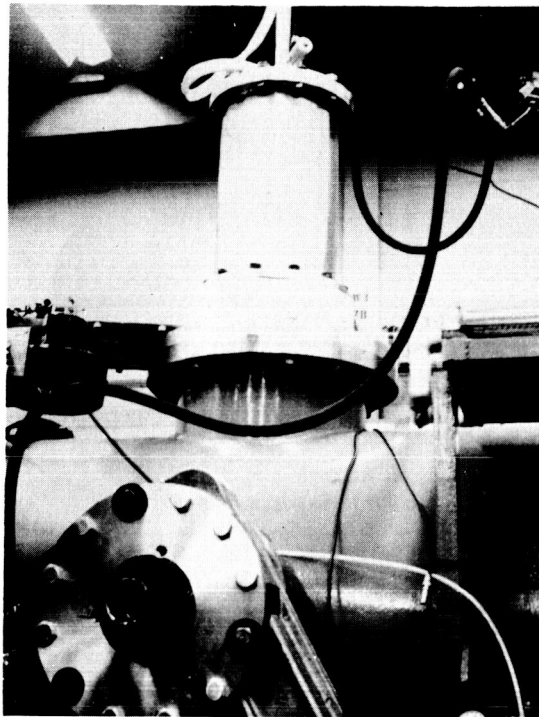
Figure 16. Sampling Probe Array System Mounted on 36" Diameter Tank.
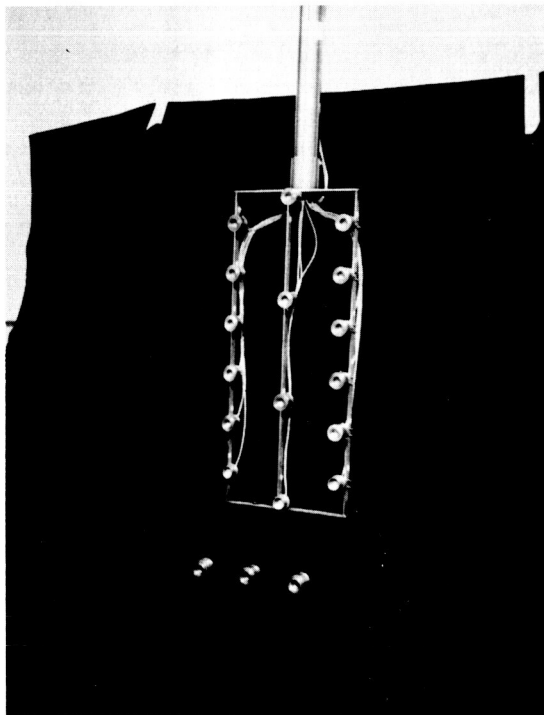
Figure 17. Sixteen-Channel Sampling Probe Array.

3) A much finer mesh screen is now used to provide better isolation between the collector and the external environment.

This probe had to be retractable from the 36" tank in order to allow passage of the large "Reppac" valve. It was also necessary to valve the compartment into which the probe retracts so that it could be installed and removed without needing to shut down the 36" tank pumping system. Fortunately, a 10" valve was located for this purpose, but this of course meant that the width of the probe array had to be limited to less than 10", as shown in Figure 15.

The measurement circuitry for each probe is shown in Figure 18. When the DPDT switch is in the "up" position, connecting the thermocouple circuit to the recorder, a multipin rotary switch is used to connect a single recorder in sequence to each of the 16 probes. The time constant of this probe is sufficiently long so that the temperatures of all sixteen collectors can be taken without need for any cooling correction.

There are 16 microammeters so that ion currents to all sixteen probes can be measured simultaneously. Currents are recorded by taking a photograph of the 16-meter panel, as shown in the photographs of Figure 19. It can be noted from the data in Figure 19 that ion currents are taken for several (in this case three) collector bias voltages, and the saturation currents are interpreted from from the resulting curves. Although only a few tenths of a volt should be needed to reflect the plasma electrons, it is seen that on the order of two hundred volts is needed to reach ion saturation current. This is explained by realizing that, after the electrons have been reflected, the probe acts as an ion diode and is space-charge limited, governed by the well-known Child-Langmuir relation. The large collector voltage is required to "pull across" to the collector all the ions arriving at the grid.
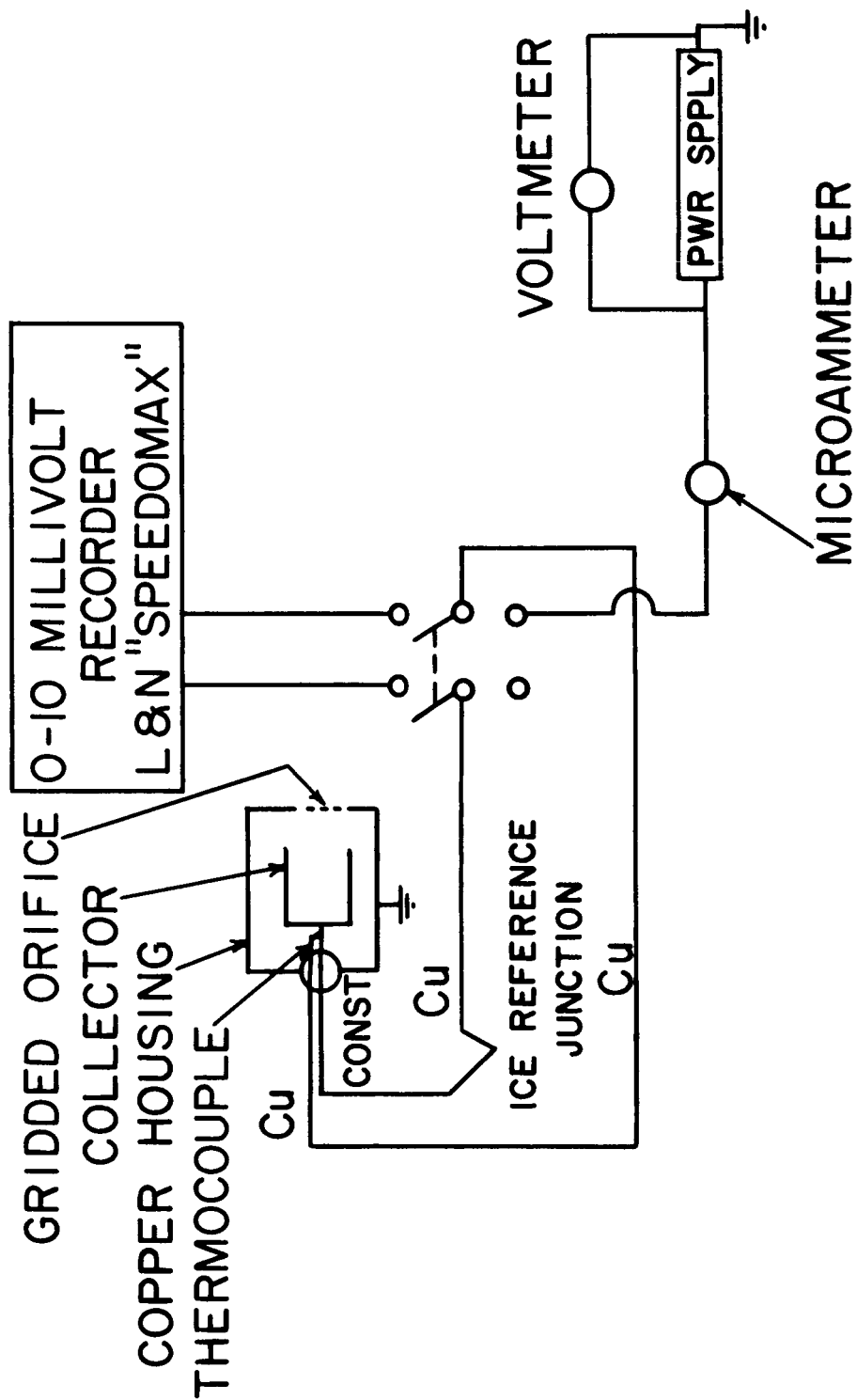
Figure 18. Sampling Probe Circuit (Typical of Sixteen)
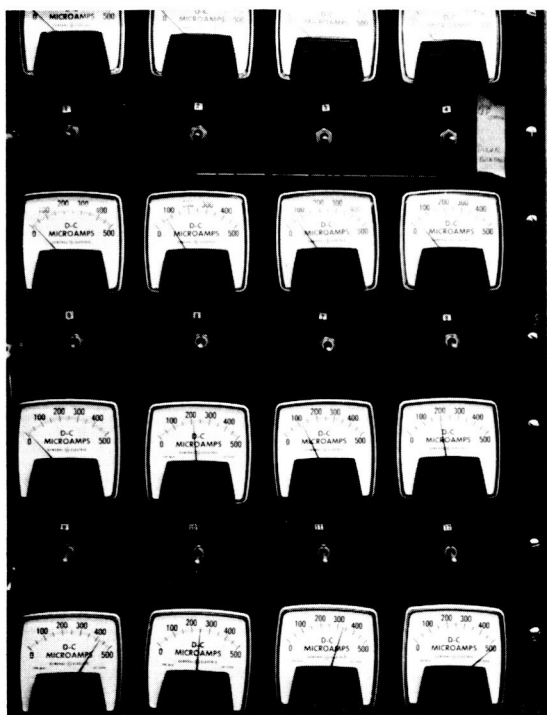
70v
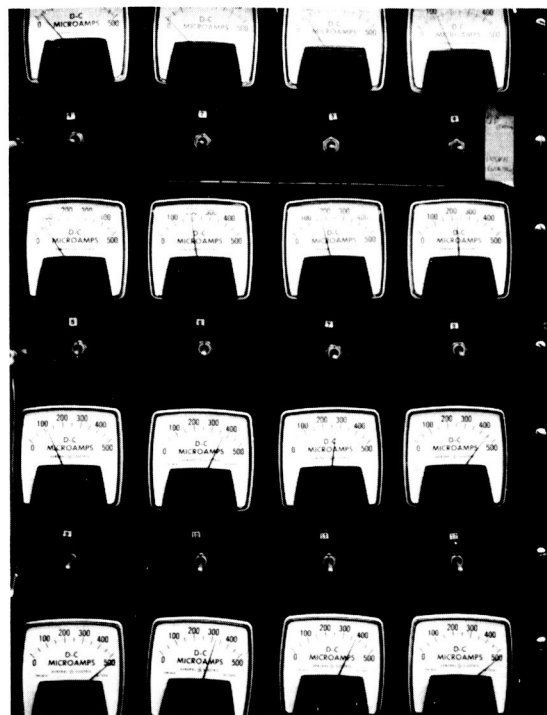
105v
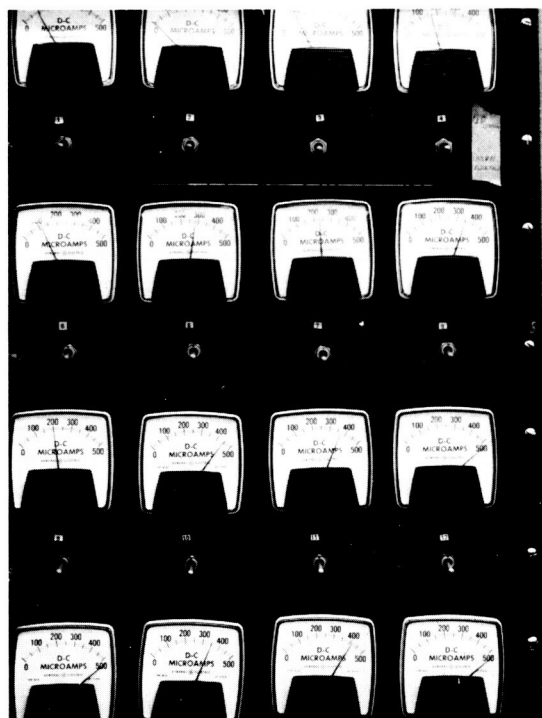
160v

Figure 19. Typical 16-Channel, Sampling Probe Data; 3600 watts,
2.4mg/sec (argon), Magnetic Field as shown in Figure 4a.

2.2.6   Total Calorimeter

Although the sampling probes give a detailed mapping of the stream cross section, the lack of well-defined symmetries makes integration over the total stream a tedious and unreliable procedure for arriving at values for total stream power. The most convenient and accurate method for getting an absolute measure of total plasma stream power is to use a single, large calorimeter which intercepts the entire plasma stream.

A total-stream calorimeter has been employed during this contract work. This calorimeter is a 10 inch diameter by 2 inch deep, cylindrical copper cup with radial baffle fins within the cup to expediate heat transfer from the plasma to the calorimeter. The cup was suspended in the 18" diameter diagnostics tank (Figure 8) so that it was coaxial with the accelerator, with its open end facing and 28 centimeters beyond the accelerator exit orifice.

Originally, thermocouples (three, to insure accurate measurement) were mounted on the back side of this calorimeter, and it was used as a transient device, in the same manner as employed for calorimetry with the sampling probes. This calorimeter has a sensitivity of 538 watt/$^{\circ}$C/sec (from the weight of the cup and the known specific heat of copper), so that intercepted plasma power is determined by multiplying the measured rate of temperature rise by 538. Since the temperature rate is in practice obtained by measuring the calorimeter temperature before and after a known duration test (typically 60 seconds), this method necessarily yields a time-averaged result. The plasma power data reported in Figures 22, 24, and 26 - 29 were taken with this transient total calorimeter.

In addition to the time-averaging feature of the transient calorimeter it had the further undesirable characteristic that it would overheat too rapidly and therefore limit the durations of tests. Both of these objectional features were eliminated by converting the calorimeter to a steady-state device. To do this, copper, water-cooling lines were added to the back side of the cup, and the power was then calculated from the measured water flow rate, the measured difference between inlet and outlet water temperatures, and the known specific heat of water. Water flow rates were generally in the range 500 - 1000 c.c. per minute. At these flow rates, the calorimeter would take a few seconds to reach a new equilibrium condition after a change in plasma power had occurred.

2.2.7 Plasma Space Potentials

Attempts were made during this year's studies to learn something of the charge-separation electric field. Originally, pairs of fixed electrodes were inserted transversely into the stream, and the field was calculated from the measured potential difference which developed between these electrodes. Conflicting results from these probes lead then to use of a single electrode which could be moved along the system axis.

This single electrode potential probe consisted of a 1/4" diameter by 1/4" long copper electrode. This electrode was attached, through a nine inch long quartz tube, to one of the sampling probes on the three channel device (Figure 12); it could therefore scan throughout the plasma volume, since, it will be recalled, the three channel probe was mounted on a movable carriage. The quartz support tube also served as a shield for the copper wire which

connected the electrode to the probe collector and therefore to an external circuit.

Because of sheath effects, the potential assumed by a probe of this sort will not be the potential of the adjacent plasma. Since sheath characteristics change from place to place, even potential differences will not be true, so this probe has not been emphasized. The importance of this measurement is such, however, that greater effort should be expended during future studies to develop more valid techniques.

2.3   Results: Original (Long) Accelerator; Original (Ducted) Window;
            Exhausting into 18" Diagnostics Tank

Initially, tests were conducted with the 2" accelerator shown in

Figures 1-3, using waveguide windows which had gas ducts drilled through

them. Argon was the propellant gas. Incident power levels up to 3200

watts were employed, and flow rates were in the range .28 to .68 mg/sec.

The objective of these tests was to investigate the dependence of operating

characteristics (particularly thrust and power efficiency) on field strength,

flow rate and propellant species. Repeated failure of the waveguide window,

as discussed below, prevented taking the desired systematic set of data.

As described previously, the waveguide window is a disc of high-

density ceramic, 2 inches in diameter and one-half wavelength thick.

Drilled radially from the edge to the center and then out along the axis of

these pieces is a hole through which the propellant gas is injected into the

accelerator. These windows, brazed into copper flanges, yielded very good

vacuum seals and caused very little absorption or reflection of the incident

microwave power. Under plasma conditions, however, when beryllium

oxide ceramic was employed, after perhaps 15-20 minutes total accumulated

operating time, the vacuum would begin to deteriorate; two such windows were

tested. With aluminum oxide ceramic, for the one window tested, the window

lasted only 6 seconds. Upon inspection of the window, it could be seen that

the ceramic (in all three window failures) had cracked along the diameter on

which the gas inlet hole was located. Blackening around the flange end of

this hole suggests that an arc ignited within the gas inlet hole. It then seems probable that this arc caused high enough local heating to crack the ceramic.

Some interesting results have been obtained from the tests which were performed. These results can perhaps best be presented in terms of the various measurement techniques which were applied.

2.3.1 R-f Power

Magnetized plasmas have been generated using power levels up to 3.2 kw. At higher plasma densities, the reflection coefficient has been observed to approach 50%, although this was without benefit of the tuner.

2.3.2 R-f Antenna Probe

In the presence of plasma, the r-f antenna probe signal was observed to decrease and to acquire a strong noise component. Using fast sweep oscilloscope detection, this noise has a random characteristic, although its frequency was observed to be in the 10-50 kc range.

2.3.3 E_z Probe

A two-electrode probe was inserted into the plasma stream in the exit region just beyond the last coil location. The electrodes are separated by one-half centimeter parallel to the flow direction and are directly connected to a high impedance oscilloscope. The high impedance load eliminates signals due to currents flowing from the plasma to the probe, and the essential signal therefore detected by this probe is due to electric fields

within the plasma. While a random component similar to that detected by the r-f probe was present, the major signal observed was a d-c voltage, typically about 10 volts. It is significant that a field of this strength (e.g., 20 volts/cm) can be detected. Of major interest, however, is the total potential through which the ions fall, and therefore no quantitative interpretation of this single point measurement can be made.

2.3.4 Calorimeter

The sampling pendulum described above (Section 2.2.3) is also a calorimeter which measures the power of the incident plasma. While the second BeO window was in good condition, one series of tests using the sampling calorimeter was successfully performed which gives some information on the accelerator performance. During this series, the calorimeter was successively positioned at different radial positions, keeping it always in a plane 26.5 cm beyond the edge of the last coil section, and power density was measured at each point. Simultaneously pressure, incident and reflected powers and magnetic field were monitored to assure constancy of conditions from one shot to another. The results of this series are presented in Figure 20. Note that the plasma stream power quoted in Figure 20 was calculated by integrating over the Figure 20 curve, assuming symmetry about the axis. More recent data, using many simultaneous sampling probes have indicated that no simple symmetry of this sort exists, and the true plasma stream power very probably is significantly different (greater or less) than 475 watts.
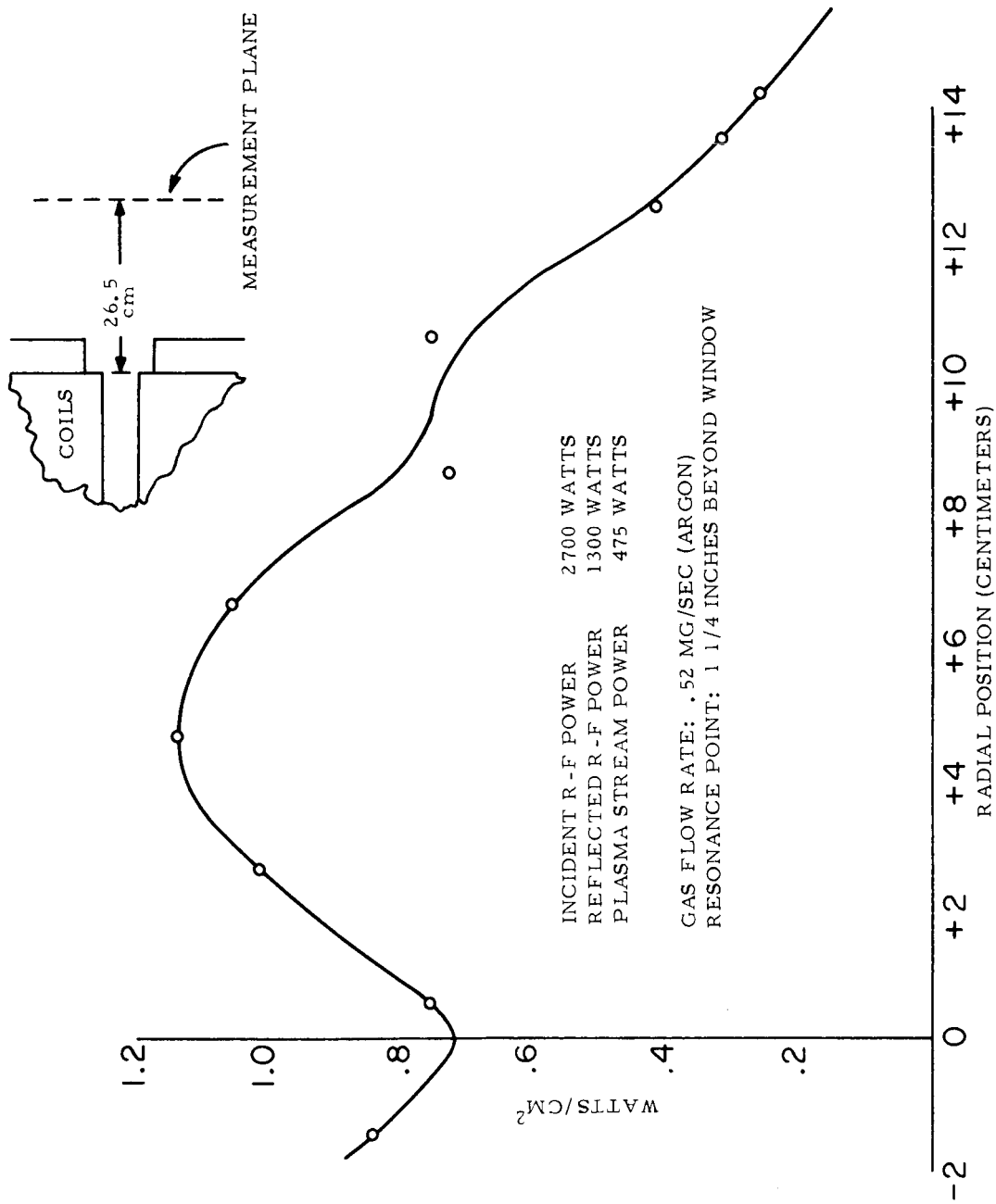
Figure 20. Power Density Profile, Pendulum/Calorimeter Measurement, 2" Beryllium Oxide Window with Gas Duct

2.3.5 Pendulum

Plasma stream momentum is measured by a sampling pendulum as described in Section 2.2.3. The photoelectric detection circuit (Figure 11) as used in these early experiments was not adequately shielded, and its output, during plasma operation, was masked by a strong noise interference signal. The pendulum swing amplitude before and after operation can be observed, however, as shown by the top trace in Figure 21, and from this change, a measure of the thrust on the pendulum by the plasma can be obtained. For instance, in Figure 21, each small vertical division (on the upper trace) is equivalent to approximately 0.4 dynes/cm^2 thrust density. Before the test, the pendulum was quiet, and after the test, it was swinging $\pm$ 3 divisions about equilibrium. This suggests that the plasma thrust density on the pendulum was approximately 1 dyne/cm^2.

It is felt that the photoelectric circuit could be adequately shielded so that the pendulum deflection could be observed during a test. We have observed, however, that, during a test, the pendulum will acquire a potential of 10-40 volts relative to ground, and one therefore wonders to what extent the observed pendulum deflections are electrostatic rather than purely kinetic. To shed some light on this, comparative tests were run with the pendulum floating and grounded. No gross difference in behavior could be observed, suggesting that the electrostatic effect is not dominant. Simple calculations, based on reasonable estimates of pendulum capacitance and electric field do, however, indicate that these measured potentials could represent enough change on the pendulum to create electrostatic forces comparable with the plasma momentum thrust.

-42-
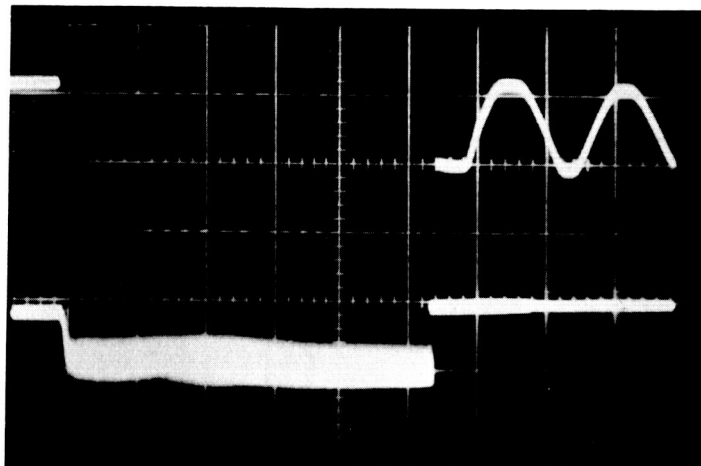
Figure 21. Characteristics of 2" Accelerator (Long Version); Ducted
Window; 2.7 kw, .52 mg/sec, Argon.
　　　　　　　Upper trace: Photocurrent, Indicating Pendulum
　　　　　　　　　　　　Positions, .05v/cm, 5 sec/cm.
　　　　　Lower trace: Reflected Power (Crystal Signal),
　　　　　　　　　　　　.05v/cm, 5 sec/cm.

2.4   Results: Original (Long) Accelerator; Ductless (Flange Gas Injection)
       Window; Exhausting into 18" Tank

The window failure problem was alleviated (although not entirely

solved) by using a solid (ductless) ceramic disc with gas injected radially

through four, equally-spaced, .030 diameter holes in the window flange.

The accelerator configuration (Figure 1) remained unchanged. By the time that

these ductless windows were put into use, additional diagnostics techniques

had been developed so that an extensive study of the accelerator could be

accomplished.

The results reported in the first two sections below were taken using

the total calorimeter as a transient device. For each test, a continuous

oscillograph recording (such as shown in Figure 6) of incident and reflected

r-f power as well as other signals such as r-f probes, electric probes and

field coil currents was made. The duration of the test, usually 30-60 seconds

for these data, was then determined from the oscillograph record. Constancy

of conditions and values of recorded parameters were also read from the

oscillograph record. The calorimeter temperatures before and after the test

were measured with a calibrated, 0-10 mV self-balancing potentiometer/

recorder.

Later, when the calorimeter was converted to a steady-state device,

the same procedures and instruments were employed, but it was not necessary

to obtain a time duration from the oscillograph record.

2.4.1 Magnetic Field Dependence

The power efficiency of the cyclotron-resonance accelerator is found to have a rather broad maximum as a function of magnetic field strength, as indicated by the data presented in Figure 22. The fact that the optimum field strength is somewhat greater than the resonance value (2970 gauss) indicates that plasma diamagnetism is playing an important role and that, as a result, the externally applied field must be greater than resonance to achieve resonance within the plasma. This interpretation is born out by the results shown in Figures 23 and 24. Here we see a rapid transition from an attenuating to a propagating plasma as magnetic field strength is increased through the range approximately 3100 - 3500 gauss. This is typical of a low-collision-frequency plasma as field strength passes through cyclotron resonance, and the high transition field strength (relative to the resonance field) again indicates significant plasma diamagnetism.

A further interesting result is the relation between the wall power loss and field strength, shown in Figure 22. Whereas one might expect greater insulation of the plasma from the walls as field strength increases, it in fact appears that the power loss across the field actually increases with increasing field. It is possible that plasma instabilities and turbulence contribute to this power loss and that such turbulence increases with the field strength. The average wall power density is seen from Figure 22 to be about 2 watts/cm^2. Since the accelerator wall area is approximately 200 cm^2, one can estimate that on the order of 20% of the absorbed r-f
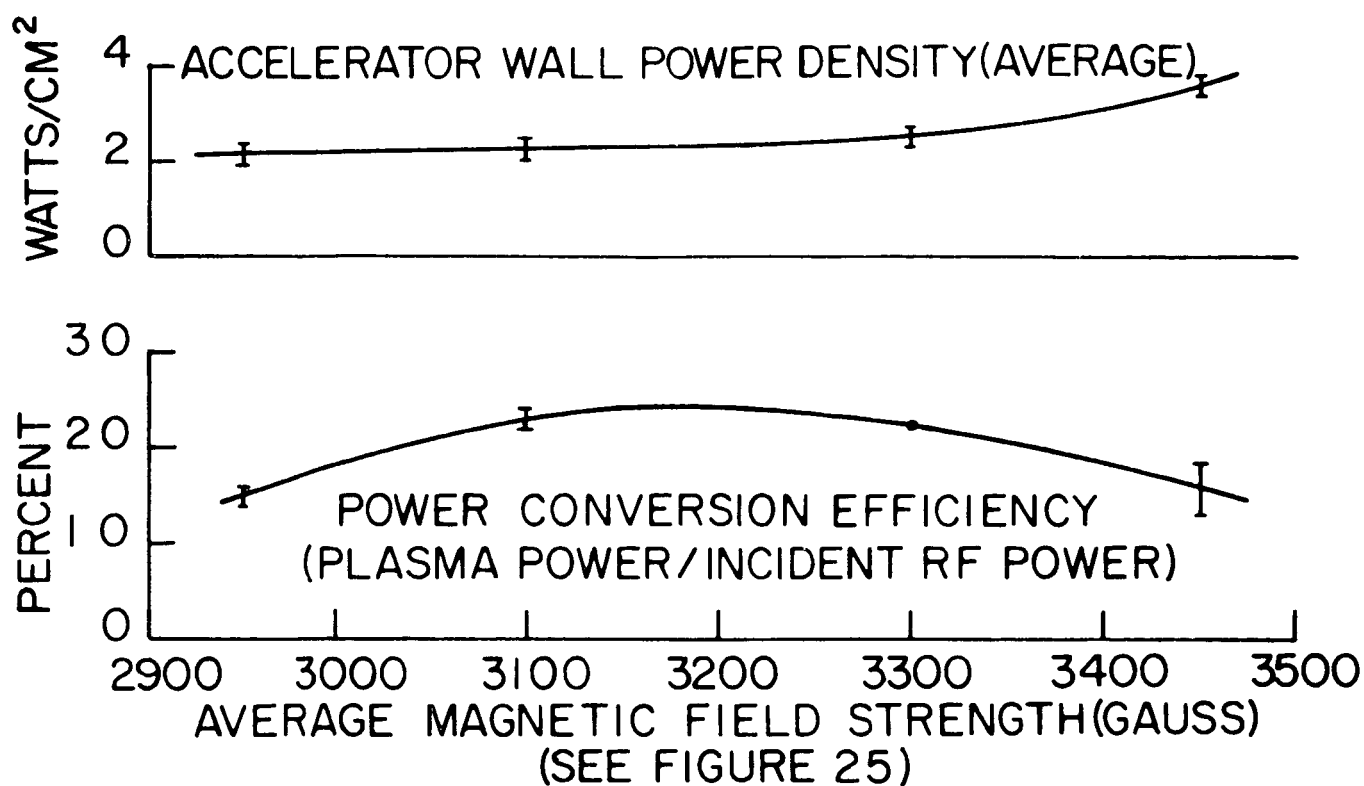
Figure 22. Effect of Field on Power Conversion Efficiency and Wall Power Loss; 2" Accelerator (Long Version); Ductless Window; 2 kw, .40 mg/sec, Argon.
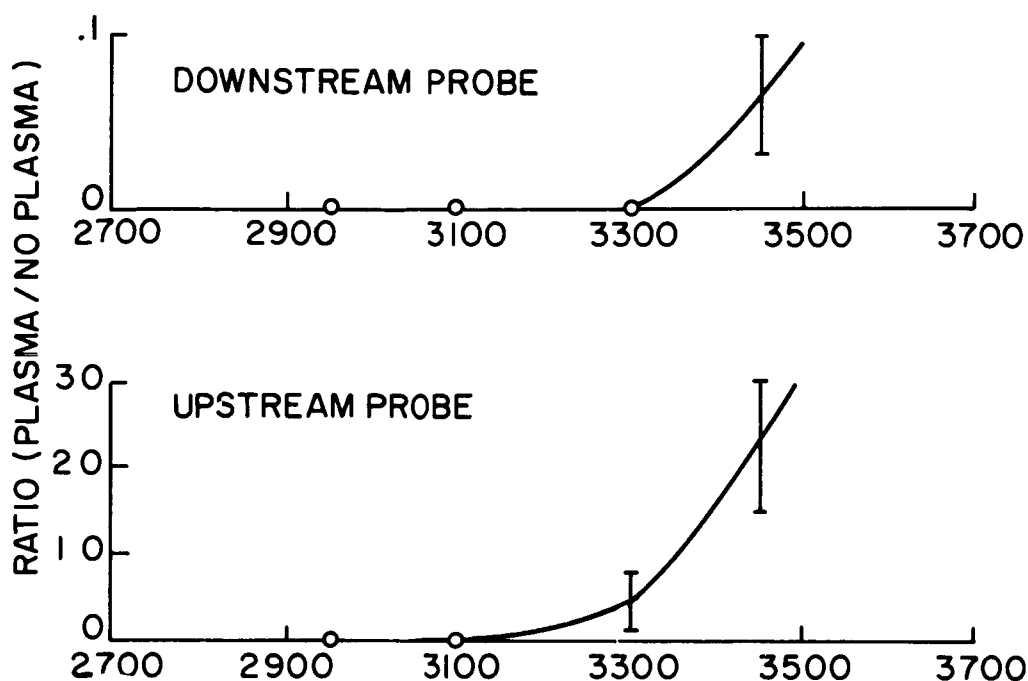
Figure 23. Effect of Field on R-f Probe Signals; 2" Accelerator (Long Version); Ductless Window; 2 kw, .40 mg/sec, Argon.
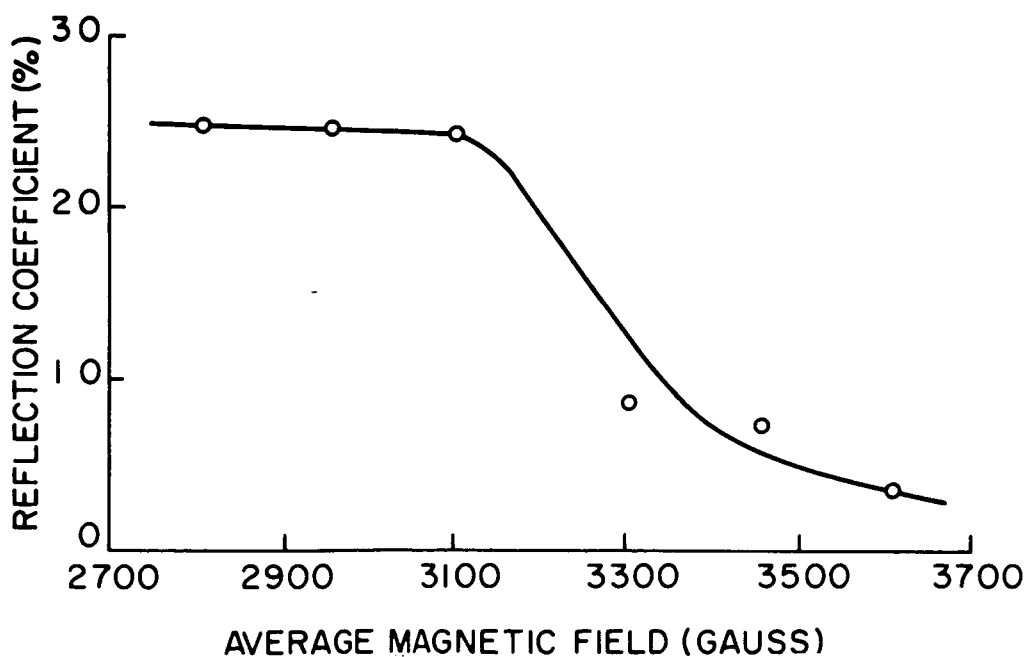
Figure 24. Effect of Field on Reflection Coefficient; 2" Accelerator (Long Version); Ductless Window; 1 kw, .40mg/sec, Argon.
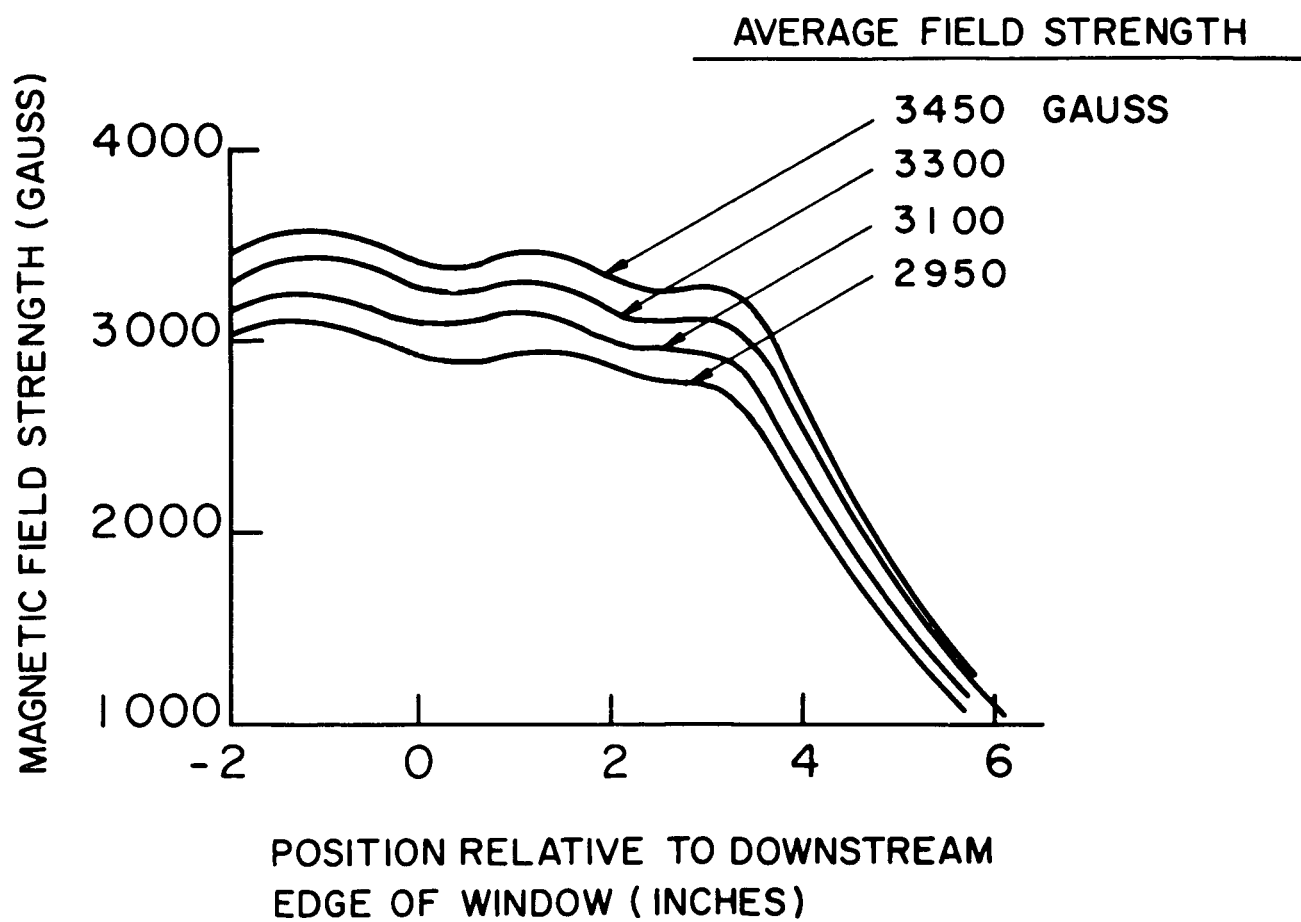
Figure 25. Magnetic Field Distributions used for Figures 22, 23 and 24.

power is being lost to the walls.

Plasma stream characteristics should depend not only on average magnetic field strength but also on the shape of the field and especially the gradient in the r-f/plasma boundary. To study this hypothesis, comparative tests were made with ratios of currents in the four coils such that different magnetic field gradients resulted just beyond the window, however keeping the average field value constant. These results were noted:

1) For 3100 gauss and 3300 gauss (reference: Figure 25), the reflection coefficient increased with increasing gradient. At lower (2950 gauss) and higher (3450 gauss) fields, the reflection coefficient was measured to decrease as the gradient was increased.

2) In all cases, the propagation of the r-f wave into the plasma was enhanced by increasing the gradient.

3) At 3100 and 3300 gauss, the power conversion efficiency (plasma stream power/incident r-f power) remained constant as the gradient was changed. At 3450 gauss, the efficiency increased with increasing gradient, and at 2950, an inverse relationship was measured.

2.4.2   Relationship of Plasma Characteristics to other Controllable Parameters (Including transient calorimeter and wall-loss Calorimeter Results).

In addition to the magnetic field dependencies reported above, it is necessary to study the variations of plasma characteristics on other

controllable parameters, specifically, the polarizer angle, the r-f power
level and the argon[*] flow rate. The results of these parametric variations
are shown in Figures 26-29.

Consider first the polarizer effect. The right-hand circularly-
polarized wave component from which the power is coupled to the cyclotron-
orbiting electrons[**], is maximized for a 45° polarizer orientation, and it
is seen from Figure 26 that this orientation does indeed yield best results.
The fact the opposite (135°) orientation also resulted in very favorable
characteristics indicates, however, either that collision/diffusion effects
are important or that the polarizer is not doing as good a job as desired.
Since magnetic field effects (Figures 23 and 24) show that the plasma is
not collision-dominated, we must conclude that the polarizer needs
improvement. For the magnetic field variation tests of section 2.4.1
and for all tests reported in the following paragraphs, the 45° orientation
was used.

The effect of r-f power level is shown in Figure 27. For these tests
the tuner was left in a fixed setting rather than minimizing reflection for
each plasma condition. As a result, it is seen that the percentage of re-
flected power increased with increasing power, indicating that the electron
density in the r-f/plasma boundary probably continued to increase. Note
that the ratio of plasma stream power to total power continues to increase

*-Helium results will be reported in a later section.

**-Reference: NAS5-1046, Annual Report No. 1, February 1962.

FLOW RATE: .40 MG / SEC (ARGON)

POLARIZER ANGLE

0°

1080 WATTS inc.   245 WATTS
~5% REFL.   PLASMA

WINDOW

45°

1040-1060 WATTS inc.   286-248 WATTS
1-3% REFL.   PLASMA

90°

1040 WATTS inc.   185 WATTS
~20% REFL.   PLASMA

135°

1050 WATTS inc.   230 WATTS
~1% REFL.   PLASMA

POWER DENSITY AT WALL — WT /CM^2

DISTANCE UPSTREAM FROM ACCELERATOR
EXIT – CENTIMETER
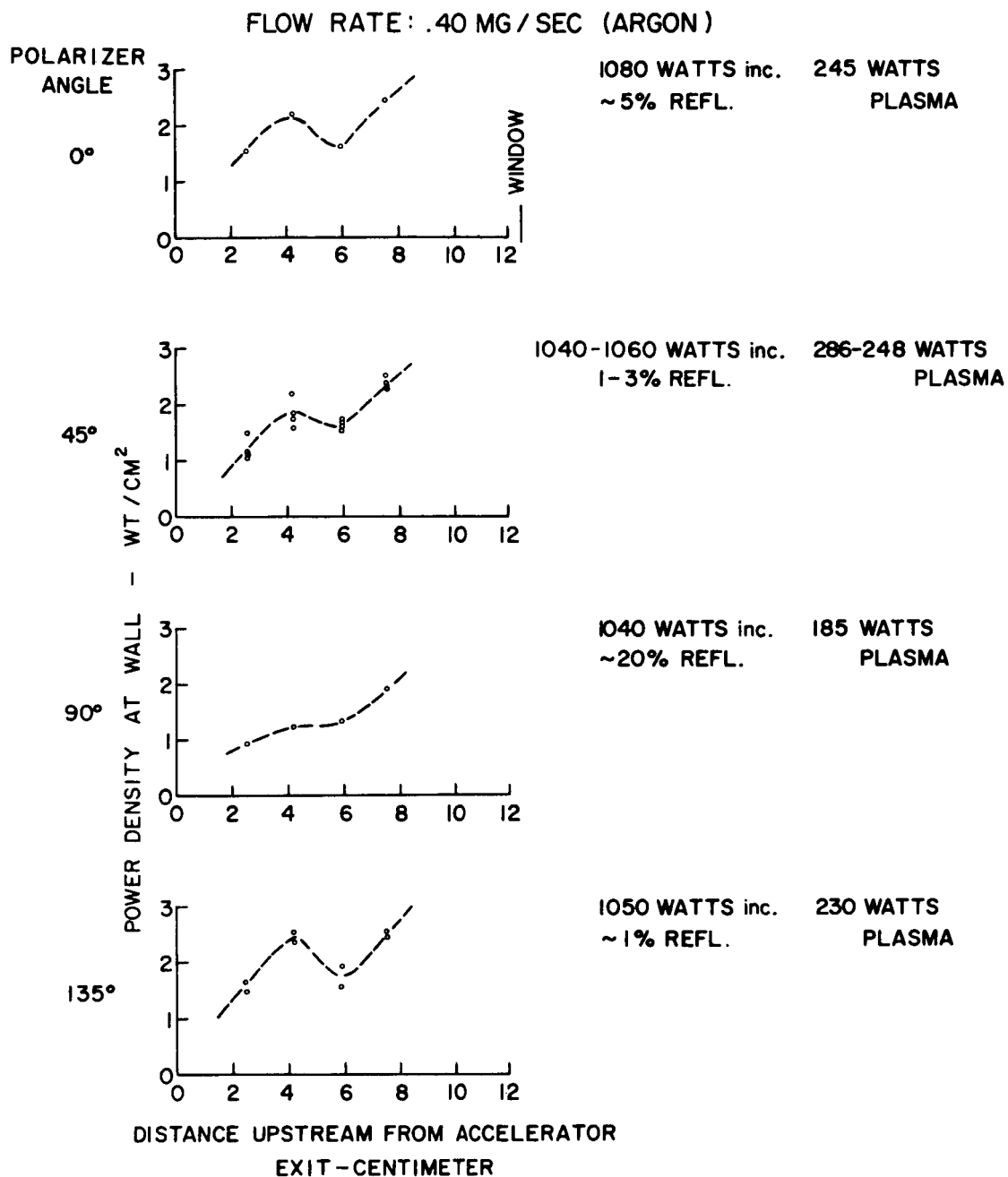
Figure 26.   Effect of Polarizer Angle on Operating Characteristics;
             2" Accelerator (Long Version); Ductless Window; 3300 gauss.

-51-
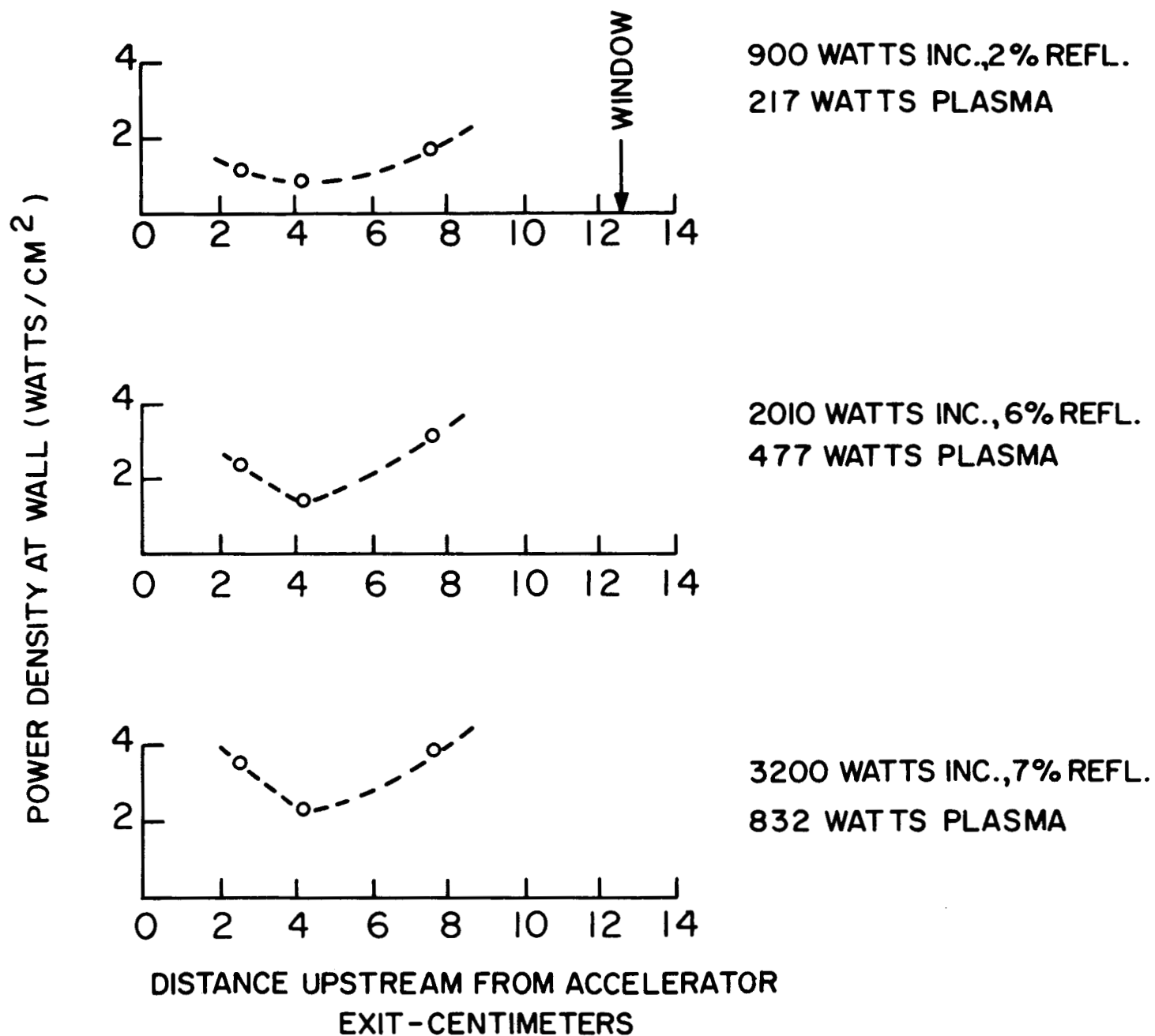
Figure 27. Effect of R-f Power on Operating Characteristics, 2" Accelerator (Long Version); Ductless Window; 3100 gauss, .40 mg/sec, Argon.

The figure shows seven stacked plots of POWER DENSITY AT WALL (WATTS/CM^2) versus DISTANCE UPSTREAM FROM ACCELERATOR EXIT-CENTIMETERS, with the following labels:

.65 MG/SEC   ARGON

1040 WATTS inc ; 4% REFL.
204 WATTS PLASMA

.53

1070 WATTS inc ; 2% REFL.
236 WATTS PLASMA

.45

1030 WATTS inc ; 2% REFL.
254 WATTS PLASMA

.40

1040-1060 WATTS inc ; 1-3% REFL.
247-286 WATTS PLASMA

.35

1030 WATTS inc ; 2% REFL.
200 WATTS PLASMA

.30

1050 WATTS inc ; 3% REFL.
210 WATTS PLASMA

.25

1070 WATTS inc ; 1% REFL.
161 WATTS PLASMA

Figure 28.   Effect of Flow Rate on Operating Characteristics;
2" Accelerator (Long Version); Ductless Window;
1 kw, 3300 gauss.

-53-
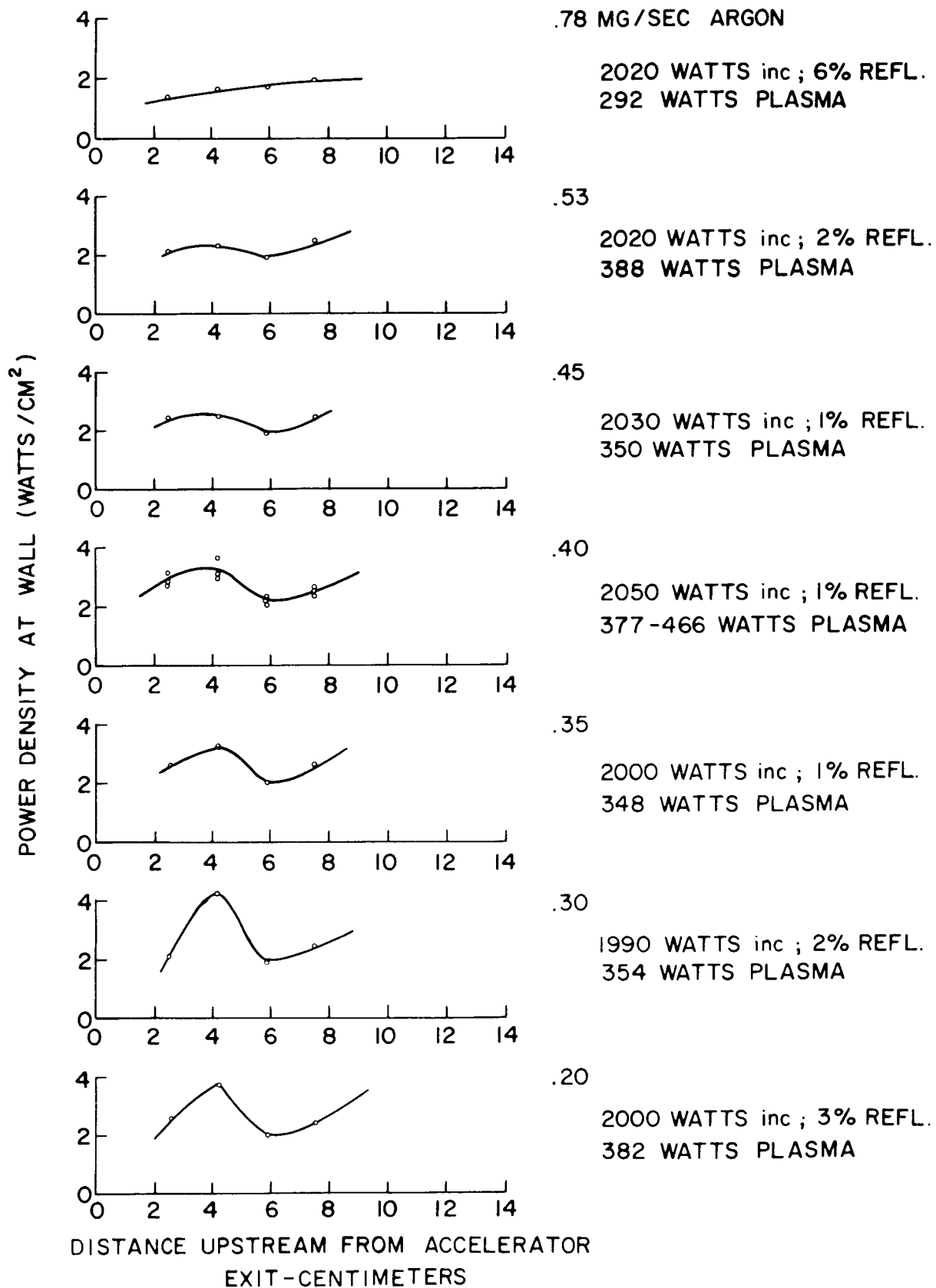
Figure 29. Effect of Flow Rate on Operating Characteristics;
2" Accelerator (Long Version); Ductless Window;
2 kw, 3300 gauss.

with increasing power. Some later results tend to indicate that, for this particular geometry, this ratio levels out above about 3200 watts. The wall power loss is again seen to account for about 20% of the input r-f power.

Figures 28 and 29 show that the power conversion efficiency maximizes for an argon flow rate of about .40 mg/sec. If we assume that the gas is moving at 300 meters/second (approximate sonic velocity for argon) and since the cross-sectional area of the accelerator is 2×10^{-3} m^2, this flow rate results in a neutral gas molecular density of about 1×10^{13} particles/cm^3. Since this is approximately ten times the cutoff density for this frequency (8350 mc), and since one would expect the plasma electron density to be at, but not much above, cutoff, this result suggests that conditions for best power efficiency do not result in best mass utilization. This conjective should be confirmed or denied by further study, in which ideally the actual electron and neutral densities in the r-f/plasma interaction region would be measured.

2.4.3 Steady-state Calorimeter Results

The data taken for the long version of the longitudinal accelerator with the steady-state calorimeter are presented in Table I. This table is arranged with increasing flow rate, increasing field and increasing power, in that order.

Although the test duration is given for each set of conditions, in general, data for more than one set were taken during a single accelerator test. Thus, it is seen that accelerator testing durations were increased considerably when the steady-state calorimeter was brought into operation. In this regard, it might be noted that the accelerator was operated continuously for four minutes and twenty-eight seconds at 2700 watts and for three minutes-eight seconds at 3300 watts.

The severe data scatter which is obvious in Table I is felt to be a problem in inadequate control of accelerator parameters, particularly field strength. Another possible source of scatter is that the accelerator possibly operates in a variety of modes for any given set of controllable parameters, and that different modes are generated from one test to another. The relatively high background pressure for these tests, approximately $1 - 3 \times 10^{-4}$ mm Hg, could contribute to these instabilities.

On several tests it is noted that the best efficiency recorded with the transient calorimeter ($\sim$25%; Figure 22) was approximately repeated. It also appears that helium tends to yield low efficiency.

TABLE I

OPERATING CHARACTERISTICS, ORIGINAL (LONG) LONGITUDINAL-INTERACTION ACCELERATOR, DUCTLESS WINDOW, STEADY-STATE CALORIMETER, EXHAUSTING INTO 18" TANK

Gas Species	Gas Flow (mg/sec)	Average Field (gauss)	Incident R.F. Power (watts)	Power Reflection Coefficient	Plasma Power (Watts)	η_p *	Test Duration (Seconds)
Argon	.30	3350	3200	.11	770	.24	97
"	.30	3450	2200	.08	370	.17	65
"	.32	3200	3400	.09	525	.15	42
"	.40	3350	2000	.06	278	.14	65
"	.40	3350	2620	.11	433	.16	58
"	.40	3350	3120	.12	527	.17	50
"	.40	3350	3200	.09	800	.25	48
"	.40	3350	3290	.14	600	.18	139
"	.40	3350	3300	.24	350	.11	52
"	.40	3350	3620	.18	554	.15	44
"	.40	3450	2200	.08	410	.19	62
"	.52	2900	3400	.20	266	.08	57
"	.52	3050	2800	.20	175	.06	90
"	.52	3100	3200	.25	280	.09	49
"	.52	3200	2700	.11	490	.18	66
"	.52	3200	2800	.07	490	.18	29
"	.52	3200	3300	.14	455	.14	80
"	.52	3200	3350	.06	560	.17	89
"	.52	3300	1500	.09	132	.09	80
"	.52	3300	2200	.11	240	.11	54
"	.52	3300	2850	.10	405	.14	60
"	.52	3300	3150	.19	315	.10	24
"	.52	3300	3600	.18	507	.14	56
"	.52	3350	1100	.27	119	.11	105
"	.52	3350	2000	.14	350	.18	89
"	.52	3350	2650	.17	595	.23	84
"	.52	3350	2700	.14	405	.15	84
"	.52	3350	3200	.09	730	.23	32
"	.52	3350	3300	.06	650	.20	49
"	.52	3350	3400	.11	552	.16	85
"	.52	3350	3550	.15	665	.19	55
"	.52	3350	3730	.10	620	.17	65

$$* - \eta_p = \frac{\text{plasma power}}{\text{Inc. r-f power}}$$

TABLE I   (cont.)

Gas Species	Gas Flow mg/sec	Average Field (gauss)	Incident R-f Power (watts)	Power Reflection Coefficient	Plasma Power (watts)	η_p *	Test Duration (seconds)
Argon	.52	3400	3300	.09	424	.13	72
''	.52	3450	1100	.10	116	.10	91
''	.52	3450	2040	.10	334	.16	77
''	.52	3450	2200	.06	330	.15	82
''	.52	3450	3100	.15	490	.16	60
''	.65	3350	3200	.12	550	.17	53
''	.67	3200	3300	.15	525	.16	81
''	.70	3350	3100	.28	280	.09	65
''	.78	3350	3100	>.30	230	.07	46
''	.78	3350	3200	.10	525	.16	96
Helium	.05	3350	2800	.07	265	.10	71
''	.07	3350	2600	.14	220	.09	80
''	.10	3350	1050	.08	97	.09	68
''	.10	3350	2900	.24	265	.09	76
''	.12	3350	2700	.28	168	.06	141
''	.15	3350	1100	.21	72	.06	85
''	.15	3350	2600	>.37	84	.03	36

$$*-\eta_p = \frac{\text{plasma power}}{\text{Inc. r-f power}}$$

The Figure 22 variation of efficiency with field strength is difficult to interpret from the scattered data of Table I. This type of broad maximum at about 3200 gauss was observed, however, when the field was changed during a single continuous run.

2.4.4   Power Density Measurements, Using the Three-Channel
         Sampling-Probe Array

The three-channel sampling probe (Figures 12 and 13) was used to obtain power density and ion flux density measurements with the original version of the longitudinal-interaction accelerator (Figure 1). Power density measurements will be reported in this section, ion flux data in the next.

The first power density data obtained with this probe resulted in the curves shown in Figures 30 and 31. A reasonable curve can be/through drawn the points for a given accelerator operating point, even though the accelerator had to be shut down several times to allow the probe to be moved to a new location in order to accumulate all the points for a single curve. Many more tests (beyond the Figures 30 and 31 data) were performed using this probe, and in general the resulting data points are much more scattered than in the cases of Figures 30 and 31. The suggestion has already been made in Section 2.4.3 above that the accelerator operates in several "modes" and this scatter in sampling probe data corroborates this hypothesis. A further indicator of this is visual observation of the plasma stream emerging from the accelerator. Rather than being a uniform stream, high-intensity "beams" can be observed, these have been seen to move around during a given test, and, in addition, they do not necessarily reappear at the same location from one test to another.
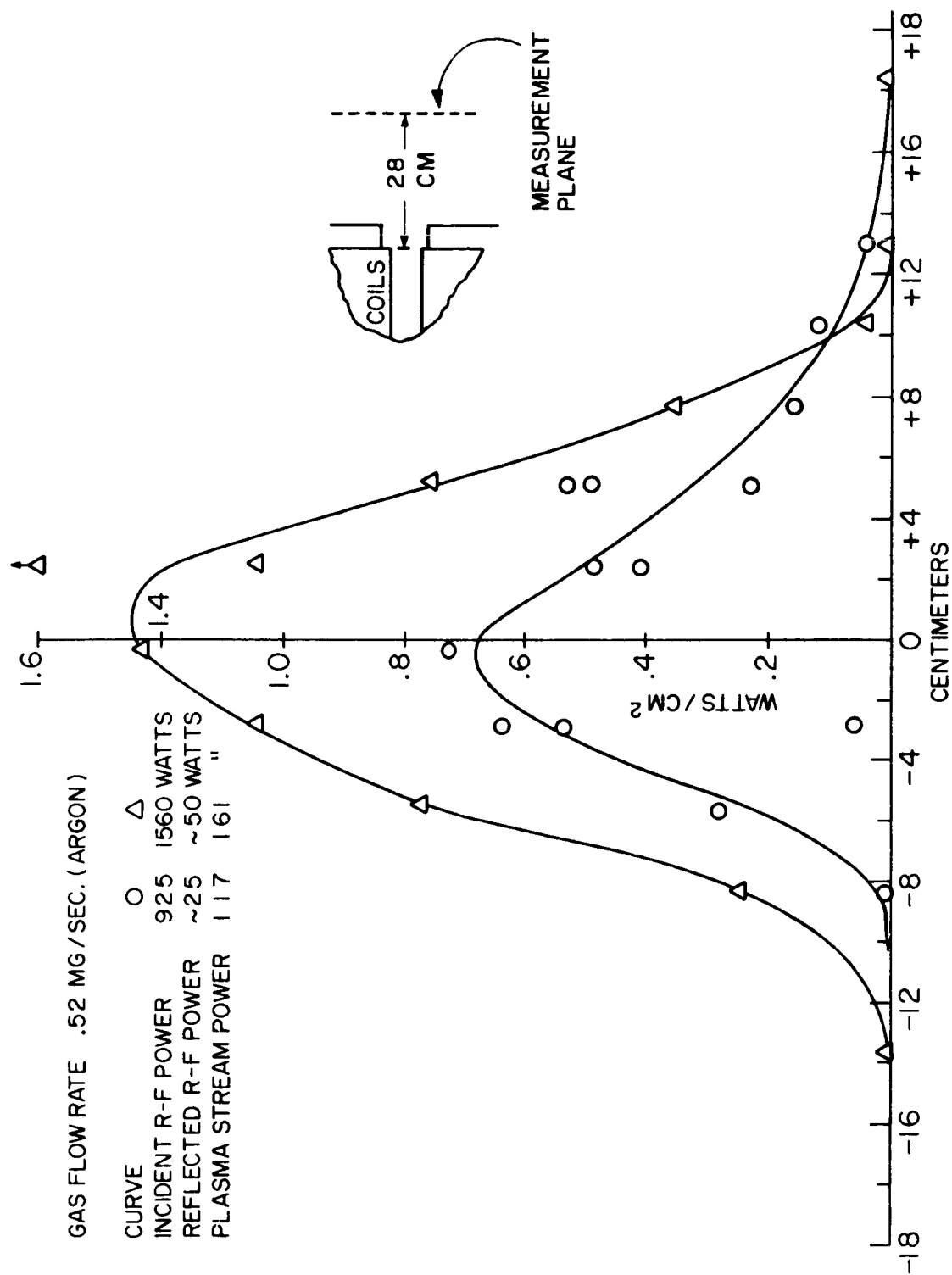
Figure 30. Power Density Profiles, 2" Accelerator (Long Version);
Ductless Window; .52 mg/sec, Argon.
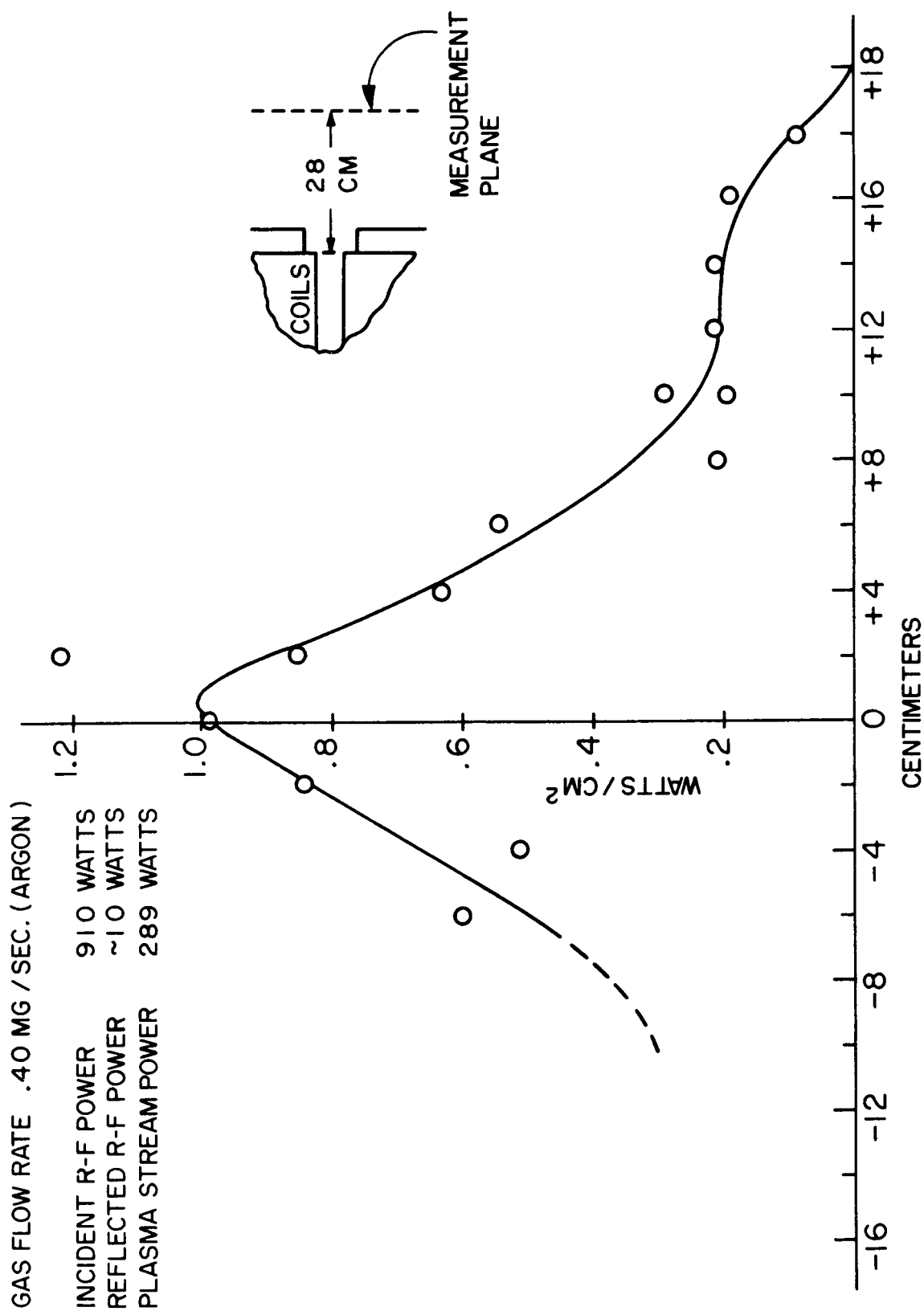
Figure 31. Power Density Profiles, 2" Accelerator (Long Version): Ductless Window; .40 mg/sec, Argon.

Identification of this "beam" type of structure resulted in significant program changes. It led first to the total calorimeter, discussed in section 2.4.3 above, which should not be sensitive to the fact that a high-intensity beam is moving[*]. It led in addition to the development of a many-probe array, so that, if such fine structure did indeed exist, it could be resolved by the use of many probes simultaneously. Finally, it gave impetus to the desire to operate in a lower background pressure environment, since it was felt that the 10^{-4}mm Hg environment in which these measurements were taken could be a significant factor in causing the observed unsteadiness.

It should be noted that the total plasma stream powers quoted in Figures 30 and 31 were obtained by assuming symmetry about the axis and integrating over the curves. This symmetry assumption, as has already been discussed, is open to question.

- - - - - - - - - - - - - - - -

[*] The scatter in total calorimeter data, Table I, indicates, however, that more than mere spacial changes in the plasma stream are involved.

2.4.5   Ion Flux Density and Ion Energy Measurements, Using the
         Three-Channel Sampling-Probe Array

Consider a probe of the type shown in Figure 12 used as a retarding

potential analyzer. For this use, the collector cup is biased with respect

to the housing, and the collector current is measured as a function of bias

voltage. The plasma stream is conceived to enter through the 1/2 inch

diameter orifice in the housing and then to be collected by the collector cup.

As the collector is biased with greater negative voltages, fewer and fewer

electrons will reach the cup, until a saturation level is reached beyond which

no electrons reach the cup, and the ion flux density can be calculated from the

measured saturation current. Similarly for positive biases, the ions are

repelled and one should, from the positive bias portion of the curve, get a

measure of the ion velocity distribution function and electron flux density.

Curve (1), Figure 32 is typical of the original data taken with the

probe as it is shown in Figure 13. Note that, indeed, saturation currents

are reached at both ends of the curve, but note also the comparative magnitudes

of the saturation ion and electron currents. For a neutral plasma under steady-

state (ambipolar diffusion) conditions, one would expect these currents to be

equal, and it was therefore hypothesized that the positive collector bias

potential was "reaching" out through the orifice and collecting electrons over an

effective cross-sectional area that was larger than the orifice itself. To test

this, grid wires were placed over the orifice, and the curve (2) resulted. Note

that this significantly reduced the electron current while not materially
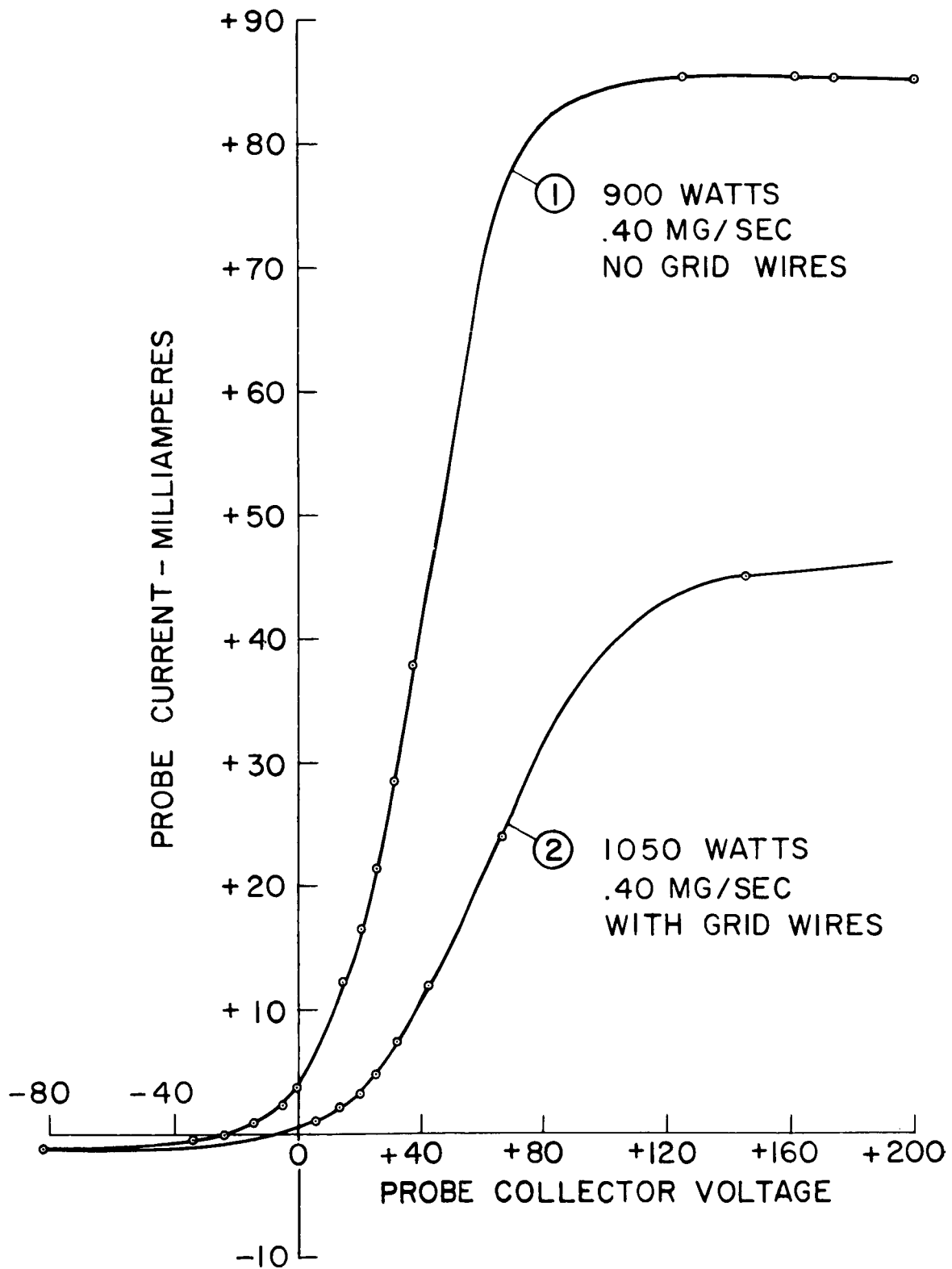
affecting the less mobile

Figure 32. Retarding-Potential, Particle - Analyzer Probe Characteristic
Curves; Without Electron Pre-retardation

ion flux. Thus it would seem that the hypothesis was correct but that the grid was not completely successful in screening the collector potential. Particle analyser probe designs (see sections 2.2.4 and 2.2.5) must provide more adequate isolation of the collector before meaningful measurement of ion velocity distribution can be made.

Comparison of saturation ion currents for curves (1) and (2), Figure 32, indicates that a true measure of ion flux density can be made with this instrument. Measurements of saturation ion current were therefore taken changing argon flow rate and r-f power level, and the results are presented in Table II. It must be noted that these calculations are based on current measurements at only two points in the plasma stream and the effective plasma area must therefore be considered highly approximate. They should be good at least to order of magnitude accuracy, and it is highly encouraging that the mass efficiency is on the order of 10 to 40%.

The particle analyser, Figure 14, was built in an attempt to achieve the isolation needed to measure ion velocity distribution. As mentioned in section 2.2.4, insufficient time was available for proper testing of this unit, but preliminary results do indicate success in achieving the intended goals. For instance, it was observed that, when the electrons were removed by the gridded structure, so that ion saturation current was received by the collector, this collector ion current was brought exactly to zero by sufficient positive biasing of the collector. Thus, it appears that the collector was adequately shielded from the external environment. The ion distribution

TABLE II

Mass Utilization Efficiency (η_m) Measurement

Sampling positions (2), on a diameter 4 cm either side of the system axis, 28 cm beyond the exit of the accelerator.

$$\eta_m = \frac{\text{ion mass flow}}{\text{input mass flow}}$$

Incident r-f power watts	Argon flow rate mg/sec	Probe Currents Probe a ma	Probe b ma	Average Probe Current ma	Average Current Density ma/cm^2	Total Ion Current ma[1]	Total Ion Mass Flow mg/sec.	Mass Efficiency η_m [2]
970	1.1	2.6	2.2	2.4	1.9	380	.16	.1
"	.90	2.5	2.2	2.4	1.9	380	.16	.2
"	.78	2.3	2.2	2.3	1.8	360	.15	.2
"	.65	2.2	1.9	2.0	1.6	320	.13	.2
"	.53	1.9	1.7	1.8	1.4	280	.12	.2
"	.40	1.9	1.7	1.8	1.4	280	.12	.3
"	.30	1.5	1.5	1.5	1.2	240	.10	.3
"	.20	8	.8	.8	.6	120	.05	.3
930	.40	1.5	1.5	1.5	1.2	240	.10	.3
1500	.40	2.3	2.3	2.3	1.8	360	.15	.4

(1) Assumed plasma area: 200 cm^2

(2) Rounded off to one place since these data are only from two sampling points within the stream.

curve obtained by this procedure showed a continuous distribution of ion

energies in the range 40 to 160 ev. It was necessary to place large positive

voltages on the intermediate grid (0_2 Figure 14) to prevent electrons from

reaching the collector. This can be explained if one assumes that the

grid potential actually appears across sheaths around each grid wire, with

electrons actually being collected by the 0_2 grid through these sheaths. A

lower background pressure environment would reduce the influence which such

sheaths play in the operation of this type of probe.

2.4.6 Plasma Potential

The plasma potential profile shown in Figure 33 was obtained with the movable potential probe described in Section 2.2.7. The total potential change is no where near the expected ion energy nor is it large enough to account for the ion energies measured by the analyser (Section 2.4.5), but these facts can be explained on the basis of the potential across the probe sheath. The observed potential minimum, which is approximately at the exit orifice of the accelerator, is more difficult to explain. It would certainly lead to particle oscillation within this potential "well" and in general would have a deleterious effect on accelerator performance.
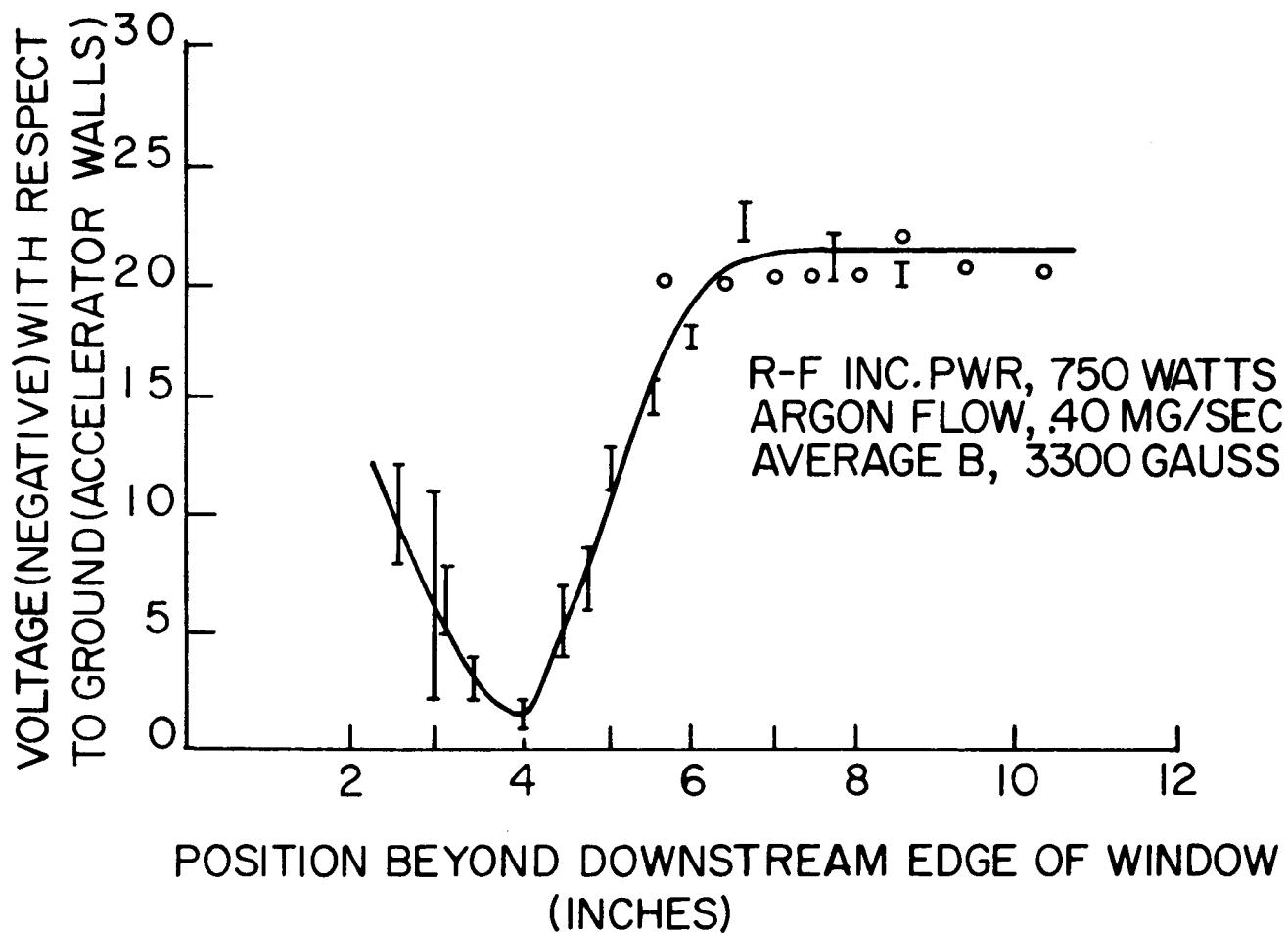
Figure 33. Plasma Potential Profile - On Axis

2.5 Results: Short Accelerator; Ductless (Flange Gas Injection) Window; Exhausting into 18" Tank

It has been shown that, for the original (long) accelerator (section 2.4), the r-f power is absorbed within one or two centimeters beyond the ceramic window. It has further been shown that a significant amount of power ($\sim$ 20%) is being lost from the plasma to the side walls of the accelerator. Thus, it seemed that a large improvement in accelerator performance could be achieved by shortening the design. The short version of the longitudinal interaction accelerator (Figure 4) was accordingly constructed. Results obtained with the short accelerator are described in this section.

Table III presents characteristics of the short accelerator (Figure 4), firing into the 18" diagnostics tank using the steady-state, total calorimeter for measurement of plasma stream power. These are conditions identical with those for the long accelerator when the Table I data were obtained, so these two Tables (I and III) provide a good measure of the effect of shortening the accelerator. The important result, of course, is the significant increase in power efficiency.

The most obvious reason for attaining these favorable results is the shortening of the plasma chamber, thereby presumably recovering a good portion of the power which, in the longer accelerator, had been measured to be going into the plasma chamber walls. It is probable that the increase in the field gradient adjacent to the window was also beneficial. A third, possibly influential change from the earlier design is the contouring of the exit orifice (compare Figures 1 and 4).

-71-

TABLE III

OPERATING CHARACTERISTICS, SHORT
LONGITUDINAL-INTERACTION ACCELERATOR,
DUCTLESS WINDOW, STEADY-STATE CALORIMETER
EXHAUSTING INTO 18" TANK, ARGON

Test	Argon Gas Flow (mg/sec)	Window Field* (gauss)	Incident R-f Power (watts)	Power Reflection** Coefficient	Plasma Power (watts)	Plasma Power / Inc. R-f Power	Test Duration (seconds)
1	.52	2980	1600	.24	640	.40	105
2	1.8	2980	1600	.24	640	.40	76
3	1.8	3220	1600	.21	640	.40	50
4	.14	2980	2500	.19-.22	990	.40	64
5	1.0	2980	1520	.23	630	.40	66
6	1.0	2980	3200	.21-.23	1610	.50	62
7	1.0	2980	3450	.20-.23	1610	.46	100
8	1.0	2980	3150	.01-.02	1650	.52	94
9	1.0	2980	3100	.01	1540	.50	150
10	1.0	3100	3200	.01	1370	.43	100
11	1.0	2980	2600	.02	1400 ± 70	$.54\pm.03$	203
12	1.0	2980	1250	.04	560	.45	86
13	1.0	2980	2800	.01	1150	.41	88
14	1.0	2980	2250	.02	1050	.47	99

*-See Magnetic Field Curve, Figure 4.

**- Note that tuning was performed between Tests 7 and 8.

2. 6   Results: Short Accelerator; Ductless (Flange Gas Injection)
            Window; Exhausting into 36'' Tank

During the last month of this contract period, the short accelerator

was operated directly into the 36'' tank, as shown in Figures 15 and 16.

This change achieved a ten-fold improvement in background pressure, and

it is important that the accelerator operated successfully in this lower

density regime.

Since any probe which was to be used for plasma diagnostics in this

arrangement had to be limited to a width of less than 10'' (as discussed

in Section 2. 2. 5), a total calorimeter was out of the question. It was

decided, therefore to take this opportunity to obtain experience with a

sampling probe array having many probes. The resulting 16-channel probe

is shown in Figures 15 and 17 and is discussed in detail in Section 2. 2. 5.

Power density and ion flux density contour plots taken for the short

accelerator using the 16-channel array are shown in Figures 34 - 45. It

can be seen from these contours that the probes are near enough together

to resolve the important variations in the patterns. It can also be seen that

no well-defined symmetries exist and the patterns are in fact somewhat

complex. As a result, since the array was not large enough to cover the

entire stream cross section, integration over these patterns cannot be per-

formed to yield total power and flux values.

Sufficient coverage and symmetry do exist in most of the patterns,

however, to see that the stream is more confined that would result if

particles did follow field lines. For example, the flux and power densities

--- EXPERIMENTAL DATA
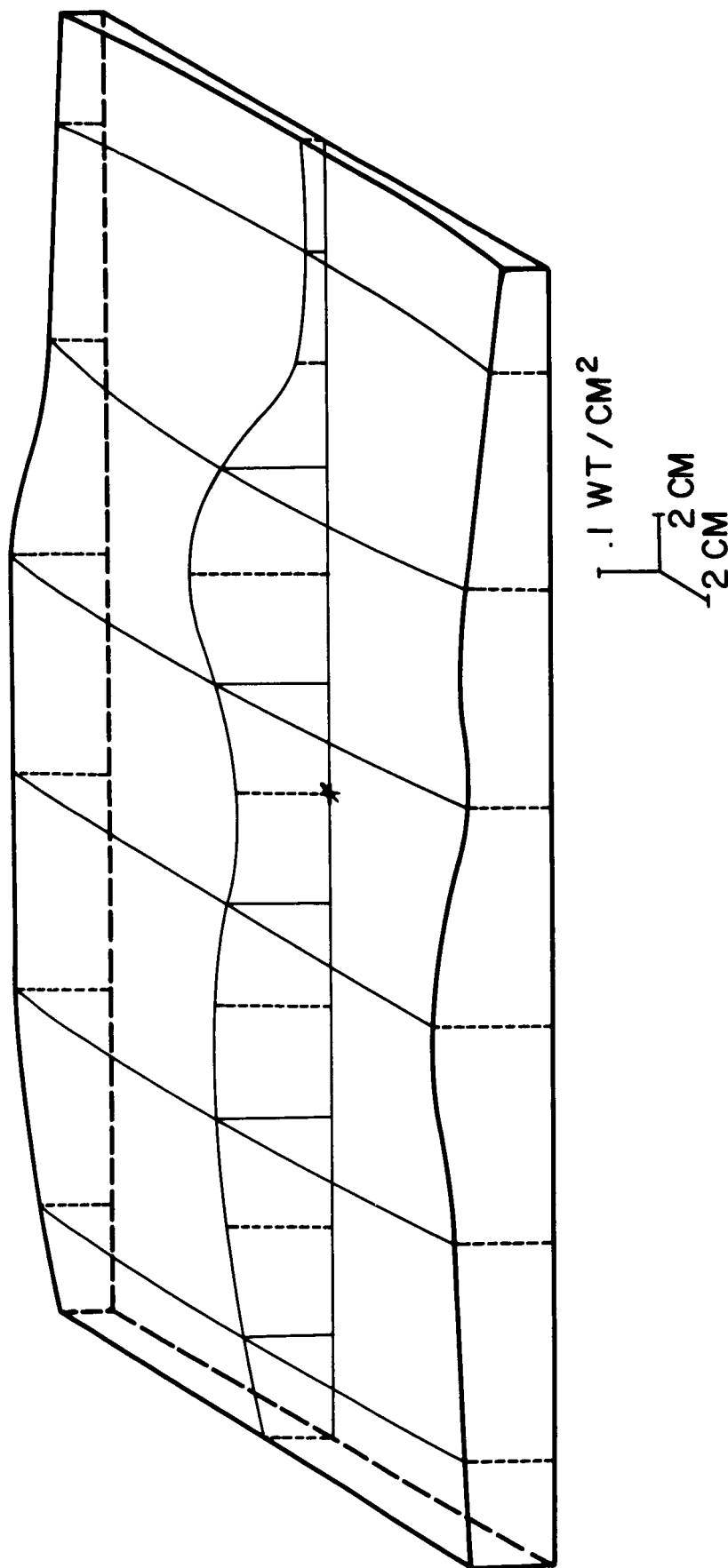
.1 WT/CM²

2 CM

2 CM

Figure 34. 2" Accelerator (Short Version); Ductless Window; Power Density Contour Map; Figure 4a Magnetic Field Distribution; Incident R-f Power 2150 Watts, Reflection Coefficient 2%, Argon Flow Rate 5.0 mg/sec.

EXPERIMENTAL DATA ----

.1 WT / CM²

2 CM
2 CM

Figure 35. 2" Accelerator (Short Version); Ducless Window; Power Density
Contour Map; Figure 4a Magnetic Field Distribution; Incident R-f
Power 2100 Watts, Reflection Coefficient 1%, Argon Flow Rate
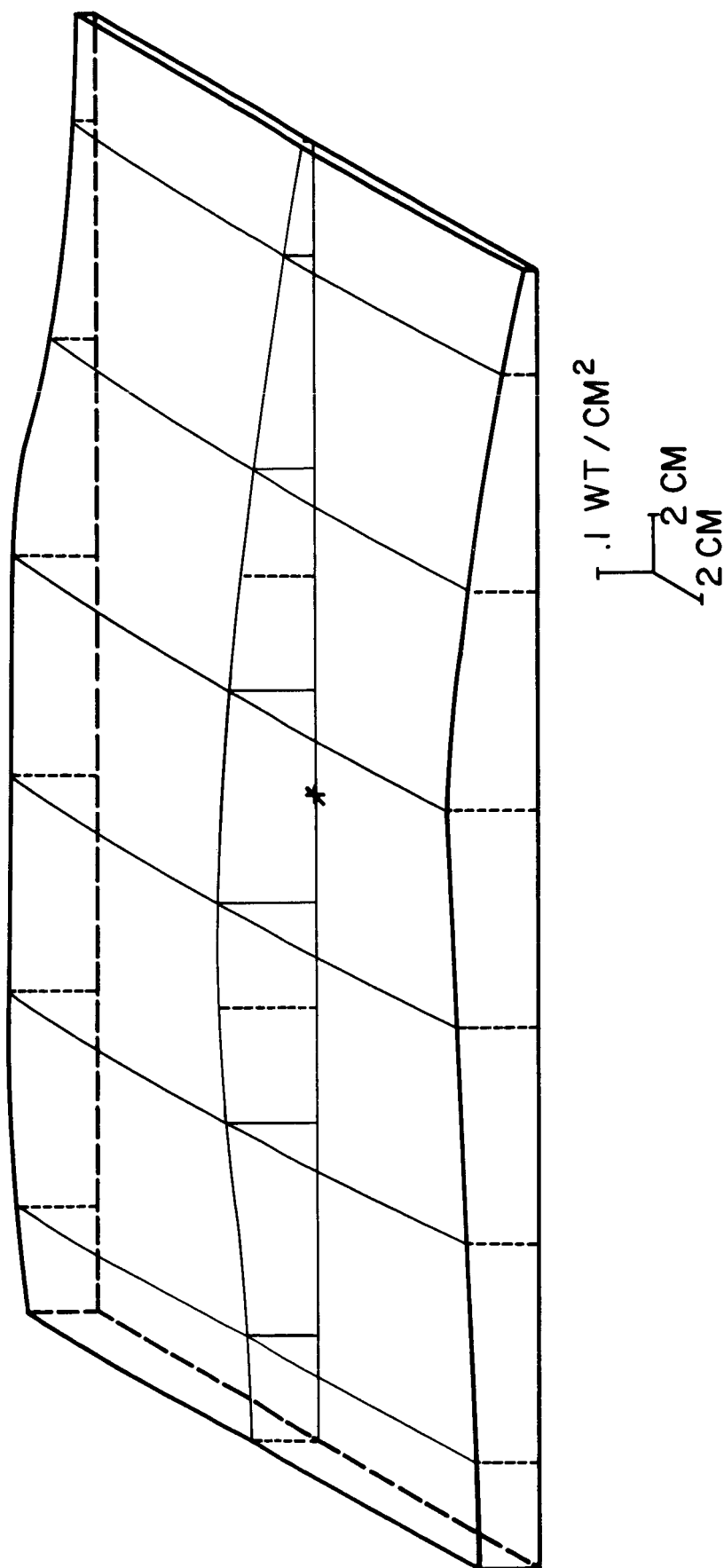2.4 mg/sec.

— EXPERIMENTAL DATA

.1 WT/CM²

2 CM

2 CM

Figure 36. 2" Accelerator (Short Version); Ductless Window; Power Density Contour Map; Figure 4a Magnetic Field Distribution; Incident R-f Power 2100 Watts, Reflection Coefficient 1%, Argon Flow Rate 1.4 mg/sec.

EXPERIMENTAL DATA

.1 WT/CM^2

2 CM

2 CM

Figure 37. 2" Accelerator (Short Version); Ductless Window; Power Density Contour Map; Figure 4a Magnetic Field Distribution; Incident R-f Power 2800 Watts, Reflection Coefficient 1-3%, Argon Flow Rate 2.4 mg/sec.

— EXPERIMENTAL DATA

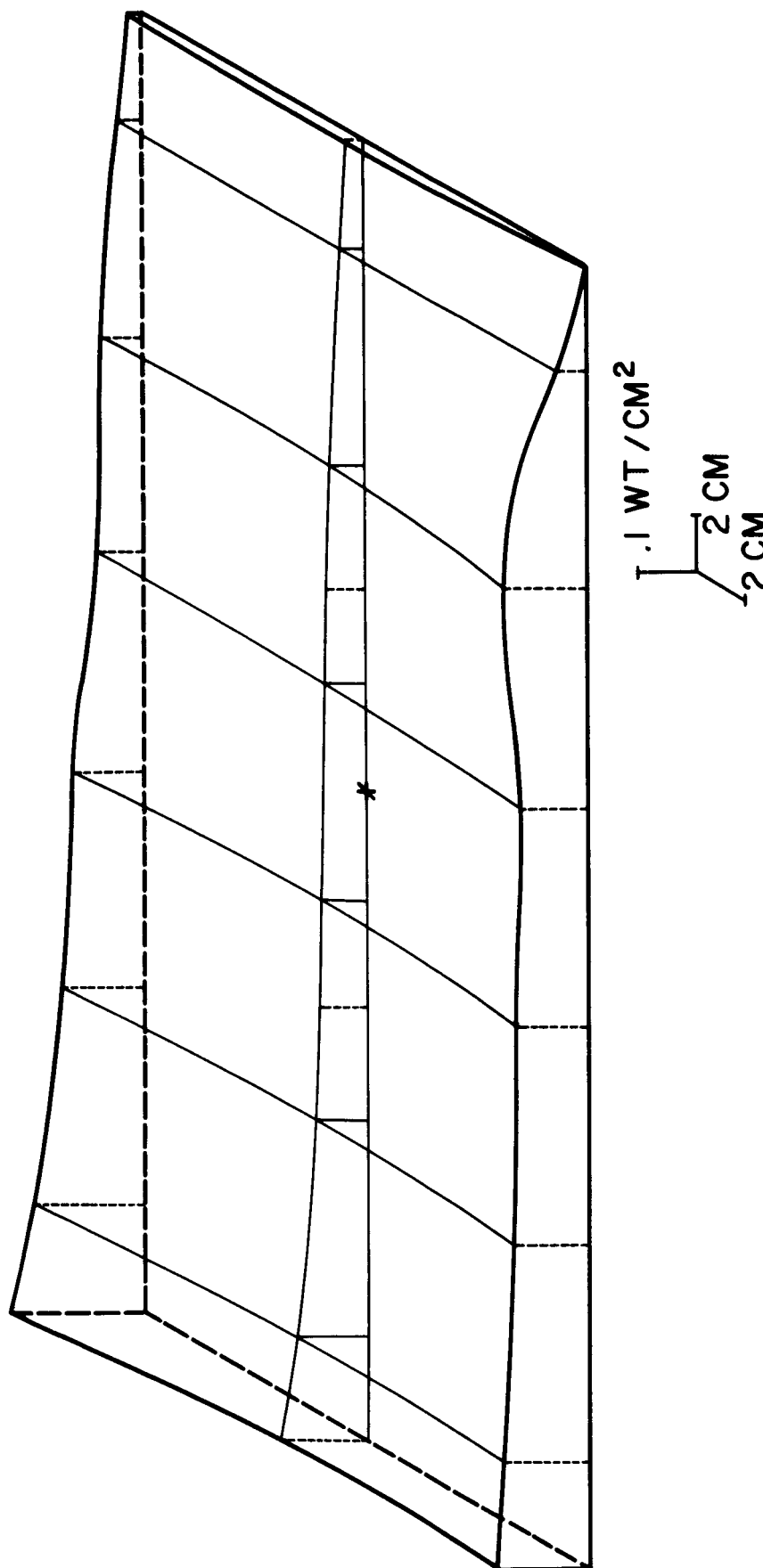$\left[\right. .1 \; WT/CM^2$

2 CM

2 CM

Figure 38. 2" Accelerator (Short Version); Ductless Window; Power Density Contour Map; Figure 4a Magnetic Field Distribution; Incident R-f Power 3600 Watts, Reflection Coefficient 2-3%, Argon Flow Rate 2.4 mg/sec.

EXPERIMENTAL DATA

.1 WT/CM²

2 CM

2 CM
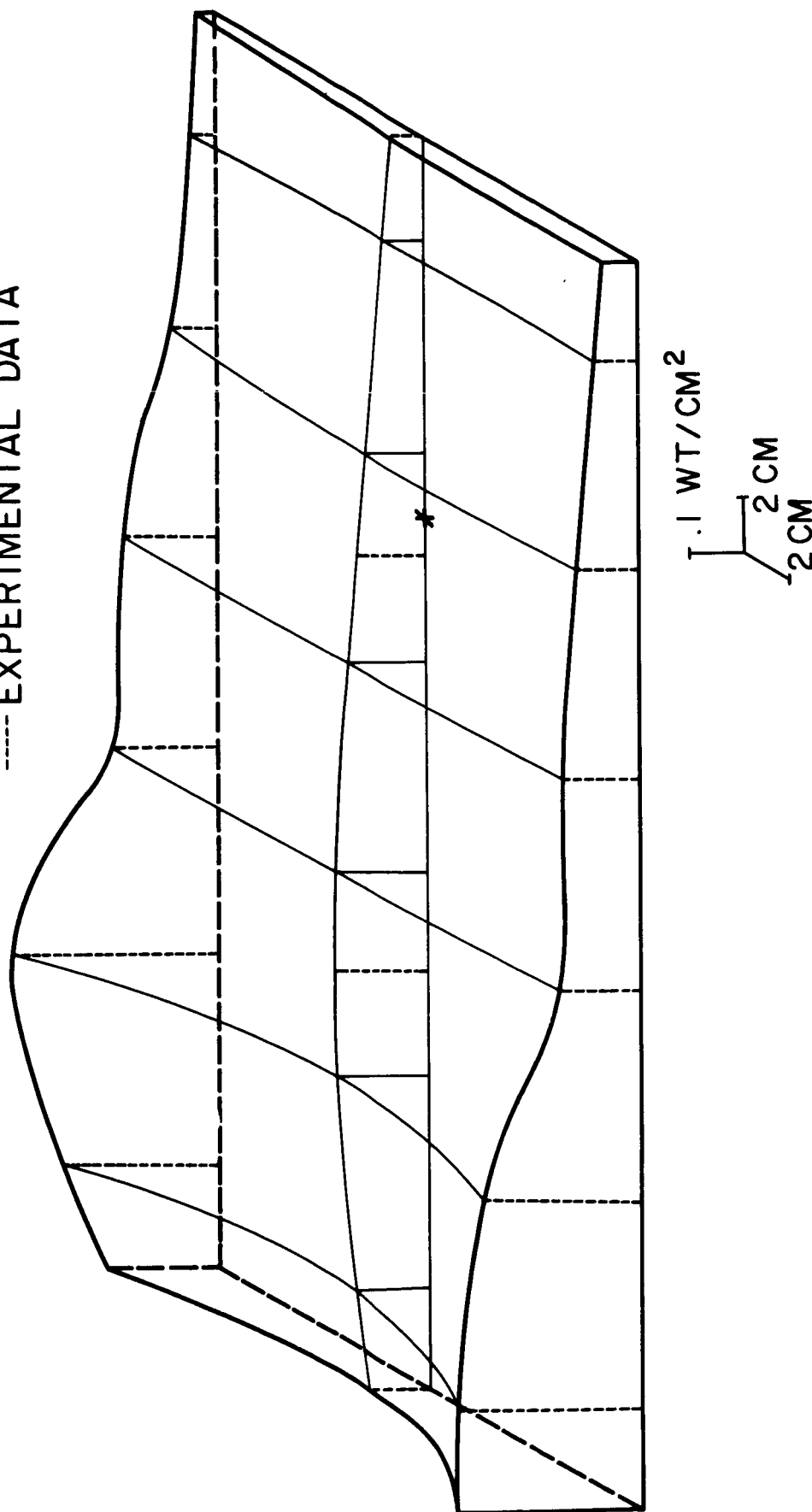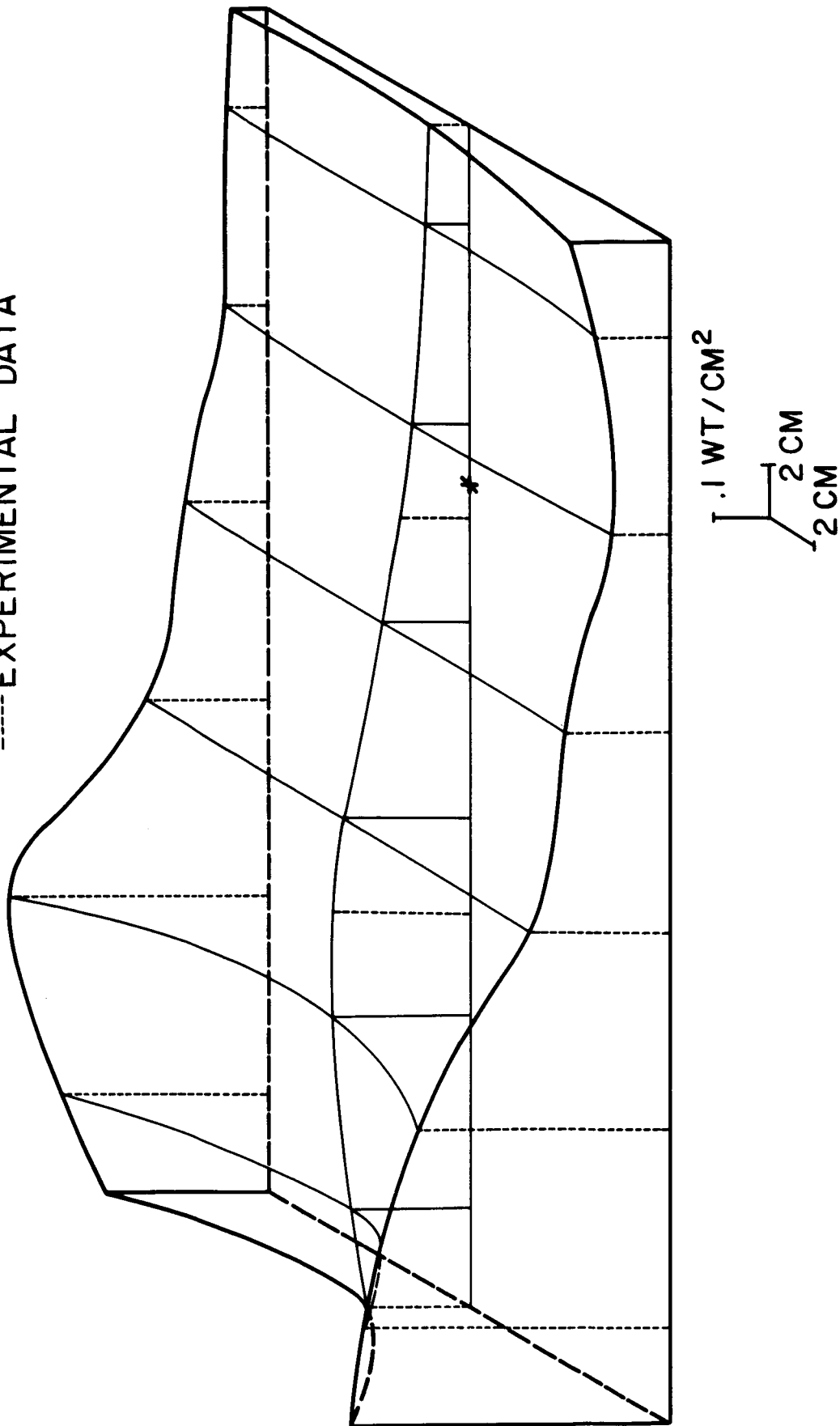
Figure 39.   2" Accelerator (Short Version); Ductless Window; Power Density Contour
Map; Figure 4a Magnetic Field Distribution; Incident R-f Power 4150 Watts,
Reflection Coefficient 1-2%, Argon Flow Rate 2.4 mg/sec.

---- EXPERIMENTAL DATA

2×10^{-4} AMP/CM^2

2 CM
2 CM

Figure 40. 2" Accelerator (Short Version); Ductless Window; Ion Current Density Contour Map; Figure 4a Magnetic Field Distribution; Incident R-f Power 2150 Watts, Reflection Coefficient 2%, Argon Flow Rate 5.0 mg/sec.

— — — EXPERIMENTAL DATA

$2 \times 10^{-4} \ AMP/CM^2$

2CM

2CM

2CM

Figure 41. 2" Accelerator (Short Version); Ductless Window; Ion Current Density Contour Map; Figure 4a Magnetic Field Distribution; Incident R-f Power 2100 Watts, Reflection Coefficient 1%, Argon Flow Rate 2.4 mg/sec.
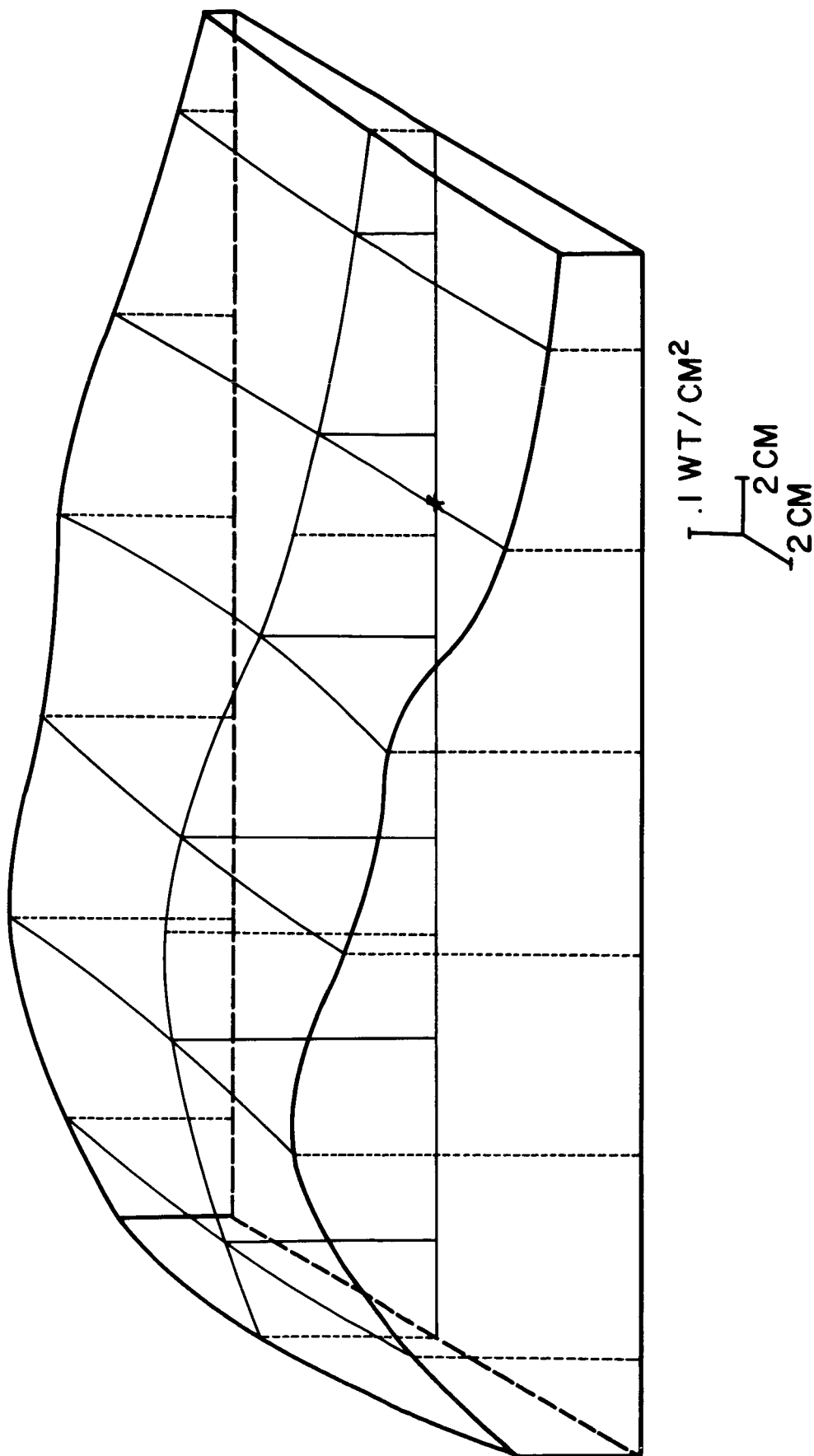
---- EXPERIMENTAL DATA

2×10^{-4} AMP/CM^2

2 CM

2CM

Figure 42. 2" Accelerator (Short Version); Ductless Window; Ion Current Density Contour Map; Figure 4a Magnetic Field Distribution; Incident R-f Power 2100 Watts, Reflection Coefficient 1%, Argon Flow Rate 1.4 mg/sec.

---- EXPERIMENTAL DATA

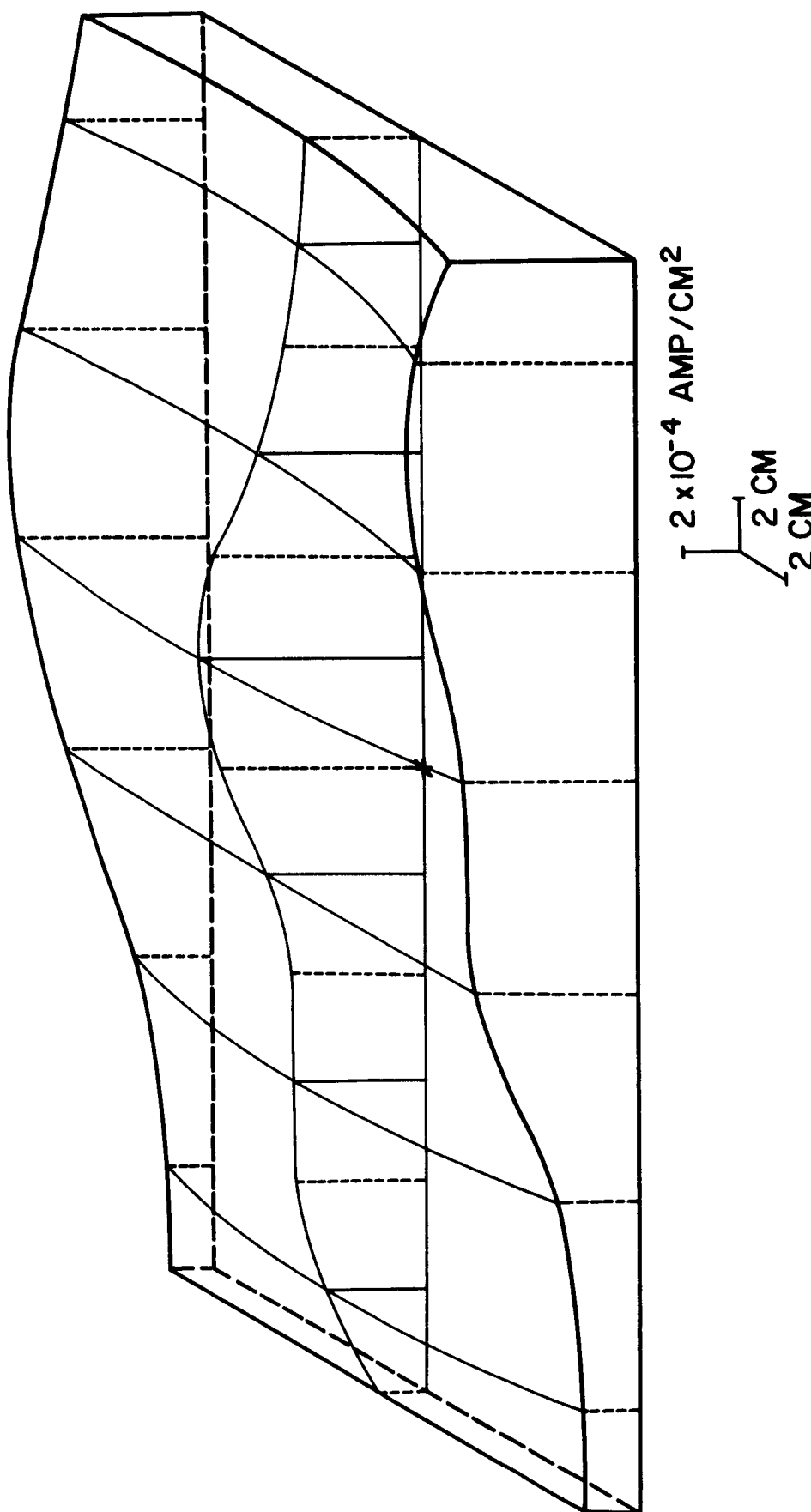2×10^{-4} AMP/CM^2

2 CM

2 CM

Figure 43. 2" Accelerator (Short Version); Ductless Window; Ion Current Density Contour Map; Figure 4a Magnetic Field Distribution; Incident R-f Power 2800 Watts, Reflection Coefficient 1-3%, Argon Flow Rate 2.4 mg/sec.

---- EXPERIMENTAL DATA

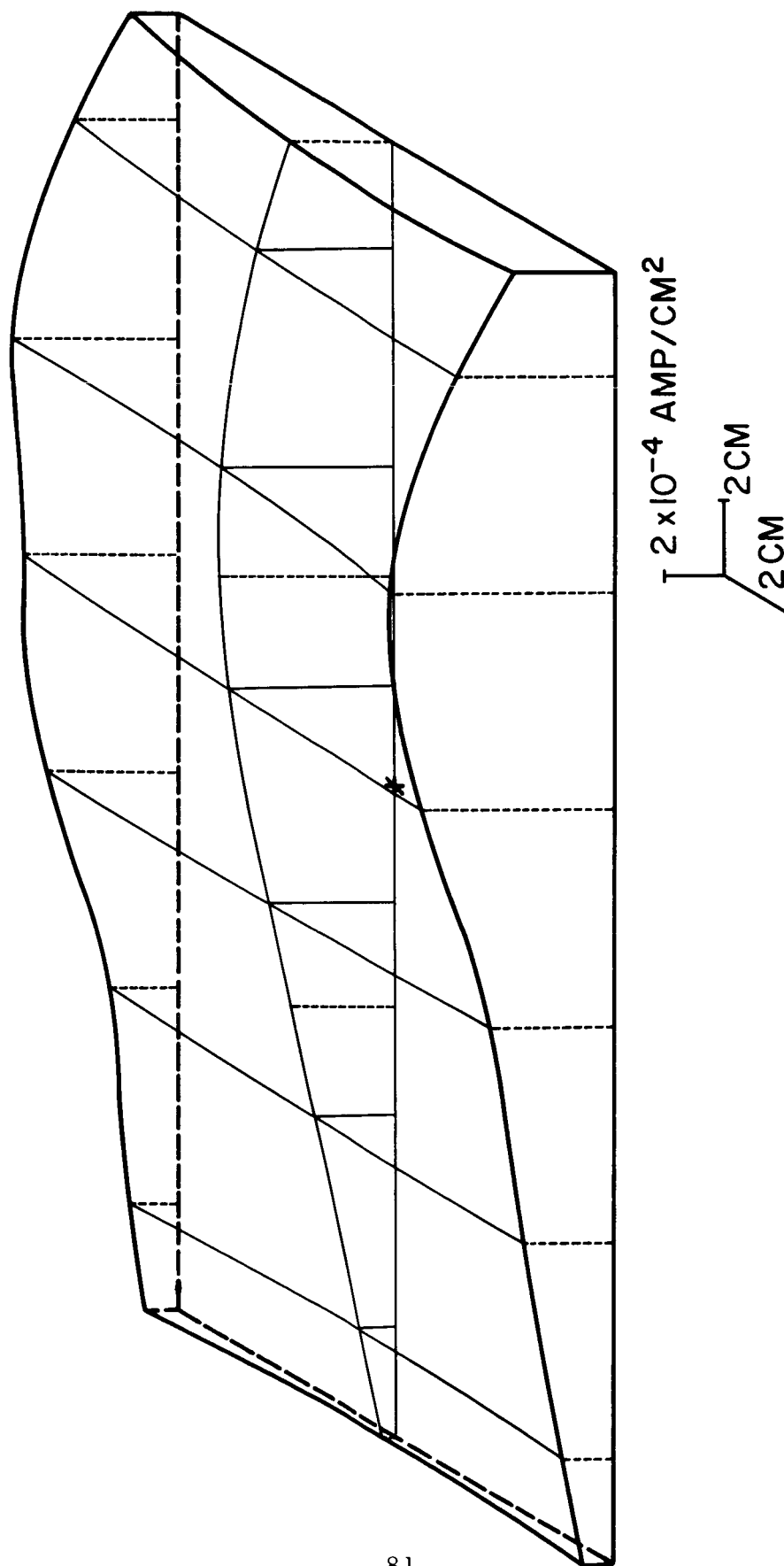2×10^{-4} AMP/CM^2

2 CM

2 CM

Figure 44. 2" Accelerator (Short Version); Ductless Window; Ion Current Density Contour Map; Figure 4a Magnetic Field Distribution; Incident R-f Power 3600 Watts, Reflection Coefficient 2-3%, Argon Flow Rate 2.4 mg/sec.
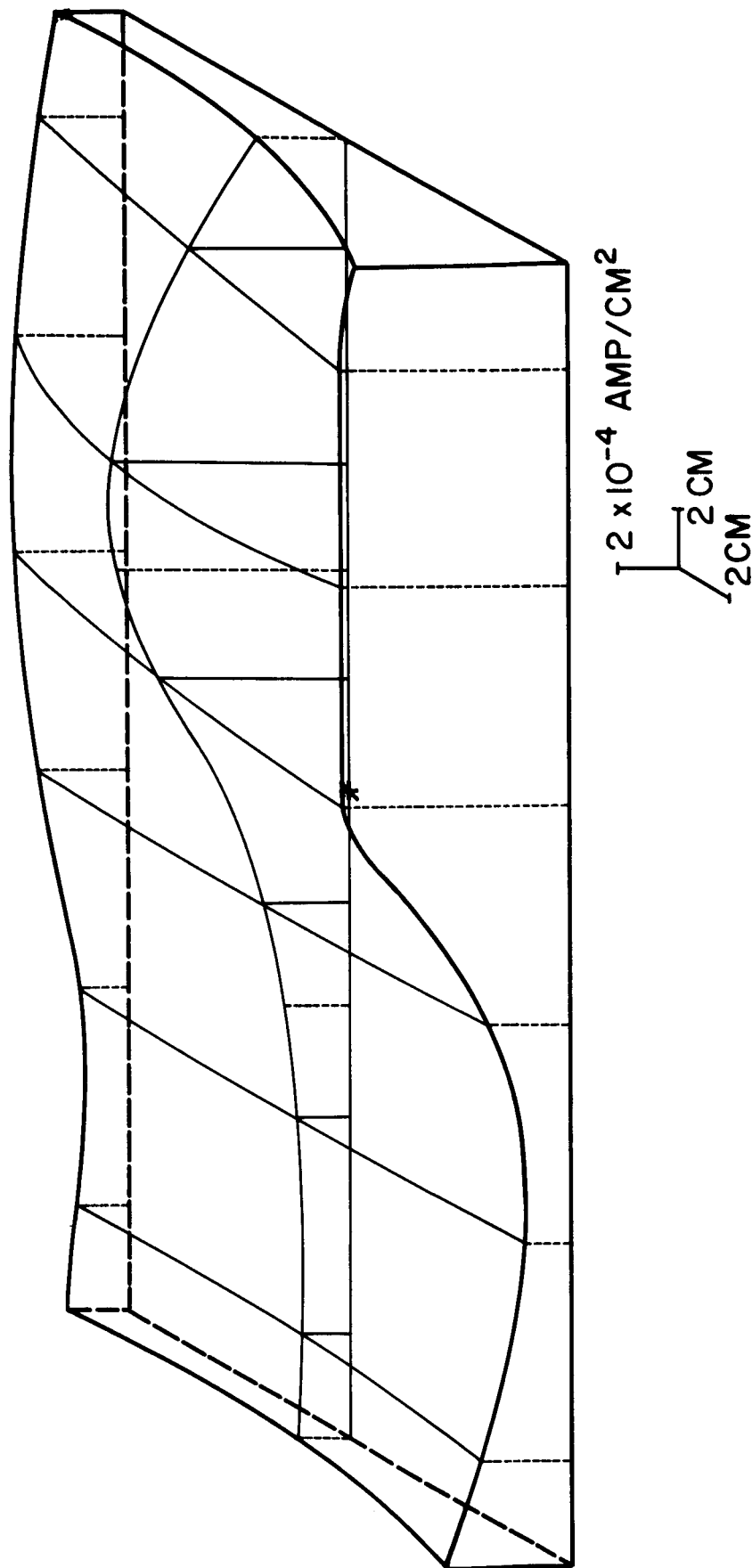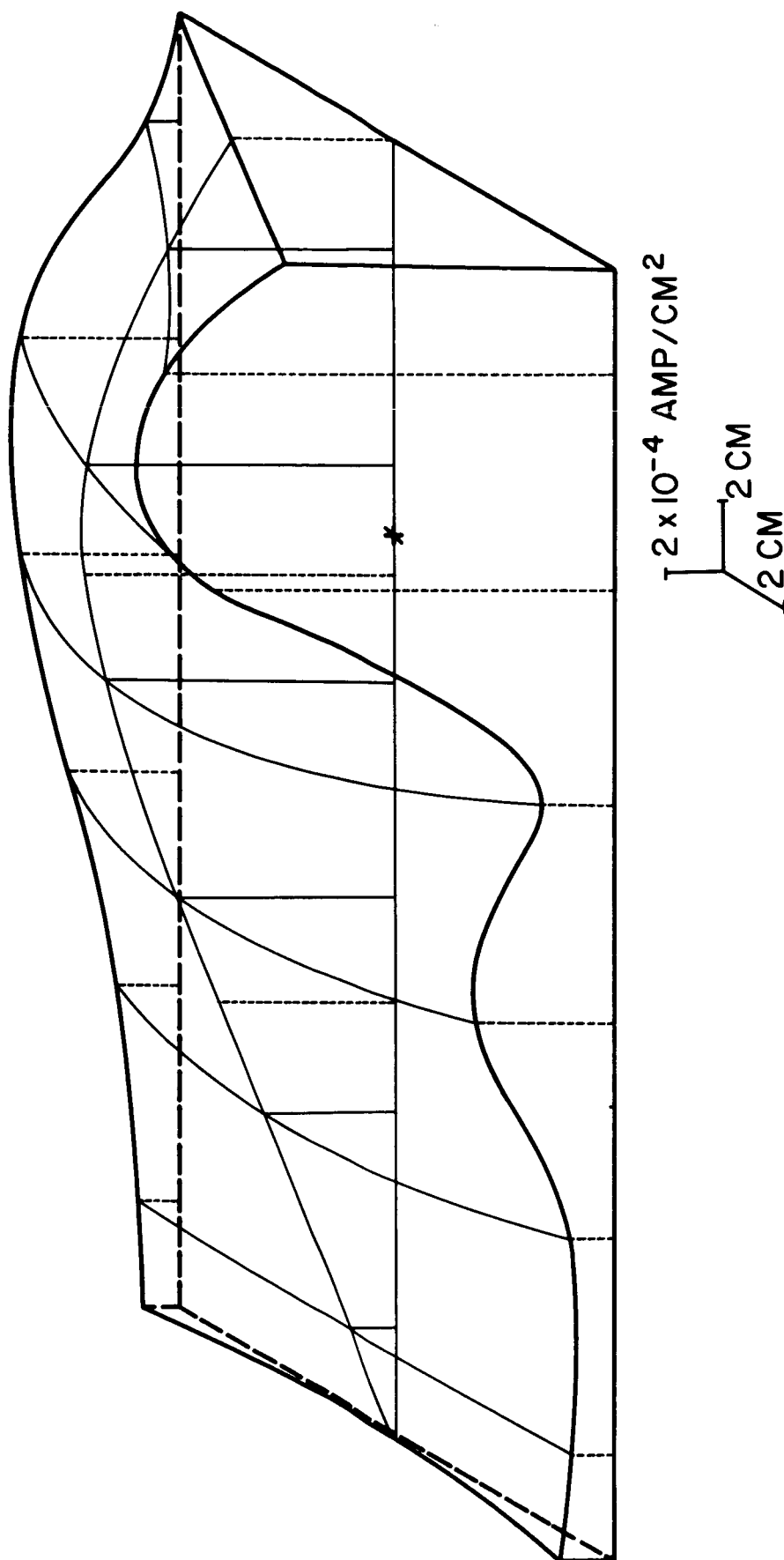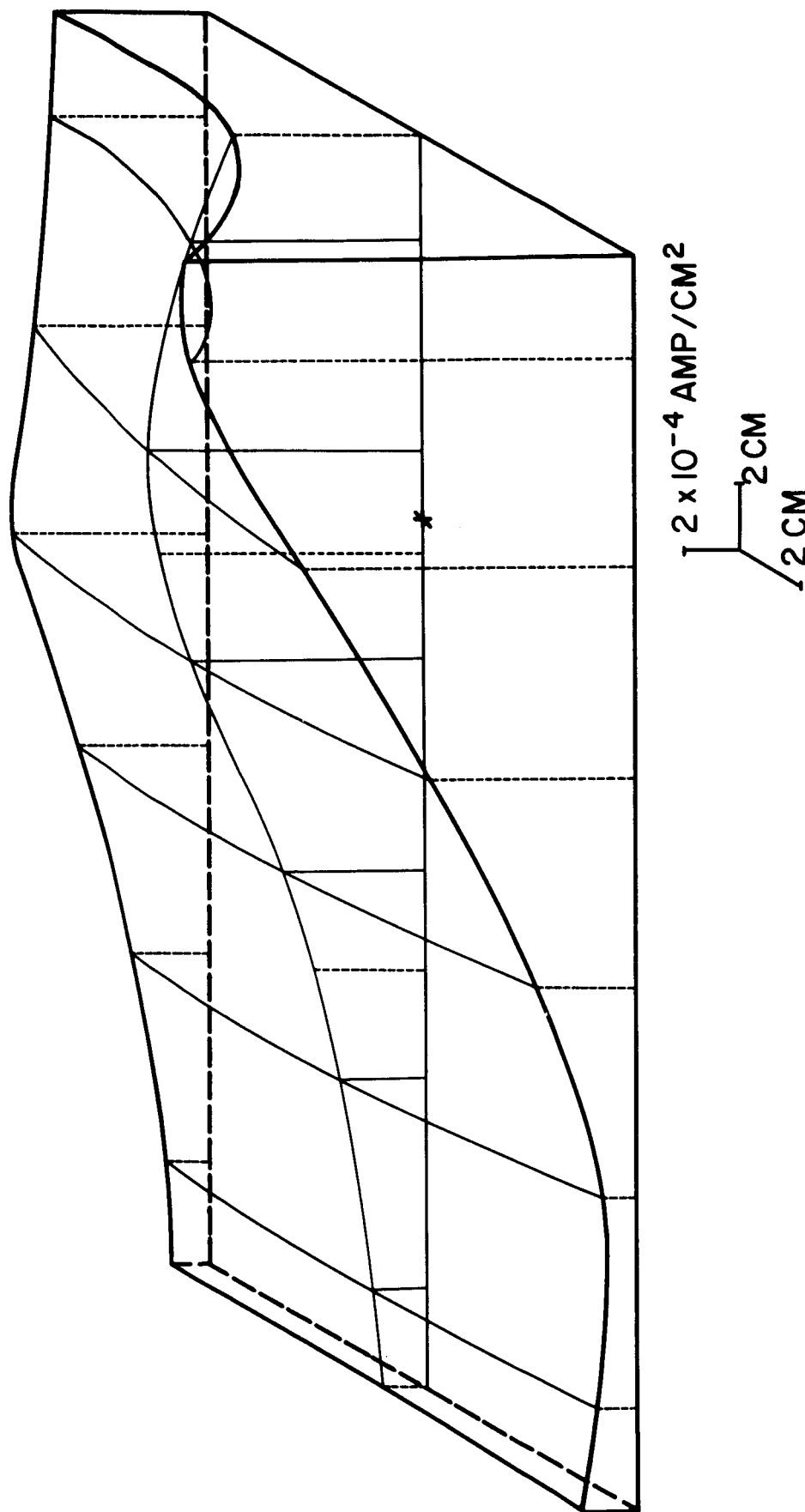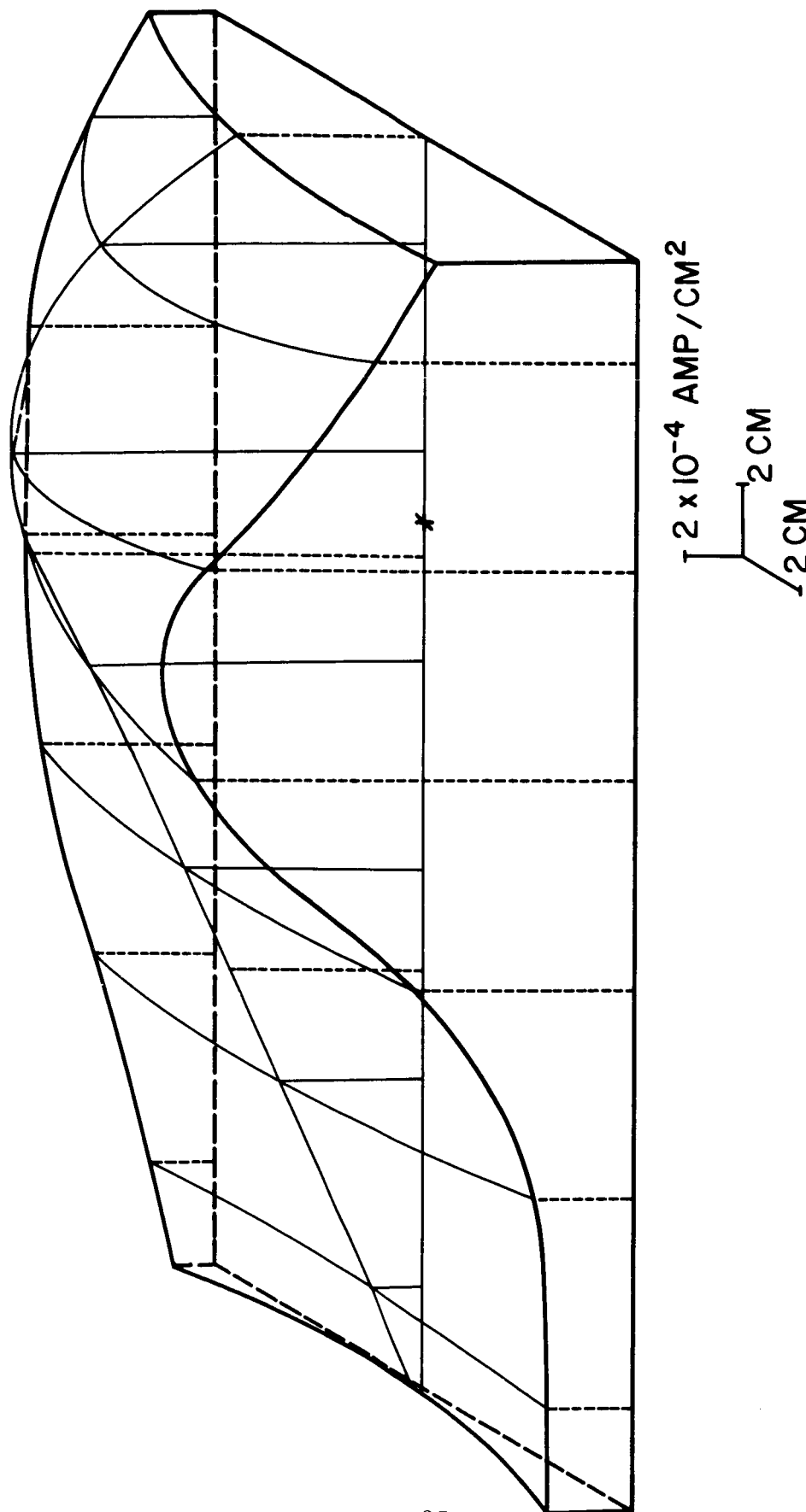
Figure 45. 2" Accelerator (Short Version); Ductless Window; Ion Current Density Contour Map; Figure 4a Magnetic Field Distribution; Incident R-f Power 4150 Watts, Reflection Coefficient 1-2%, Argon Flow Rate 2.4 mg/sec.

are typically down to one-half the peak values in a transverse distance from the peak position of about 15 centimeters. Since the probe array is located 72 centimeters beyond the accelerator window, this yields a half-power half-angle of about 12°.

Both power density and flux density increase as the gas flow rate and r-f power increase. It is interesting to note that the power and flux patterns are not similar for a given flow and r-f power. This indicates a spread in ion velocities which has the effect of diminishing the total efficiency of the thrustor.

The severity of data scatter was investigated under these lower background density conditions. It was found that the basic patterns would repeat from one test to another, for identical values of the controllable variables, with randomness being perhaps $\pm$ 20% of the average. This is a definite improvement over the conditions found with the three-channel probe for the poorer pressure environment. It is our feeling that even this scatter can be substantially improved by better control of the magnetic field.

A photographic view looking into the accelerator during operation is shown as Figure 46. Although the plasma outline is indistinct and is partially blocked by the probe array, it can be seen that the plasma is divided into four areas, each adjacent to one of the gas injection holes. Thus, only a portion of the accelerator cross section is occupied by the more dense plasma, suggesting that, in future designs, the diameter of the accelerator should be decreased or the number of gas injection ports increased.
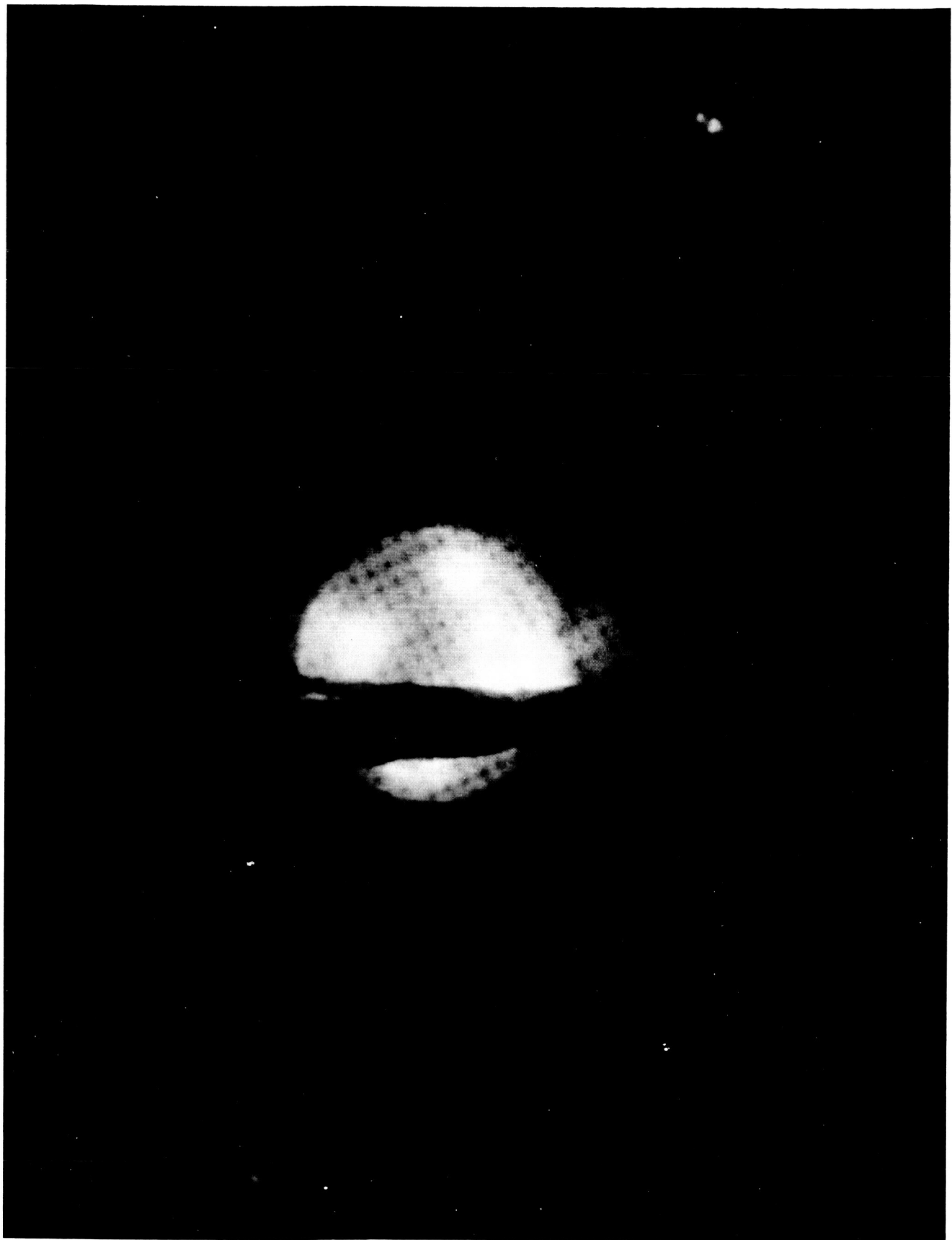
Figure 46. Photographic View Looking into Operating 2" Accelerator (Short Version).

3.   Experimental Program
      Transverse-Interaction Accelerator

During the initial planning of this program, it was felt desirable

to investigate a variety of basic geometries, and, as a result, a design

basically different from the longitudinal-interaction accelerator was built

and tested during this contract period. This accelerator, called the trans-

verse-interaction design, is shown in Figures 47 and 48.

In this accelerator, a continuous flow of un-ionized gas is introduced

into one end of the preionizer section, shown at the left end of the assembly

view in Figure 48. D-c field coils are mounted coaxial with parts 6 and 3

.(assembly view, Figure 48), generating a solenoidal magnetic field coaxial

with the assembly.

The gas stream, partially ionized as it passes through the preionizer,

flows through the orifice in part 11 and eventually out the exit end of the

accelerator. As the gas passes through the cylindrical cavity, however,

it is further ionized and its electrons are accelerated in cyclotron orbits

by the cavity r-f field, which in turn is sustained by r-f power entering

through the waveguide flange (21).

In a manner exactly analogous to the longitudinal-interaction device,

the plasma is accelerated by the field-gradient/charge separation process

as the energized plasma flows out through the diverging portion of the magnetic

field.

As implied by its name, it is seen that in this accelerator, the power

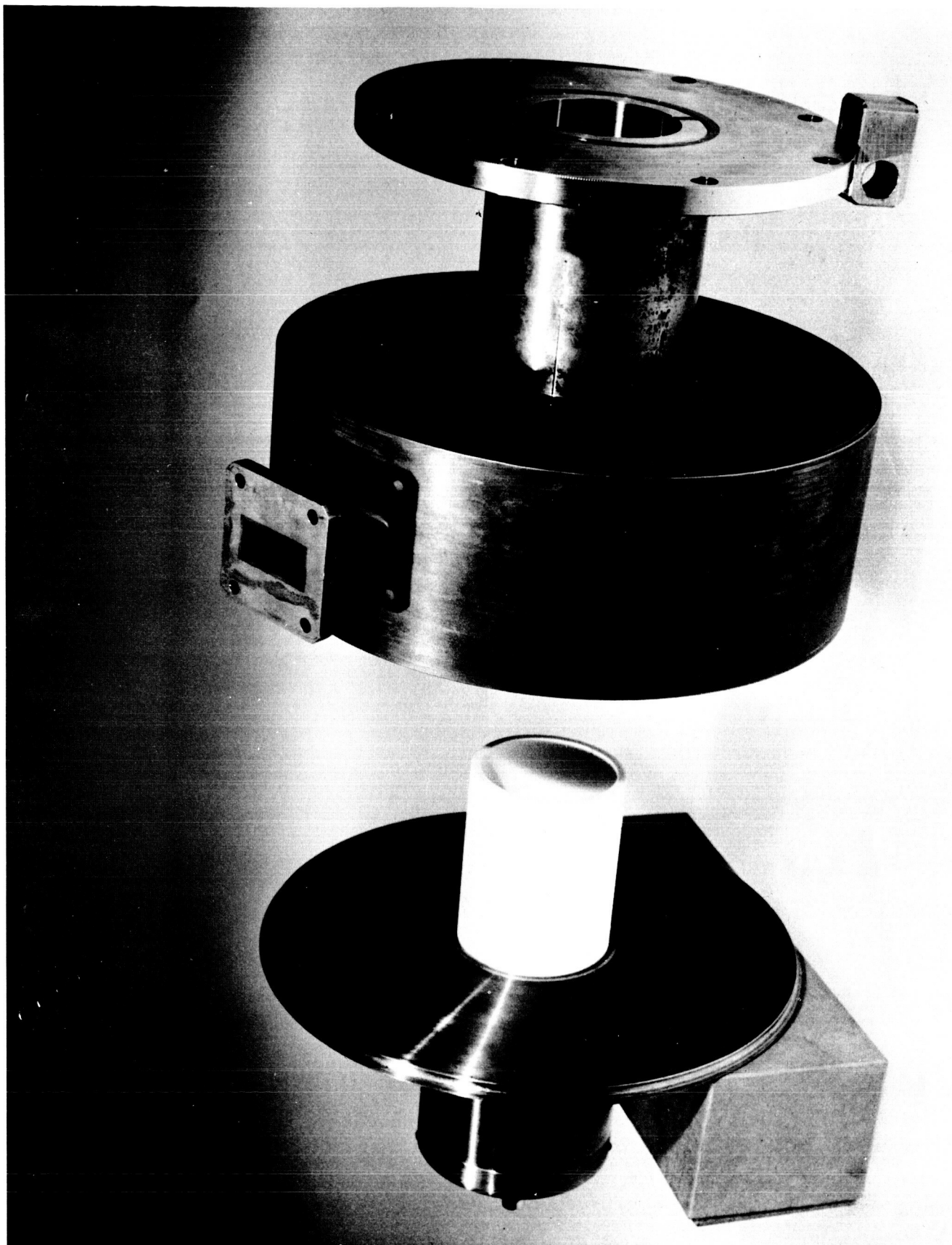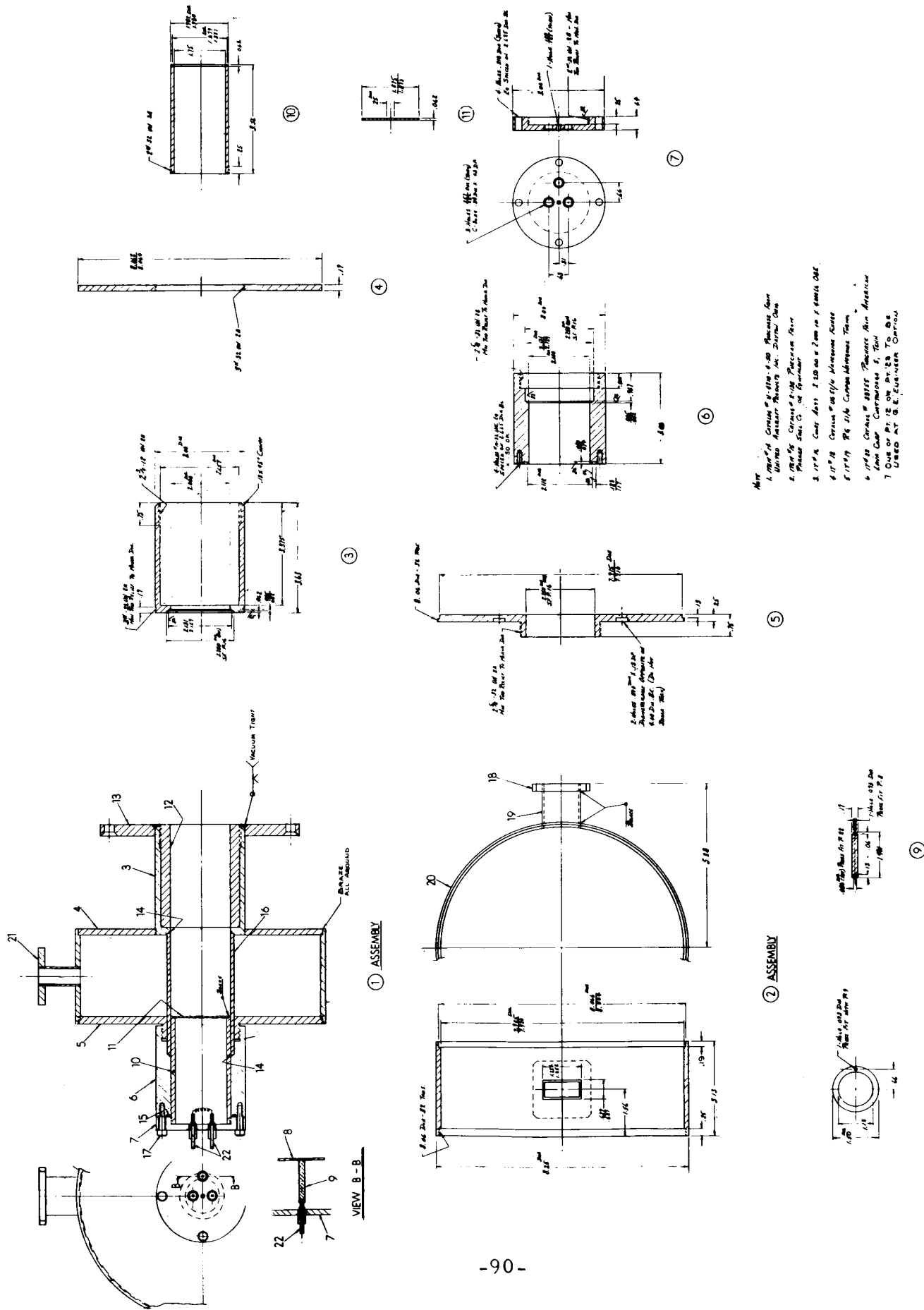flow direction which is radially through the ceramic tube (16), is transverse

Figure 47.   Transverse - Interaction Accelerator; Photographic View Before Final Assembly, Showing Plasma Source (Far Left), Ceramic Plasma Chamber, Cylindrical Cavity Resonator (with Waveguide Coupling) and Exit Orifice (Far Right).

Figure 48. Transverse - Interaction Accelerator; Engineering Drawing.

-90-

to the field direction. This has at least two possible advantages:

1). The area through which the power passes into the plasma is not limited by waveguide dimensions and therefore can be made quite large, thereby reducing power density.

2). The end of the device opposite to the exit orifice is not encumbered by the r-f input, leaving much more freedom in design of the gas injector, as exemplified by the plasma source used here.

Before significant tests could be made, the design had to be altered somewhat from the Figure 48 design in order to achieve an adequate seal around the ends of the ceramic tube (16). A silicone rubber o-ring was used in place of the metal o-ring (14) at the source end of the tube. A copper flange was brazed onto the ceramic tube at the other end and a seal was obtained by compressing another rubber o-ring between this new flange and the face of part 3.

During operation, the preionizer was run at 30 watts (150 volts, 200 ma) with an additional few watts going to heating the thermionic tungsten filament. R-f power levels up to 2100 watts were employed, and behavior for various argon flows and field configurations were studied. The field shape for this device, by the way, generally has a minimum in the cavity region because of the wide spacing between coils. The steady-state calorimeter (Section 2.2.6) was used to measure plasma stream power during these tests.

A conical, pale-blue plasma stream could be observed to be emerging

from the accelerator. In no case, however, did the calorimeter recover more

than a percent or so of the r-f input power. R-f reflection coefficient was

generally below 0.10.

The poor efficiency of this model, coupled with the success achieved

with the longitudinal-interaction accelerator and with the fact that the ceramic

tube (part 16, Figure 48) cracked after a short testing period, caused these

tests to be terminated before any thorough parametric survey of this

accelerator's characteristics were obtained.

4. SUMMARY AND CONCLUSIONS

4.1 Review

A review of this year's accomplishments indicates significant advances in both engine performance and testing techniques. With regard to thrustor performance, note the following items:

1). Efficiency with which power is coupled from the r-f field into the plasma has been shown to be very good, that is, typically over 95%.

2). The efficiency with which the r-f power is converted to directed motion of the accelerated plasma stream has also been found to be quite good, as high as 54% under proper conditions.

3). Power levels and test durations have been markedly improved during this year. X-band accelerator designs on hand at the beginning of this period (developed during the last few months of Contract NAS5-1046) would not last for more than a few seconds at a kilowatt r-f power. During this year, designs have been achieved which have run without damage for minutes at a time at several kilowatts r-f power. In addition it was found that the thrustor wall temperature had stabilized by the end of these runs.

Several testing techniques were developed and applied during this year. Sampling and total calorimetry were used to good advantage both in the thrustor itself and in the accelerated plasma stream. The concept of sampling the plasma stream power density and ion flux density at many

points in a stream cross section was tested and resulted in a valid technique

for exploring the stream profile. By contrast, a relatively "old" technique,

the sampling pendulum, was rejected because of possible electrostatic

force interference.

4.2   Potential

Although a great deal of effort must still be expended to develop

this accelerator as a space propulsion engine, this year's results do

indicate potentially favorable characteristics as a thrustor. With this

favorable performance having been demonstrated, it is proper to inquire

in more detail into possible thrustor applications. With the realization

of good coupling and conversion efficiencies, and the appearance on the

microwave tube market of high-power, high-efficiency, r-f sources, it is

probable that the cyclotron-resonance plasma thrustor can be competitive

with other plasma engines now under development. In addition, the r-f

character of this engine makes it uniquely suited to vehicles which already

have r-f on board for communications and radar purposes. Thus, a

cyclotron-resonance engine could readily be used for station keeping on a

24 hour communications satellite. A similar thrustor could be used for

trajectory correction and even prime propulsion on a deep space probe,

which would of necessity carry large amounts of radio frequency power

for communications.

4.3 Future Program

The major goal of a continuing program should be improvement in engine performance. Improvements should first of all be made in power, mass and velocity efficiencies, leading as a result to improved overall efficiency. Secondly, improvement should be made in engine repeatibility and durability. Finally, the use of permanent magnets should continue to be considered.

Along with and necessary to the performance improvement program, development of old and new diagnostics techniques should continue. For instance, a thrust stand should be developed for direct measurement of engine thrust. In addition, more accurate probes of plasma potential and electron energy must be developed in order to study the important plasma processes upon which engine performance depends. Techniques for measurement of the ion velocity distribution must also be improved.

Finally, a continuing program should include study of this type of thrustor as part of a mission system. Missions for which this thrustor is uniquely qualified should be identified, and weight, size and power requirements of the thrustor should be specified and compared with competitive engines.

APPENDIX

Charge Exchange; Effect on Accelerator Characteristics

If the accelerated plasma stream passes through a background gas between emergence from the accelerator and impingement on some measuring instrument (such as a calorimeter or particle analyser), interactions between the accelerated plasma and the background gas will cause the stream characteristics as measured to differ from stream characteristics at emergence from the accelerator. The dominant process under these conditions is very likely to be the transfer of charge from the stream ions to the background gas molecules.

We will assume that the ion path length in the acceleration region is short compared with the path length ℓ_m from the end of the acceleration zone to the plane in which measurements are made. In this case, stream energy remains constant, and the calorimeter will measure the true stream power. Similarly, the velocity distribution of the arriving stream will be the same as for the stream emerging from the accelerator. If the total efficiency,

$$\eta = \frac{T^2}{2\,PR}$$

is expressed as the product of mass, power and velocity efficiencies,

$$\eta = \eta_m\, \eta_p\, \eta_v = \left(\frac{R_1}{R_0}\right)\left(\frac{P_1}{P_0}\right)\left(\frac{(\bar{v})^2}{\overline{v^2}}\right)$$

(where R_0 and R_1 are the input and accelerated mass flows, respectively)

then these results mean that valid measurements of η_p and η_v will be made.

The mass efficiency η_m will, however, not be accurate if the ion flux, as measured in a probe circuit, is taken to be the total flux. That is, R_1 will contain accelerated ions (R_i) which reached the probe undisturbed, and neutrals (R_n) which originally were accelerated ions but which lost their charge during transit to the probe. A comparison must now be made between the measured mass efficiency η_{mm} (using ion flux data), and the true mass efficiency η_m:

$$\eta_{mm} = \frac{R_i}{R_o}$$

$$\eta_m = \frac{R_1}{R_o} = \frac{R_n + R_i}{R_o} = \eta_{mm} + \frac{R_n}{R_o}$$

The neutral flux in the stream can be expressed as:

$$R_n = R_1 \left(1 - e^{-n\sigma \ell_m} \right)$$

where n is the background particle density and σ is the charge exchange cross section. If the product $n \sigma \ell_m$ is small, this can be approximated by:

$$R_n \simeq n\sigma \ell_m R_1$$

and

$$\eta_m \simeq \eta_{mm} + n\sigma \ell_m$$

For argon ions with energies of approximately 200 volts, σ will be about 3×10^{-15} cm^2.[*] Let us assume the transit path ℓ_m is 100 cm and

----

[*]-Sanborn C. Brown, Basic Data of Plasma Physics, J. Wiley, New York, 1959, p. 37.

calculate the background pressure needed to cause a 10% change in the result.

$$n = \frac{\eta_m - \eta_{mm}}{\sigma \ell_m}$$

$$= \frac{\eta_m}{3} \times 10^{12}$$

For purposes of calculation, assume η_m is 0.3, requiring that n be

1×10^{11} particles/cm^3 or less in order that charge exchange not cause more

than a 10% change in the mass efficiency measurement. This means that the

background pressure (at room temperature) should be something under

1×10^{-5} mm Hg.